



**NTNU – Trondheim**  
Norwegian University of  
Science and Technology

# Hydrogen Induced Stress Cracking of Inconel 718 under Cathodic Polarization

Effects of Hydrogen on the Initiation and  
Propagation of Cracks

**Kristian Knarbakk**

Materials Science and Engineering

Submission date: June 2015

Supervisor: Roy Johnsen, IPM

Co-supervisor: Afrooz Barnoush, IPM  
Gaute Stenerud, IPM

Norwegian University of Science and Technology  
Department of Engineering Design and Materials



---

# Abstract

This work has examined the susceptibility to hydrogen induced stress cracking (HISC) of Inconel 718 (UNS N07718) by stepwise tensile loading tests with in situ cathodic polarization. Specifically, the effect of hydrogen on crack initiation and propagation in Inconel 718 has been investigated by use of scanning electron microscope (SEM) and electron backscatter diffraction (EBSD). Materials with two different grain sizes were examined in order to explore the effect of grain size on HE in Inconel 718. An attempt was made to develop a novel procedure for measuring local strains in tensile samples tested with in situ cathodic polarization. This procedure was based on using digital image correlation software to analyze series of images obtained with an optical microscope during tensile testing.

Inconel 718 material of both grain sizes were found to be susceptible to HISC, based on fracture surfaces exhibiting transgranular cleavage fractures and severe secondary cracking on the sample surface. No secondary cracking was observed for samples tested in air. Qualitative examinations of specimen surfaces in SEM suggested that crack initiation happens preferentially at grain boundaries (GBs) and twins. This was supported by EBSD results indicating higher dislocation density at GBs and twins. Crack propagation happened transgranularly, as evidenced by the fracture surfaces. Hydrogen induced localized plasticity (HELP) is assumed to be the dominating mechanism for HISC, as suggested by significantly deformed regions near the crack edge and surrounding the crack tip. Particle content did not appear to affect crack initiation. A method for using digital image correlation technology to map local strains from in situ tensile testing was developed, although more work is necessary to refine the method and setup.





# Sammendrag

I denne masteroppgaven har mottakelighet for hydrogenindusert sprekking (HISC) i Inconel 718 (UNS N07718) blitt undersøkt ved hjelp av stegvis strekktesting med in situ katodisk polarisering. Særlig har effekten av hydrogen på sprekkitiering og propagering i Inconel 718 blitt undersøkt ved hjelp av scanning elektronmikroskop (SEM) og elektronmikrodiffraksjon (EBSD). Materialer med to forskjellige kornstørrelser ble undersøkt for å studere effekten av kornstørrelse på hydrogensprøhet. Det ble gjort forsøk på å utvikle en ny prosedyre for måling av lokale tøyninger i strekkprøvene testet med in situ polarisering. Denne prosedyren er basert på bruk av ”digital image correlation”-programvare for å analysere bildeserier som ble tatt med optisk mikroskop under strekkprøving.

Inconel 718 med begge kornstørrelser viste seg å være mottagelig for HISC, basert på bruddflater som viste transgranulære kløyvningsbrudd og utbredt sekundærsprekking på prøveoverflaten. Ingen sekundærsprekking ble observert for prøvene som ble testet i luft. Kvalitative undersøkelser av prøveflater i SEM antydte at sprekkitiering skjer fortrinnsvis ved korn grensene og tvillinger. Dette ble støttet av EBSD-resultater som indikerte høyere dislokasjonstetthet på korn grenser og tvillinger. Bruddflatene viste at sprekkpropagering skjedde transgranulært. Hydrogenindusert lokalisert plastisitet (HELP) antas å være den dominerende mekanismen for HISC, basert på betydelig deformerte regioner nær sprekkanten og rundt sprekkspissen. Partikkelinnhold så ikke ut til å påvirke sprekkitiering. En metode for å bruke ”digital image correlation”-teknologi til å kartlegge lokale tøyninger fra in situ strekktesting ble utviklet, men mer arbeid er nødvendig for å utvikle metoden og oppsettet videre.



# Preface

This master's thesis is submitted to NTNU as a part of the Master's program at the Department of Materials Science and Engineering. It is submitted as the final product of the master's thesis project TMM4911. Professor Roy Johnsen has supervised this work, with Professor Afrooz Barnoush and Ph.D. candidate Gaute Stenerud as co-supervisors. Jim Stian Olsen has been the industrial contact representing Aker Solutions.

I would like to extend my gratitude toward my supervisors for sharing their knowlegde and providing guidance throughout this project. Meetings and discussions during the semester have improved the quality of this work. I would especially like to thank Ph.D. candidate Gaute Stenerud for helping me in the laboratory and for providing insightful knowledge. Thanks are due to Kjetil Fosslund Veium for close cooperation in the lab and to Ph.D. candidates Haiyang Yu and Petter Henrik Holmstrøm for help with ABAQUS and eCorr. I am grateful to Aker Solutions for providing financial funding and to ATI Metals for providing the materials tested in this work.

In addition, thanks are due to Yingda Yu for sharing his knowledge of the scanning electron microscope, to Trygve Lindahl Schanche and Nils-Inge J. Nilsen for help in the laboratory, and to Christian Oen Paulsen for teaching me how to use EBSD. I am grateful to Jarand Nærland for proof reading my thesis.

Finally, a special thanks to Tonje Marie Bø Vaksvik for supporting me, proof reading and contributing with great advice.

Trondheim, June 7, 2015



---

Kristian Knarbakk



# List of Figures

2.1	Examples of $\delta$ -particles precipitated in Inconel 718 . . . . .	4
2.2	Formation of a cup-and-cone ductile fracture . . . . .	5
2.3	Stresses acting on an elemental cube . . . . .	6
2.4	Stress directions . . . . .	7
2.5	Principal stress . . . . .	7
2.6	Schematic representation of notch stress . . . . .	8
2.7	Ingredients of HISC . . . . .	9
2.8	Dislocation pile-ups . . . . .	12
2.9	Pourbaix diagram . . . . .	14
2.10	Ductile fracture . . . . .	19
2.11	Typical example of a brittle cleavage fracture . . . . .	20
2.12	Typical example of a brittle intergranular fracture . . . . .	20
2.13	eCorr DIC mesh . . . . .	21
2.14	eCorr DIC principal strain map . . . . .	21
2.15	DIC contrast example . . . . .	22
2.16	EBSD schematic . . . . .	23
2.17	EBSD grain map . . . . .	24
2.18	Orientation color legend . . . . .	24
3.1	P3A01 - 1900: Coarse grained material . . . . .	26
3.2	P3A01 - 1850A: Fine grained material . . . . .	26
3.3	Specimen dimensions . . . . .	26
3.4	Polished specimen . . . . .	27
3.5	Tensile test setup for reference test . . . . .	28
3.6	Microscope setup . . . . .	29
3.7	Microscope setup version 2 . . . . .	30
3.8	Microscope setup version 2 top view . . . . .	30
3.9	Old electrolyte chamber . . . . .	31
3.10	Electrolyte chamber . . . . .	32
3.11	New electrolyte chamber top view . . . . .	32
3.12	Tensile test example . . . . .	34
4.1	1900 microstructure . . . . .	38
4.2	1850B microstructure . . . . .	39
4.3	1900 particles SEM . . . . .	40
4.4	1850B particles SEM . . . . .	40
4.5	1850A SN-6 EDS . . . . .	41
4.6	1900 SN-8 EDS . . . . .	43
4.7	P3A01 - 1900: Coarse grained material . . . . .	45
4.8	P3A01 - 1850B: Fine grained material . . . . .	45

4.9	1900 tensile test fracture results . . . . .	47
4.10	1850A tensile test fracture results . . . . .	48
4.11	1900 SN-5 potential-time curve . . . . .	49
4.12	Potential-curves . . . . .	50
4.13	1850A SN-4 fracture surface map . . . . .	52
4.14	1850A SN-1 ductile features . . . . .	53
4.15	1850A SN-4 brittle features . . . . .	54
4.16	1850A SN-4 ductile features . . . . .	54
4.17	1900 SN-1 ductile features . . . . .	55
4.18	1900 SN-5 brittle features . . . . .	56
4.19	1900 SN-5 ductile features . . . . .	56
4.20	Measurement of area . . . . .	58
4.21	Main crack vs. secondary crack . . . . .	59
4.22	Main crack . . . . .	60
4.23	Map of imaged areas . . . . .	61
4.24	1900 SN-1 main crack . . . . .	62
4.25	1900 SN-1 no secondary cracking . . . . .	62
4.26	1900 SN-4 main crack . . . . .	63
4.27	1900 SN-4 cracked particle . . . . .	64
4.28	1900 SN-2 main crack . . . . .	65
4.29	1900 SN-2 secondary cracking . . . . .	66
4.30	1900 SN-2 crack at twin . . . . .	66
4.31	1900 SN-3 cracking at notch . . . . .	67
4.32	1900 SN-3 crack along grain boundary . . . . .	68
4.33	1900 SN-3 cracking at notch . . . . .	69
4.34	1900 SN-3 cracking at twin . . . . .	69
4.35	1900 SN-6 crack along grain boundary . . . . .	70
4.36	1900 SN-7 cracking at notch . . . . .	71
4.37	1900 SN-7 cracked particle . . . . .	71
4.38	1900 SN-8 cracking at notch . . . . .	72
4.39	1900 SN-8 inside notch area . . . . .	73
4.40	1850A SN-6 no secondary cracking . . . . .	74
4.41	1850A SN-6 cracked particle . . . . .	75
4.42	1850A SN-2 secondary cracking overview . . . . .	76
4.43	1850A SN-2 cracked particle . . . . .	76
4.44	1850A SN-2 crack at twin boundary . . . . .	77
4.45	1850A SN-5 main crack . . . . .	78
4.46	1850A SN-5 secondary cracking . . . . .	78
4.47	1850A SN-7 no secondary cracking . . . . .	79
4.48	1900 SN-6 EBSD 681X . . . . .	81
4.49	1900 SN-6 EBSD grain map . . . . .	81

4.50	1900 SN-6 EBSD KAM 681X . . . . .	81
4.51	1900 SN-6 EBSD 501X . . . . .	82
4.52	1900 SN-6 EBSD grain map . . . . .	82
4.53	1900 SN-6 EBSD KAM 640X . . . . .	82
4.54	1850A SN-5 EBSD 2280X . . . . .	83
4.55	1900 SN-6 EBSD grain map . . . . .	83
4.56	1850A SN-5 EBSD KAM 2280X . . . . .	83
4.57	1900 SN-6 in situ optical image zero load . . . . .	84
4.58	1900 SN-6 in situ optical image (71 % of YS) . . . . .	84
4.59	1900 SN-6 in situ optical image (97 % of YS) . . . . .	85
4.60	1900 SN-6 in situ optical image (108 % of YS) . . . . .	85
4.61	Beginning of a propagating crack 1 . . . . .	85
4.62	Beginning of a propagating crack 2 . . . . .	85
4.63	Beginning of a propagating crack 3 . . . . .	86
4.64	Beginning of a propagating crack 4 . . . . .	86
4.65	1850A SN-8 in situ optical image zero load . . . . .	86
4.66	1850A SN-8 in situ optical image (60 % of YS) . . . . .	86
4.67	1850A SN-8 in situ optical image (82 % of YS) . . . . .	87
4.68	1850A SN-8 in situ optical image (106 % of YS) . . . . .	87
4.69	DIC strain map 1 . . . . .	88
4.70	DIC strain map 2 . . . . .	88
4.71	DIC strain map 3 . . . . .	88
4.72	DIC strain map 4 . . . . .	88
4.73	DIC strain map 5 . . . . .	88
4.74	DIC strain map 6 . . . . .	88
4.75	DIC strain map 7 . . . . .	89
4.76	Notch deformation . . . . .	89
4.77	Strain development for a single element . . . . .	90
4.78	A custom mesh for DIC analysis . . . . .	91
C.1	PreProcessor . . . . .	C3
C.2	Input file editor . . . . .	C3
C.3	Grayvalue correction . . . . .	C4
C.4	Multiscale . . . . .	C4
C.5	Results view . . . . .	C5
D.1	1900 SN-4 NbC . . . . .	D1
D.2	1900 SN-3 TiN . . . . .	D2

# List of Tables

2.1	Properties of phases in alloy 718 . . . . .	3
2.2	Size of $\gamma''$ -particles in Inconel 718 . . . . .	3
3.1	Key properties of the examined materials. . . . .	25
3.2	Composition of the materials. . . . .	25
3.3	Heat treatment of the materials. . . . .	25
3.4	Electropolishing parameters . . . . .	27
3.5	Experimental procedure. . . . .	33
3.6	Test matrix . . . . .	37
4.1	Chemical content of spot 1 (large particle) from fine grained 1850A SN-6 . . . . .	41
4.2	Chemical content of spot 3 (small particle) from fine grained 1850A SN-6 . . . . .	42
4.3	Chemical content of spot 5 (matrix) from fine grained 1850A SN-6 . . . . .	42
4.4	Chemical content of spot 1 (large particle) from coarse grained 1900 SN-8 . . . . .	43
4.5	Chemical content of spot 2 (small particle) from coarse grained 1900 SN-8 . . . . .	44
4.6	Chemical content of spot 3 (matrix) from coarse grained 1900 SN-8 . . . . .	44
4.7	Results from the measurement of particle area fraction. . . . .	46
4.8	UTS, YS and microstructure . . . . .	46
4.9	Tensile test fracture results summarized. . . . .	48
4.10	Highest and lowest measured potential . . . . .	50
4.11	Potential-results from the three experiments using the Elek- troniklabor Schrems potentiostat. . . . .	51
4.12	Depth of the brittle area . . . . .	57
4.13	Reduction of area . . . . .	58
A.1	First polishing step after grinding. . . . .	A1
A.2	Second polishing step. . . . .	A1
A.3	Third and final polishing step. . . . .	A1
D.1	Chemical content of the particle from 1900 SN-4. The particle exhibited Nb and C levels indicative of NbC-particles. . . . .	D1
D.2	Chemical content of the particle from 1900 SN-3. This particle exhibited chemical content indicative of TiN-particles. . . . .	D2



---

# List of Equations

2.1	Engineering stress . . . . .	6
2.2	Engineering strain . . . . .	6
2.3	Hall-Petch . . . . .	11
2.4	Cathodic reaction 1 . . . . .	14
2.5	Cathodic reaction 2 . . . . .	14
2.6	Hydrogen absorption . . . . .	15
2.7	Hydrogen leaves the surface 1 . . . . .	15
2.8	Hydrogen leaves the surface 2 . . . . .	15
2.9	Fick's first law . . . . .	16
2.10	Diffusion coefficient . . . . .	16

---

# List of Abbreviations

**1850A** Fine grained material P3A01-1850A

**1900** Coarse grained material P3A01-1900

**AIDE** Adsorption-Induced Dislocation Emission

**BCC** Body Centered Cubic

**CP** Cathodic Protection

**DIC** Digital Image Correlation

**DSS** Duplex Stainless Steel

**EBSD** Electron Backscatter Diffraction

**EDS** Energy Dispersive Spectroscopy

**FCC** Face Centered Cubic

**FS** Fracture Strength

**GB** Grain Boundary

**Glycerol** Used as abbreviation for a 2:1 mixture of glycerol and 85 % ortho-phosphoric acid

**HCP** Hexagonal Close Packed

**HE** Hydrogen Embrittlement

**HEAC** Hydrogen Environment Assisted Cracking

**HEDE** Hydrogen Enhanced Decohesion

**HELP** Hydrogen Enhanced Localized Plasticity

**HIC** Hydrogen Induced Cracking

**HIP** Hot Isostatically Pressed

**HISC** Hydrogen Induced Stress Cracking

**HSC** Hydrogen Stress Cracking, also known as HISC

**ID** Identification

<b>IG</b>	Intergranular
<b>IHAC</b>	Internal Hydrogen Assisted Cracking
<b>IPF</b>	Inverse Pole Figure
<b>KAM</b>	Kernel Average Misorientation
<b>MPa</b>	Megapascal
<b>NHE</b>	Normal Hydrogen Electrode
<b>NTNU</b>	Norwegian University of Science and Technology
<b>ppm</b>	Parts Per Million
<b>RA</b>	Reduction of Area
<b>RT</b>	Room Temperature
<b>SCE</b>	Saturated Calomel Electrode
<b>SEM</b>	Scanning Electron Microscope
<b>SN</b>	Single Notch
<b>SSC</b>	Sulfide Stress Cracking
<b>SSRT</b>	Slow Strain Rate Tensile test
<b>TRIP</b>	Transformation Induced Plasticity
<b>TTF</b>	Time To Fracture
<b>UTS</b>	Ultimate Tensile Strength
<b>wppm</b>	Weight-Parts Per Million
<b>YS</b>	Yield Strength

# Contents

<b>Abstract</b>	<b>iii</b>
<b>Sammendrag</b>	<b>v</b>
<b>Preface</b>	<b>vii</b>
<b>List of Figures</b>	<b>ix</b>
<b>List of Tables</b>	<b>x</b>
<b>List of Equations</b>	<b>xi</b>
<b>List of Abbreviations</b>	<b>xiv</b>
<b>1 Introduction</b>	<b>1</b>
1.1 Background . . . . .	1
1.2 Objective . . . . .	2
<b>2 Theory</b>	<b>3</b>
2.1 Properties of Inconel 718 . . . . .	3
2.2 Fracture Mechanisms . . . . .	4
2.3 Stress and Strain . . . . .	5
2.4 Notch Effects . . . . .	7
2.5 The Effect of Hydrogen on Metals . . . . .	8
2.6 Mechanisms of Hydrogen Embrittlement . . . . .	10
2.7 The Effect of Grain Size on Mechanical Properties . . . . .	11
2.8 The Effect of Grain Size on Hydrogen Embrittlement . . . . .	12
2.9 Sources of Hydrogen . . . . .	13
2.10 Hydrogen from Cathodic Protection . . . . .	14
2.11 Diffusion of Hydrogen in Inconel 718 . . . . .	15
2.12 Trapping of Hydrogen . . . . .	16
2.13 Crack Initiation and Propagation . . . . .	17
2.14 Stepwise Loading Tensile Tests . . . . .	18
2.15 Fractography . . . . .	19
2.16 Digital Image Correlation Technology . . . . .	20
2.17 Electron Backscatter Diffraction . . . . .	22

<b>3</b>	<b>Experimental</b>	<b>25</b>
3.1	Material . . . . .	25
3.2	Specimen Dimensions and Sample Preparation . . . . .	26
3.3	Tensile Test Equipment . . . . .	27
3.4	Optical Microscope Equipment . . . . .	28
3.5	Designing New Electrolyte Chambers . . . . .	30
3.6	Stepwise Tensile Test Procedure . . . . .	32
3.7	Examination in Scanning Electron Microscope . . . . .	35
3.8	EBSD . . . . .	35
3.9	Analysis Using Digital Image Correlation Technology . . . . .	35
3.10	Test Matrix . . . . .	36
<b>4</b>	<b>Results</b>	<b>38</b>
4.1	Material Characterization . . . . .	38
4.1.1	Optical Microscope . . . . .	38
4.1.2	Scanning Electron Microscope . . . . .	39
4.1.3	Particle Fraction . . . . .	45
4.2	Tensile Test Results of Fracture Tests . . . . .	45
4.3	SEM Images - Fracture Tests . . . . .	51
4.3.1	Fine Grains - 1850A SN-1 Air Fracture . . . . .	53
4.3.2	Fine Grains - 1850A SN-4 Hydrogen Fracture . . . . .	53
4.3.3	Coarse Grains - 1900 SN-1 Air Fracture . . . . .	55
4.3.4	Coarse Grains - 1900 SN-5 Hydrogen Fracture . . . . .	55
4.4	Depth of Brittle Area . . . . .	57
4.5	Measurements of Reduction of Area . . . . .	57
4.6	SEM Images - Stop Tests . . . . .	59
4.6.1	Coarse Grained Material: P3A01-1900 SN-1 Air Stop at 128 % of YS . . . . .	62
4.6.2	Coarse Grained Material: P3A01-1900 SN-4 Air Stop at 121 and 127 % of YS . . . . .	63
4.6.3	Coarse Grained Material: P3A01-1900 SN-2 Hydrogen Stop at 120 % of YS . . . . .	65
4.6.4	Coarse Grained Material: P3A01-1900 SN-3 Hydrogen Stop at 120 % of YS . . . . .	67
4.6.5	Coarse Grained Material: P3A01-1900 SN-6 Hydrogen Stop at 122 % of YS . . . . .	69
4.6.6	Coarse Grained Material: P3A01-1900 SN-7 Hydrogen Stop at 116 % of YS . . . . .	71
4.6.7	Coarse Grained Material: P3A01-1900 SN-8 Hydrogen Stop at 112 % of YS . . . . .	72

4.6.8	Summary of Findings from Stop Tests of Coarse Grained Material . . . . .	73
4.6.9	Fine Grained Material: P3A01-1850A SN-6 Air Stop at 115 % of YS . . . . .	74
4.6.10	Fine Grained Material: P3A01-1850A SN-2 Hydrogen Stop at 113 % of YS . . . . .	76
4.6.11	Fine Grained Material: P3A01-1850A SN-5 Hydrogen Stop at 112 % of YS . . . . .	78
4.6.12	Fine Grained Material: P3A01-1850A SN-7 Hydrogen Stop at 108 % of YS . . . . .	79
4.6.13	Summary of Findings from Stop Tests of Fine Grained Material . . . . .	79
4.7	EBSD . . . . .	80
4.8	In Situ Optical Microscope Images . . . . .	84
4.8.1	Coarse Grained Material . . . . .	84
4.8.2	Fine Grained Material . . . . .	86
4.9	An Attempt to Use Digital Image Correlation Technology to Map Strains . . . . .	87
<b>5</b>	<b>Discussion</b>	<b>92</b>
5.1	Material Characterization . . . . .	92
5.2	Fracture Tests . . . . .	92
5.3	Potential . . . . .	93
5.4	Stop Tests - Effects of Hydrogen on Crack Initiation and Propagation . . . . .	93
5.5	Effect of Grain Size on Hydrogen Embrittlement . . . . .	95
5.6	Development of New Equipment and Experimental Setup . . . . .	96
5.7	Test Method . . . . .	97
5.8	Digital Image Correlation - Progress Made and Future Potential . . . . .	98
5.9	Validity of the Results . . . . .	99
<b>6</b>	<b>Conclusion</b>	<b>101</b>
6.1	Conclusion . . . . .	101
6.2	Recommendations for Future Work . . . . .	102
	<b>References</b>	<b>103</b>
	<b>Appendix A</b>	<b>A1</b>
	Parameters for Sample Preparation Using Struers TegraPol-31 . . . . .	A1

<b>Appendix B</b>	<b>B1</b>
Electrolyte Chamber Working Drawing . . . . .	B1
<b>Appendix C</b>	<b>C1</b>
eCorr v4.0 User Guide . . . . .	C1
<b>Appendix D</b>	<b>D1</b>
Additional EDS results from coarse grained 1900 . . . . .	D1
<b>Appendix E</b>	<b>E1</b>
Signed Problem Text . . . . .	E1
<b>Appendix F</b>	<b>F1</b>
Signed Risk Assessment . . . . .	F1





# 1 Introduction

## 1.1 Background

Ni-superalloys are extensively used for subsea applications in the oil and gas industry. One such alloy is UNS N07718, hereafter referred to as Inconel 718, which is utilized due to its high strength and often adequate corrosion resistance. The alloy is widely used in the aerospace, petrochemical and oil and gas industries due to its favorable mechanical properties, structural ability and corrosion resistance, at temperatures ranging from  $-252^{\circ}\text{C}$  up to approximately  $700^{\circ}\text{C}$  [1][2].

Components of Inconel 718 utilized subsea will often be connected to cathodic protection (CP) systems. This causes hydrogen to develop on the surface of the material. Cathodic protection can thereby serve as a source of hydrogen, which can diffuse into the material and cause hydrogen embrittlement (HE), which combined with stress and a susceptible material will lead to hydrogen induced stress cracking (HISC). Nickel has a face centered cubic crystal structure, which exhibits a high solubility of hydrogen, but low diffusivity. Until recently, this contributed to a perception that Ni-alloys would be immune to hydrogen induced stress cracking during subsea use. While they are indeed less susceptible to HISC than many ferritic stainless steel alternatives, in which hydrogen diffuses much faster, it is now a well known fact that Ni-alloys are susceptible to HISC. This has been proven through extensive research [3][4][5][6] and documented field failures [7] [8].

In previous project work performed by the author [9], stepwise tensile loading tests with in situ cathodic polarization were performed. The objective was to investigate the effect of grain size on the hydrogen embrittlement of Inconel 718. The grain size effect was not successfully resolved; however, it was established that in situ cathodic charging led to HISC in tensile specimens of Inconel 718. This was supported by fracture surfaces exhibiting brittle fracture characteristics when examined in scanning electron microscope, as well as reduction in ductility and fracture strength.

This work will continue to investigate the grain size effect on hydrogen embrittlement of Inconel 718. It will also focus on the effect hydrogen has on crack initiation and propagation in the alloy. In addition to this, new equipment will be developed and utilized in order to examine the possibility of using digital image correlation techniques to measure local strains while testing the samples in situ. HISC testing will be performed by stepwise tensile loading under in situ cathodic polarization, in dedicated constant load

equipment. A resolution of the grain size effect would be helpful in future production and design of high performance Ni-components, as would knowledge about the influence of hydrogen on crack initiation.

## 1.2 Objective

There are three main objectives in this work: to examine the effect of hydrogen on crack initiation and propagation; examine the effect of grain size on hydrogen embrittlement of Inconel 718; and attempt to develop a procedure for measuring local strains by using digital image correlation technology in combination with series of images obtained during in situ tensile testing. Experiments will be carried out using the aforementioned tensile loading equipment. Samples of two different grain sizes will be tested. The investigation will also include examination in scanning electron microscope (SEM) and electron backscatter diffraction (EBSD).

## 2 Theory

### 2.1 Properties of Inconel 718

Superalloys are heat-resistant alloys based on nickel, nickel-iron or cobalt, that exhibit a combination of mechanical strength and resistance to surface degradation [10].

Inconel 718 is a Ni-Fe-base superalloy. These alloys have an austenitic matrix, which means that they have a face centered cubic (FCC) crystal structure. Due to their FCC crystal structure, the austenitic Ni-Fe-base superalloys have a high solubility of hydrogen but low diffusion rate. Inconel 718 is widely used in the aerospace, petrochemical and oil and gas industries due to its favorable mechanical properties, structural stability and corrosion resistance at temperatures ranging from  $-252^{\circ}\text{C}$  up to approximately  $700^{\circ}\text{C}$  [1][2]. The Inconel 718 alloys are precipitation strengthened [11]. The alloy normally contains three different intermetallic phases, namely  $\gamma'$ ,  $\gamma''$  and the  $\delta$ -phase. Compositions and crystal structures of the respective phases are summarized in Table 2.1:

**Table 2.1:** Properties of phases in alloy 718 [12].

Phase	Composition	Crystal structure
$\gamma'$	$\text{Ni}_3(\text{Al,Ti})$	Cubic ( $\text{L1}_2$ )
$\gamma''$	$\text{Ni}_3\text{Nb}$	Body Centered Tetragonal ( $\text{D0}_{22}$ )
$\delta$	$\text{Ni}_3\text{Nb}$	Orthorombic ( $\text{D0}_a$ )

Other particles, such as NbC and TiN may also precipitate in Inconel 718 [13] [14] [15]. The basis for the precipitation strengthening of the alloy is formed by  $\gamma'$  and  $\gamma''$ , though  $\gamma''$  is the main strengthening precipitate [1] [16]. Sundararaman et al. reported on the size of  $\gamma''$ -particles in aged Inconel 718 [17]. They found that the size of the ellipsoidal  $\gamma''$ -particles, as measured by the major axis (R), varied between 3.8 and 28.9 nm for varying heat treatments. These findings are displayed in Table 2.2.

**Table 2.2:** Size of  $\gamma''$ -particles in Inconel 718 after different heat treatments [17].

Heat treatment	$\gamma''$ particle size, R (nm)
Solution treated at $1100^{\circ}\text{C}$ , aged at $650^{\circ}\text{C}$ for 75 hours	3.8
Solution treated at $1100^{\circ}\text{C}$ , aged at $750^{\circ}\text{C}$ for 2 hours	7.9
Solution treated at $1100^{\circ}\text{C}$ , aged at $700^{\circ}\text{C}$ for 20 hours	13.7
Solution treated at $1100^{\circ}\text{C}$ aged at $750^{\circ}\text{C}$ for 20 hours	28.6

The  $\delta$ -phase does not contribute significantly to the strengthening of Inconel 718. On the contrary, since both  $\gamma''$  and  $\delta$  are Ni-based, its presence may deplete the matrix of  $\gamma''$ , resulting in a loss of hardenability. The  $\delta$ -phase can provide inhibition of grain growth, but other precipitates, such as carbides, may have the same effect in its absence [12]. Formation of the  $\delta$ -phase is possible in the range of 760 to 980°C, and it can remain stable at temperatures approaching room temperature [1]. The presence of  $\delta$ -phase in Inconel 718 deteriorates ductility, and at high hydrogen concentrations (40 weight-parts per million in the article by Sjøberg and Cornu) its presence will drastically reduce the ductility, as the hydrogen preferentially interacts with the  $\delta$ -phase [5]. It was found by Liu et al. that the hydrogen embrittlement resistance of Inconel 718 can be greatly improved by dissolving  $\delta$ -particles in the material [19] [20]. Research by Galliano et al. also supports the notion that the  $\delta$ -phase has a harmful effect on mechanical properties in the presence of hydrogen [21].

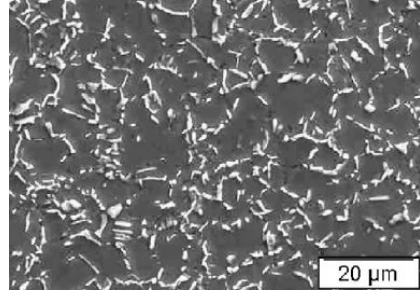


**Figure 2.1:** Example of  $\delta$ -particles precipitated in Inconel 718 [18].

## 2.2 Fracture Mechanisms

Fractures in metals can be classified as either ductile or brittle. A ductile fracture is characterized by an appreciable amount of plastic deformation prior to failure. Severe deformation is usually present at the fracture surface. Brittle fracture is characterized by very little deformation prior to failure, and a rapid rate of crack propagation. Brittle fractures have been observed in BCC and HCP metals, but not in FCC metals unless there are factors contributing to grain boundary embrittlement (e.g. hydrogen) [22].

Tensile fracture of a ductile metal will usually include plastic deformation until a necked region is formed. Many fine cavities, or microvoids, will form in this necked region. The preferred sites for void formation are inclusions and second phase particles [22]. As these microvoids elongate, they will merge and thereby contribute to crack growth by a process of microvoid coalescence. The crack will grow in a direction perpendicular to the load axis until it gets close to the surface, where it will start to propagate along shear planes at a 45° angle to the load axis. The result is a recognizable cup-and-cone fracture, the steps of which are shown in Figure 2.2. This process leads to a dimpled fracture surface, characteristic of a ductile fracture (as

displayed in Figure 2.10 from section 2.15).

Brittle fracture occurs as either transgranular cleavage or intergranular (IG) fracture. Cleavage fracture is the most common, and it occurs as a consequence of a three-step process: first, plastic deformation produces pile-ups of dislocations at grain boundaries; then, build-up of shear stress at the head of pile-ups will nucleate a microcrack; finally, propagation of the microcrack occurs when a sufficient stress level is reached. Intergranular fracture is the formation and propagation of cracks along grain boundaries. In most cases, metals do not fail along grain boundaries. However, if the boundaries have been weakened, intergranular fracture may occur.

A variety of situations can lead to this type of fracture, such as precipitation of brittle phases on the grain boundary, environmentally assisted cracking (such as hydrogen embrittlement) and intergranular corrosion [23]. Hydrogen-induced cracks normally exhibit transgranular features. However, intergranular fracture is possible for some alloy systems [24]. Indeed, fractures in hydrogenated nickel polycrystals were shown to be brittle and intergranular [25] [26]. Robertson et al. proposed that the fracture mode depends on the details of the hydrogen distribution. Transgranular fracture is observed when hydrogen distribution is enhanced at the tip of a notch because that is where the hydrogen concentrates due to the stress field. Intergranular fracture is alternatively observed when there is a higher hydrogen concentration at the grain boundary than at other places in the material [27]. A study of nickel-base alloy UNS N07725 revealed a mixture of transgranular and intergranular fracture in hydrogen charged samples [28].

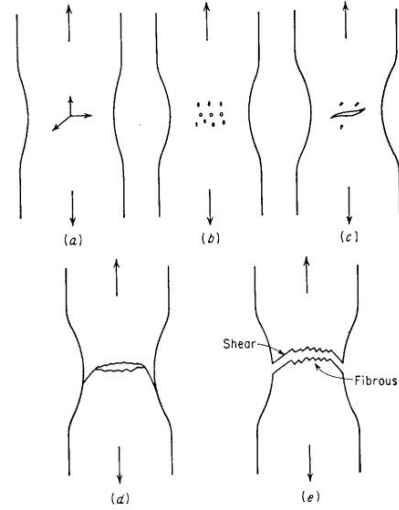


**Figure 2.2:** Formation of a cup-and-cone ductile fracture. Figure from Dieter [22].

### 2.3 Stress and Strain

In tensile testing, the load and elongation are normalized in order to reduce geometrical factors. This results in the parameters of engineering stress (Equation 2.1) and engineering strain (Equation 2.2).

$$\sigma = \frac{F}{A_0} \quad (2.1)$$

Where  $\sigma$  is the engineering stress,  $F$  is the force and  $A_0$  is the original cross sectional area.

$$\varepsilon = \frac{\Delta L}{L_0} \quad (2.2)$$

Where  $\varepsilon$  is the engineering strain and  $\Delta L$  is the difference between the instantaneous length ( $L$ ) and the original length ( $L_0$ ).

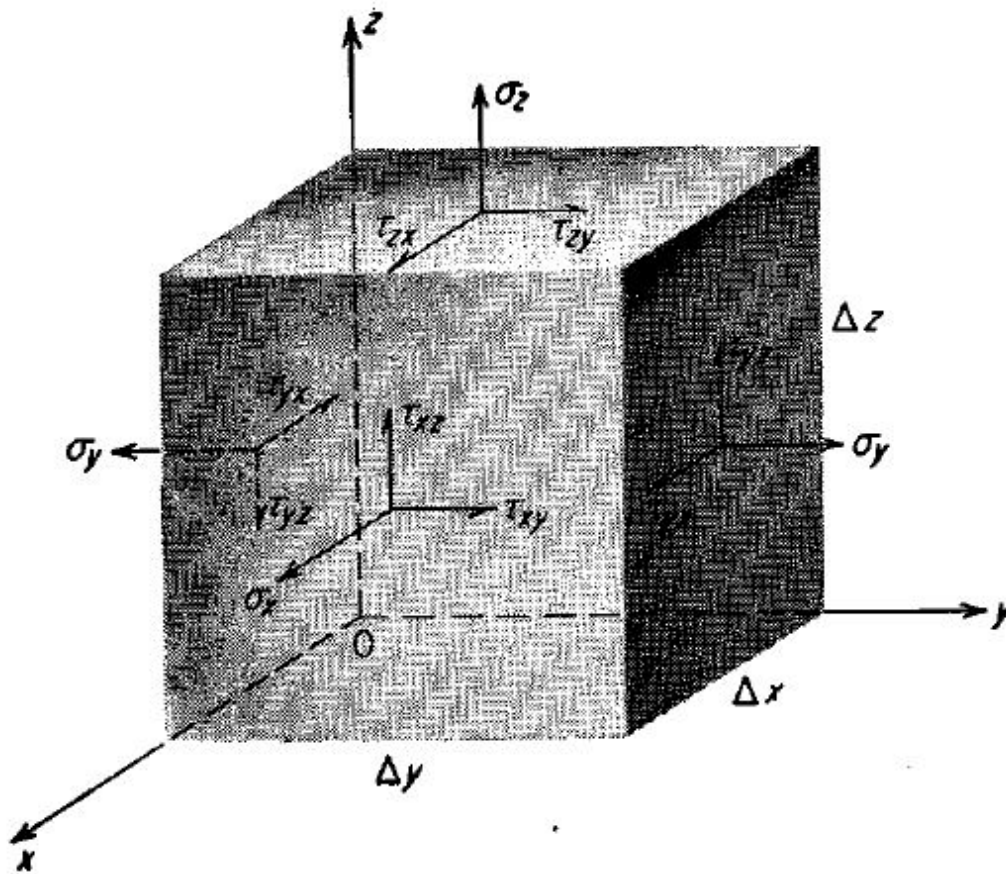


*Figure 2.3: Stresses acting on an elemental cube. Figure from Dieter [22].*

There are three principal ways in which a load may be applied: tension, compression and shear. The total stress can be resolved into two components: a normal stress,  $\sigma$ , perpendicular to  $A$ , and a shear stress,  $\tau$ , working in the plane of the area, as illustrated by Figure 2.3 [22]. The same decomposition is valid for strains.

For any stress state it is possible to define a new coordinate system with axes perpendicular to the planes on which the normal stresses act and on which no shear stresses act. These planes are called principal planes. The stresses and strains normal to these planes are the principal stresses and strains, respectively [22]. For two-dimensional plane stress,  $\sigma_1$  and  $\sigma_2$  will denote the two principal stresses, which occur at  $90^\circ$  angles to each other. Conventionally,  $\sigma_1$  is the greatest principal stress. In complete analogy with principal stress, it is possible to define principal axes (Figures 2.4 and 2.5) in which there are no shear strains, by rotating the axes so that  $\tau$  equals zero. For an isotropic body, the directions of principal strains coincide with the directions of principal stress [22].

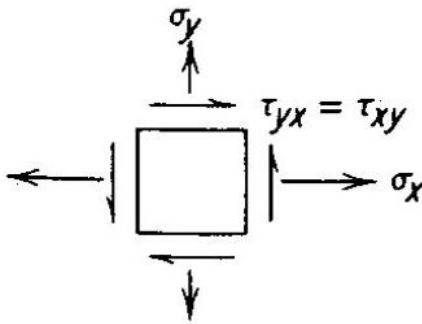


**Figure 2.4:** Illustration of unrotated stress directions. Figure taken from Dieter [22].

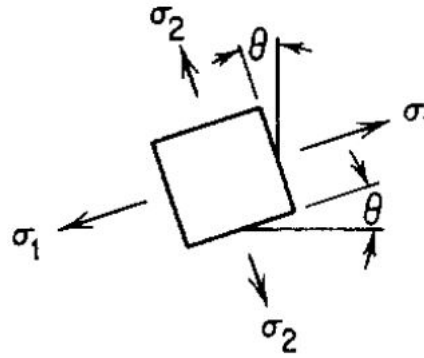


**Figure 2.5:** Illustration of how the axes can be rotated to find principal axes. Figure from Dieter [22].

## 2.4 Notch Effects

In a notched specimen, the notch will create a local stress peak near the root of the notch, as illustrated by Figure 2.6. Still, the most important effect is the fact that it introduces a triaxial state of stress at the notch. In an un-notched tensile specimen, the longitudinal stress alone measures the yielding. The existence of transverse stresses raises the average value at which yielding occurs. Consequently, the nominal strength of a notched sample may be greater than the tensile strength of a smooth sample, and a “notch strengthening” effect in crystalline metals may be observed [22] [29]. Although, in a material sensitive to brittle fracture the increased tensile stresses can exceed the critical value for fracture before plastic yielding occurs [22]. A notch strengthening effect was observed in notched tensile specimens of Inconel 718 in project work performed by the author [9].

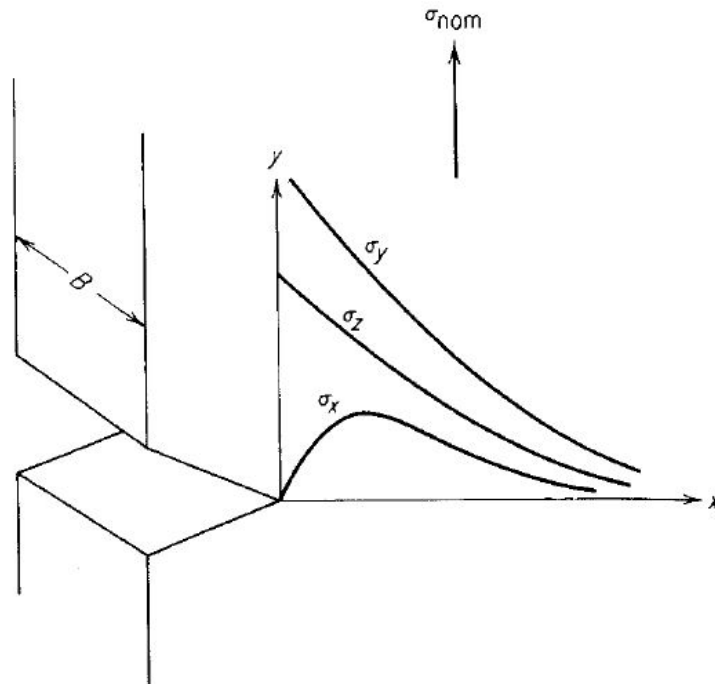


**Figure 2.6:** A representation of the elastic stress distribution at a notch during plane strain. The schematic is taken from Dieter [22].

## 2.5 The Effect of Hydrogen on Metals

The phenomenon of hydrogen embrittlement was first discovered in 1875, when William H. Johnson described the embrittlement of iron and steel [30]. Hydrogen embrittlement (HE) can be defined as a loss of mechanical properties due to the presence of atomic hydrogen and stress in a susceptible material. The consequences of hydrogen embrittlement may be decreased ductility, reduction of fracture strength and brittle fracture. Otherwise ductile materials may exhibit brittle fracture under the influence of hydrogen. Atomic hydrogen diffuses interstitially through the lattice of the metal, and concentrations on the order of parts per million (ppm) may lead to cracking [24]. A common misunderstanding is that hydrogen embrittlement only affects materials with a BCC crystal structure. However, this is a false perception, as HE actually affects most of the important alloy systems. Materials affected by HE includes among others: ferritic and austenitic steels, titanium and nickel-base alloys [23].

Different forms of hydrogen embrittlement exist, many of which are defined in the ISO21457 standard [31]. Hydrogen induced cracking (HIC) involves planar cracking that occurs in carbon and low alloy steel, as a consequence



of hydrogen diffusing into the material and combining at trap sites to form molecular hydrogen. Cracking results from pressurization of trap sites by hydrogen. Therefore, no externally applied stress is needed for HIC [31]. Hydrogen stress cracking (HSC; also known as hydrogen induced stress cracking, HISC) is another form of cracking which results from the presence of hydrogen in a metal and an applied or residual tensile stress. The ingredients of HISC are illustrated in Figure 2.7. Sulfide stress cracking (SSC) is another form of hydrogen induced stress cracking, where atomic hydrogen is produced by acid corrosion on the metal surface. Hydrogen uptake is enhanced by the presence of sulfides [31].

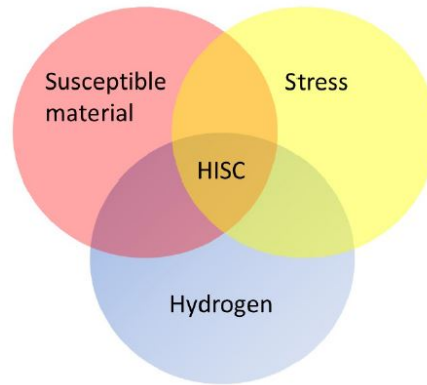


**Figure 2.7:** Illustration of the ingredients necessary for HISC. Figure from Andersen [32].

It is common to differentiate between internal hydrogen assisted cracking (IHAC) and hydrogen environment assisted cracking (HEAC) [33]. The difference between the two is in how hydrogen enters the material. Internal hydrogen assisted cracking implies that hydrogen enters the material prior to use, for instance during manufacturing, processing or welding. Hydrogen environment assisted cracking implies that hydrogen enters the material during use. The embrittlement mechanism is assumed to be the same for both IHAC and HEAC [33].

Research has shown that Inconel 718 is clearly affected by hydrogen embrittlement: In experiments carried out by Fournier et al., the tensile elongation of Inconel 718 was significantly reduced by cathodic hydrogen charging performed either prior to or during deformation [3]. This embrittlement was portrayed by a change from ductile to brittle fracture mode. A Ni-base alloy investigated by Yao et al. also exhibited significant susceptibility to hydrogen embrittlement under both precharged and dynamic charging conditions.

Susceptibility was shown to increase with higher current density and longer charging times [4]. Sjöberg and Cornu found that samples of Inconel 718 which had been precharged with hydrogen, were severely affected by hydrogen embrittlement, as evidenced by a reduction in elongation and reduction of area in tensile testing [5]. The same was found by McCoy et al. using slow strain rate tensile tests on precharged samples of Inconel 718 [6].

## 2.6 Mechanisms of Hydrogen Embrittlement

The mechanisms of hydrogen embrittlement have been widely discussed and are not completely understood. So far, no single theory has been proposed that can explain all instances of hydrogen embrittlement, as different mechanisms appear to dominate under different conditions. A reasonably certain aspect of the controversy of hydrogen embrittlement, is that the search for a single mechanism is probably in vain, and that there are several viable mechanisms to hydrogen-related failure [34]. At the present time, there are four mechanisms of hydrogen embrittlement normally mentioned in the literature. These mechanisms are: Hydrogen Enhanced Localized Plasticity (HELP); Hydrogen Enhanced Decohesion (HEDE); Adsorption-Induced Dislocation Emission (AIDE), in addition to a mechanism involving embrittlement through hydride formation.

In the case of hydride formation, the theory is widely accepted for certain materials and conditions [35]. This mechanism is known to occur only in specific situations. Crack growth in this case is thought to occur by repeated sequences of: (1) hydrogen diffusion to regions of high triaxial stress in front of crack tips; (2) nucleation and growth of a hydride phase; (3) cleavage of the hydride when a critical size is reached; (4) arrest of crack propagation at the interface between hydride and matrix [35]. A hydride mechanism only occurs in the temperature and strain-rate regimes where hydrogen has time to diffuse to regions ahead of crack tips, and only at temperatures where the hydride phase is stable [26] [35].

Hydrogen Enhanced Localized Plasticity (HELP) is a model based on increased plasticity in local regions, as the name implies. The model is based on observations that the presence of hydrogen in solid solution will increase the mobility of dislocations, increasing the dislocation density at crack tips, which creates regions with localized high deformation. The enhanced dislocation mobility occurs through an elastic shielding effect by the hydrogen on the dislocations at crack tips. This local softening of the material results

in cracking by microvoid coalescence along preferred crystallographic planes. Macroscopically, the resulting fracture is still perceived as brittle [35] [36] [37]. In non hydride-forming systems, the evidence for HELP is strong, based on microscopic observations of crack-tip behavior and fracture surfaces [34].

Hydrogen Enhanced Decohesion (HEDE) is based on the hypothesis that hydrogen lowers the cohesive strength by dilation of the atomic lattice and hence lowers the fracture energy [36]. This leads to a weakening of metal-metal bonds near crack tips by high local hydrogen concentrations, such that tensile separation of atoms (decohesion) will occur in preference to slip [35]. This model is applicable to brittle failure, but it cannot explain the fractures accompanied by plasticity. The decohesion model claims that there should be a critical hydrogen atom concentration for which brittle fracture occurs [37].

Adsorption-Induced Dislocation Emission (AIDE) was first proposed by Lynch [38]. This mechanism is based on a weakening of interatomic bonds by the presence of hydrogen, with crack growth occurring by localized slip [35].

The four mechanisms mentioned above may occur together at times, although one will usually dominate [26] [35]. The dominant mechanism depends on variables like material, microstructure, environment, temperature and others which affect the fracture path and fracture mode.

## 2.7 The Effect of Grain Size on Mechanical Properties

The mechanical properties of a material are greatly affected by the grain size. Because a greater total grain boundary area will contribute to impede dislocation movement more than a lesser grain boundary area, a smaller grain size leads to harder and stronger materials than a larger grain size [24]. This relationship is expressed by the Hall-Petch equation (eq. (2.3)):

$$\sigma_y = \sigma_0 + k_y d^{-\frac{1}{2}} \quad (2.3)$$

In the Hall-Petch equation,  $\sigma_y$  is the yield strength,  $d$  is the average grain diameter,  $\sigma_0$  and  $k_y$  are material constants. Figure 2.8 illustrates in simple terms how more dislocations can pile up in larger grains than in smaller ones, creating a larger driving force to cross the grain boundary.

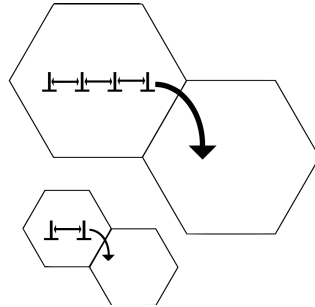


**Figure 2.8:** Illustration of how more dislocations can pile up at the grain boundary of a larger grain than in a smaller grain. Schematic from R. Mittal [39].

## 2.8 The Effect of Grain Size on Hydrogen Embrittlement

There is conflicting evidence in the literature with respect to the effect of grain size on hydrogen embrittlement [40]. Several aspects make this a strenuous subject to investigate. For instance, it is difficult to change the grain size of a material without also affecting other aspects of the microstructure. Therefore, it is challenging to isolate the effect of grain size on the susceptibility to hydrogen embrittlement. It is important to ensure that other parameters, such as amount of precipitates, are as equal as possible when testing the effect of grain size. Differing results in the literature may be a result of differences in the degree of segregation in different grain size materials, because of different structures obtained in the effort to produce varying grain sizes, or because of grain size dependent differences in diffusion [40].

Sjöberg and Cornu performed tensile tests on precharged samples of fine grained and coarse grained material of cast Inconel 718 [5]. Hydrogen embrittlement of fine grained material was larger than in coarse grained material. This was attributed to grain boundary hydrogen sensitivity. Haaland also attained results that suggested fine grained Inconel 718 material was more embrittled by hydrogen than coarse grained material [41]. This was evidenced by higher loss in ductility and a higher hydrogen content in the fine grained material.

In contrast, Latanision and Opperhauser found that larger grain sizes were correlated with a more substantial loss in fracture strength and ductility, compared with smaller grain sizes of polycrystalline nickel [25] [42]. The proposed explanation implied that hydrogen entry occurs preferentially at grain boundaries, due to the segregation of recombination poisons, such as

Sb and Sn, to the grain boundaries. The authors stated that even in 99.995 % pure nickel, the Sb and Sn impurity contents are 2 weight-parts per million (wppm) and 6 ppm, respectively<sup>1</sup>. When testing high-strength low alloy steels in 45 MPa gaseous hydrogen atmosphere by notched tensile tests, Takasawa et al. found that fracture stresses increased with smaller grain sizes, indicating that grain refinement is an effective way of reducing hydrogen embrittlement in high-pressure hydrogen atmospheres [43]. The positive effect of grain refinement was claimed to be due to the reduction in the mass of hydrogen per unit grain boundary area with smaller grains. In 2205 duplex stainless steel (DSS), Chou and Tsai reported that the resistance to hydrogen-assisted cracking decreased with increasing grain size [44]. Similar results were obtained with hot isostatically pressed DSS in a study by Lauvstad et al. [45].

It seems the literature generally agrees on the effect of grain size in steels. However, the literature has thus far failed to provide a clear-cut answer to what effect grain size has on hydrogen embrittlement in nickel alloys such as Inconel 718. Several conflicting results have been presented, a fact that points out the need for further research on the subject.

## 2.9 Sources of Hydrogen

Hydrogen may be introduced into the material from sources such as wet welding electrodes, cathodic protection (CP), a gaseous hydrogen atmosphere or corrosion reactions.

The coverage of hydrogen on the metal surface depends both on the mechanism of the hydrogen evolution on the substrate and on the current density or potential [37]. Certain compounds, such as  $S^{2-}$  and  $HS^-$ , will hinder the recombination of hydrogen atoms on the metal surface. Such compounds are referred to as recombination poisons [37]. The fact that these poisons prevent the hydrogen from recombining, ensures that the amount of atomic hydrogen on the surface increases, hence increasing the probability of absorption into the material [25].

---

<sup>1</sup>The article does not differentiate between weight or volume ppm. It is assumed here that wppm was intended.

## 2.10 Hydrogen from Cathodic Protection

Cathodic protection is one of the most effective ways of preventing corrosion and may in some cases completely stop corrosion from occurring. Cathodic protection is based on the principle of applying a current to a material in need of corrosion protection. The current may be applied by using an imposed current or connecting the material to a sacrificial anode. This applied current will cause the electrode potential of the material to stay in the immune area of the Pourbaix diagram (Figure 2.9), or to stay under a certain protection potential. In effect, the protected material is turned into a cathode in an electrochemical cell when polarized cathodically [46]. When cathodic protection is applied, hydrogen production at the surface of the metal is one of the possible cathodic reactions. This supplies hydrogen that may diffuse into the material.

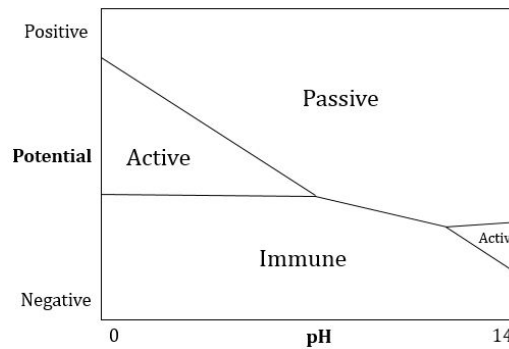
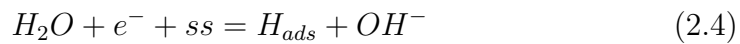


**Figure 2.9:** Pourbaix diagram of a hypothetical metal.

For subsea applications of Inconel 718, cathodic protection systems are commonly used for corrosion protection. It is useful to consider the electrochemistry behind CP in order to understand its importance as a hydrogen source. If cathodic protection is applied in seawater, there are two reactions that can lead to the formation of atomic hydrogen [36]:

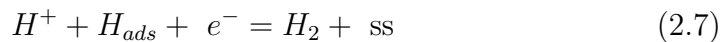


Here,  $ss$  is a surface site available for hydrogen adsorption. Hydrogen that is capable of diffusing into the metal is produced by the hydrogen from these

reactions chemisorbing at the metal surface. Chemisorption is a form of adsorption which involves a chemical reaction between the surface and the atoms to be adsorbed. When adsorbed hydrogen is absorbed, the process can be expressed by Equation 2.6 [36].



Adsorbed hydrogen may leave the surface instead of being absorbed. This happens when the hydrogen forms gaseous  $H_2$  and leaves the surface, according to Equations 2.7 and 2.8 [36].



## 2.11 Diffusion of Hydrogen in Inconel 718

The austenitic Ni-Fe-base superalloys have a high solubility of hydrogen, but low diffusion rate, due to their FCC crystal structure. Grain boundaries may act as preferential paths for hydrogen diffusion in FCC materials, providing accelerated diffusion in the vicinity of the boundaries. Brass et al. have shown that there are cases of preferential diffusion along grain boundaries in stable FCC structures, such as nickel or stainless steel [47] [48]. However, the diffusion may slow down when the dislocation density stored in the grain boundary is substantial [47]. When a stress is applied, hydrogen will diffuse under a stress gradient toward places of high stress [37]. Dislocations may enhance the hydrogen motion, especially in FCC structures, where the lattice diffusivity is low at room temperature [49]. Hydrogen transport by mobile dislocations can lead to local hydrogen enrichment in the dislocation pile-ups near precipitates, which favors crack initiation [21]. Deformation was proven to enhance hydrogen diffusion in a Ni-base alloy when tested by Yao et al. [4].

Kimura and Birnbaum stated that the kinetics of intergranular embrittlement of high purity nickel from an external hydrogen source are controlled by grain boundary diffusion [50]. Additionally, they proposed that segregation of elements to grain boundaries (GB) may affect both the hydrogen

grain boundary diffusion and the critical hydrogen concentration required for intergranular fracture. For instance, carbon segregated at the GBs resulted in a decrease in hydrogen diffusivity, but an increase in critical hydrogen concentration for intergranular fracture.

The movement of hydrogen from an area of high concentration to an area of low concentration can be described by Fick's law, presented in Equation 2.9.

$$J_x = -D \left( \frac{\partial C}{\partial x} \right)_t \quad (2.9)$$

In Fick's law, J represents the flux, D is the diffusion coefficient and  $\frac{\partial C}{\partial x}$  is the concentration gradient as a function of time. An indication of the speed of diffusion in a material is given by the diffusion coefficient. Robertson [51] has measured the diffusion coefficient in Inconel 718, which is presented in equation (2.10), where R is the gas constant [cal/Kmol] and T is the temperature [K]:

$$D_{\text{Inconel 718}} = 1.07 \times 10^{-2} \times \exp \left( \frac{-11,900}{RT} \right) \left[ \frac{\text{cm}^2}{\text{s}} \right] \quad (2.10)$$

At room temperature, equation (2.10) gives  $D = 2 \times 10^{-11} \text{ cm}^2/\text{s}$  for Inconel 718. In comparison, an average diffusion coefficient of  $7.60 \times 10^{-7} \text{ cm}^2/\text{s}$  was found for X70 grade steel, by Skjellerudsveen et al. [52]. Clearly, diffusion in Inconel 718 is much slower than in X70 grade steel. As can be seen from the general expression for D in equation (2.10), the diffusion for both materials will increase as the temperature rises.

Values of hydrogen content after charging with hydrogen were obtained by Haaland [41], in a master's thesis examining the same materials as will be tested in the present work. Haaland measured a hydrogen content of 9.42 weight-parts per million for coarse grained P3A01-1900 Inconel 718 material and 11.56 wppm for fine grained P3A01-1850A Inconel 718. These samples had been precharged with hydrogen at a potential of -1050 mV Ag/AgCl for 5 days at 120°C.

## 2.12 Trapping of Hydrogen

Hydrogen atoms normally reside at interstitial positions in the metal. However, in reality, the hydrogen atoms may be trapped by various defects within the material. Any metallurgical defect may act as a trap for hydrogen [37].



Although, typical trapping sites are dislocations, vacancies, grain boundaries, phase boundaries, inclusions and precipitates [36].

Traps are classified as either reversible or irreversible. Hydrogen may easily depart from the reversible traps, as these traps have low energy. The irreversible traps demand more energy in order to release the hydrogen atoms, and will therefore be more effective in trapping the hydrogen. If the hydrogen were only occupying interstitial sites, it would start to diffuse out of the material once hydrogen charging was terminated. However, the traps will contribute to keep the hydrogen in the material. It has been shown by Pound that TiC and NbTi(CN) precipitates may act as irreversible traps in Inconel 718 [53]. The irreversible traps may serve as initiation points for fracture.

### 2.13 Crack Initiation and Propagation

Crack initiation and propagation can be studied by loading a specimen until a crack begins to form, and subsequently investigating this crack using appropriate techniques. Laureys et al. [54] performed characterization of cracks in Transformation Induced Plasticity (TRIP) steels, by loading samples to a stress level between yield strength and the onset of necking. These were notched samples, either charged with hydrogen or un-hydrogenated. The resulting cracks were characterized by SEM and EBSD, which allowed Laureys et al. to conclude that the presence of hydrogen in the material promoted stress-induced fracture ahead of the notch, while in the absence of hydrogen, only strain-induced cracks were observed at the notch root. The difference between the two types of cracking is as follows: formation of a strain induced crack is a strain controlled event which happens at the notch root where the local strains are highest; this leads to the formation of large cracks propagating from notch root. Stress induced cracks are induced by hydrogen and form at a distance ahead of the notch where the local tensile stresses are highest. Laureys et al. also proposed that failure occurred by the hydrogen enhanced localized plasticity (HELP) mechanism, as indicated by elevated strains surrounding the cracks and crack tips. Methods similar to those used by Laureys et al. will be utilized to investigate crack initiation and propagation in Inconel 718 in this master's thesis.

Lufrano and Sofronis [55] performed numerical simulations of the hydrogen concentration ahead of notches and cracks in steel specimens with rounded notches. They found that when fracture is accompanied by large strains at the notch root, most of the hydrogen is trapped close to the notch root,

and cracking is initiated there; whereas if limited plastic strains precede the fracture, most of the hydrogen will reside at the normal interstitial lattice sites at the maximum hydrostatic stress peak location some distance from the notch root, which would result in microcracks initiating there. McCoy et al. [6], who tested hydrogen precharged samples of Inconel 718 by slow strain rate tensile tests (SSRT), found that crack initiation did not start until the material was plastically strained to levels above the yield strength. In hydrogen charged samples of superalloy UNS N07725 tested by Hanson et al. [28], cracks were found to propagate predominantly along grain boundaries, with no evidence of slip band cracking or fracture initiation at carbides, supporting the importance of grain boundaries to the fracture process.

In 1984, Tabata and Birnbaum [56] presented the first direct observations of the hydrogen related fracture process in iron, by having a crack propagate in vacuum, stopping the crack, changing the environment to gaseous  $H_2$ , and observing the subsequent crack propagation in situ in an electron microscope. They showed that crack propagation in iron was greatly affected by gaseous hydrogen, as the crack velocity was increased by the addition of hydrogen. Crack propagation could also be stopped by removing the  $H_2$  gas and replace it with inert gas [56][27].

Stenerud et al. [57] proposed that secondary cracks in the surface of specimens of Inconel 718 affected by HISC, appeared due to the embrittled surface layer of the material. They reported that several secondary cracks could initiate in the brittle surface, until one finally would reach a threshold size and propagate until complete fracture occurred. The center of the samples exhibited ductile features.

## 2.14 Stepwise Loading Tensile Tests

The stepwise tensile testing performed in this work will be based on a procedure developed by Roy Johnsen et al. [36]. In the article initially describing this method, it was found that a stepwise increase in load and direct loading gave the same critical load. The stepwise tensile testing procedure have since been further developed by students at NTNU, and involves loading a tensile specimen stepwise until fracture. The stepwise loading permits exposure to different environments over time. In the present work, this is utilized to cathodically charge samples with hydrogen during tensile testing.

Rising step load bend tests were performed by Kernion et al. [58], in which specimens were exposed to hydrogen via in situ cathodic polarization in 3.5

wt % NaCl aqueous solution. Load was applied at fixed time intervals, and the subsequent drop in load (i.e. sample relaxation after load application) was used to determine the step at which crack growth occurred. Contributions to load drop were reported to include crack growth, sample relaxation (cold creep) and relaxation of the testing apparatus. A similar method of using the amount of sample relaxation to detect crack growth was utilized in the present master's thesis.

## 2.15 Fractography

Fractography is the examination of fracture surfaces in order to gain information on the nature of the fracture. This is most often performed using a scanning electron microscope (SEM). The ability to investigate the actual fracture surface, as well as having high resolution and a good depth of focus, are reasons why the SEM is an important tool in fracture analysis. The appearance of the fracture surface will indicate what type of fracture mechanism has occurred.

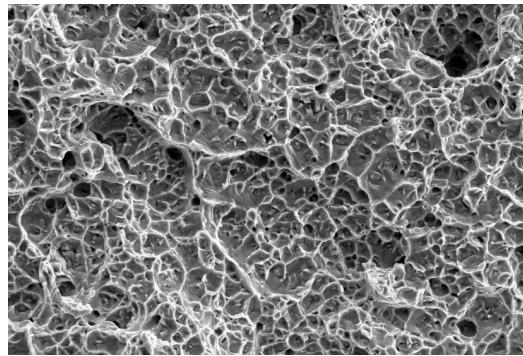


**Figure 2.10:** Typical example of a ductile fracture. 1000X magnification.

A transgranular cleavage fracture is characterized by a flat faceted surface, as shown in Figure 2.11. These facets will usually exhibit river markings, where the river pattern indicates the direction of crack propagation. For intergranular fracture, the fracture surface will exhibit clean facets which have fractured along grain boundaries, as in Figure 2.12. A ductile fracture will be recognized by its distinct dimpled surface, as shown in Figure 2.10.

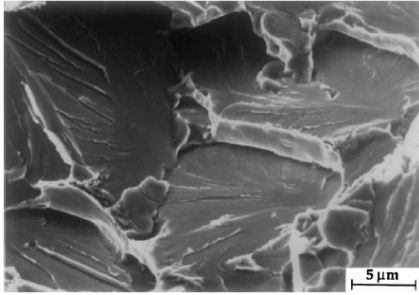


**Figure 2.11:** Typical example of a brittle cleavage fracture, displaying the characteristic river markings. Figure from Anderson [23].

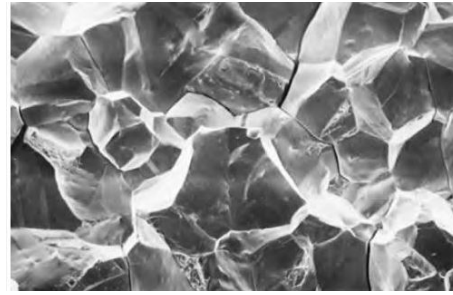


**Figure 2.12:** Typical example of a brittle intergranular fracture. 50X magnification. Figure from Callister [24].

## 2.16 Digital Image Correlation Technology

Using DIC, each pixel of the image is given a grayscale value between 0 and 255. The program then uses a correlation function to minimize the difference in grayscale values between the current and reference image. The DIC software used in this study, eCorr, uses a "finite element" type of mesh. Digital Image Correlation (DIC) technology relies on innovative non-contact optical techniques for measuring strain and displacement. It is a technique that may prove to be ideally suited for the study of crack propagation and material deformation in real-world applications [59]. DIC works by comparing digital photographs of a component or specimen at various stages of deformation. The system tracks blocks of pixels, in order to measure surface displacement. This can be used to build up full field 2D and 3D deformation vector fields and strain maps. DIC will be used in the present work, in an attempt to map the development of strains in tensile specimens of Inconel 718, from optical microscope images obtained during in situ stepwise tensile testing. Figures 2.13 and 2.14 display examples of a mesh and a strain map, respectively, created in the DIC software eCorr v4.0.

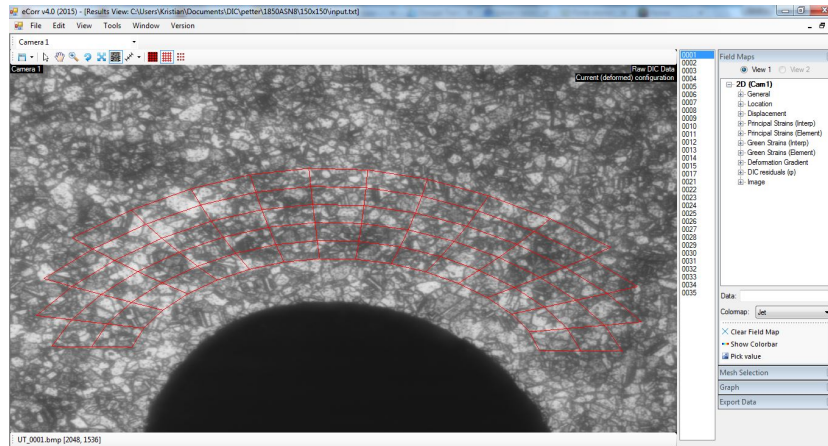


**Figure 2.13:** A mesh used for DIC analysis in the software *eCorr v4.0*. The mesh (in red) is laid over an image of a fine grained Inconel 718 sample that has been etched in order to achieve the desired contrast.

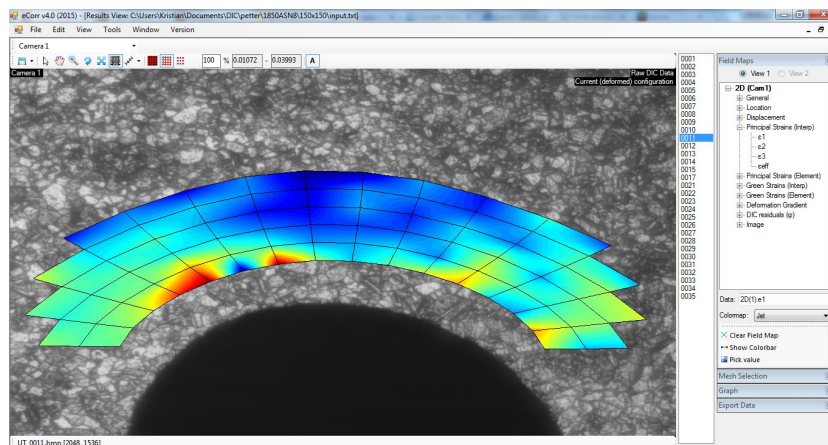


**Figure 2.14:** A map of principal strains has been created using *eCorr v4.0*. Warmer colors represent higher strain value.

In many cases, the natural surface of the material may have sufficient image texture for DIC to work without the need for any special surface preparation [59]. It is, however, important that the surface pattern has a random texture. The DIC software measures variations in grayscale. Therefore, a random pattern with large variations in grayscale is ideal. An example of contrast and pattern that is suitable for DIC is presented in Figure 2.15. A wide variety of sources may be employed to obtain the images that are to be used for DIC analysis, including conventional digital cameras, microscopes, macrosopes or scanning electron microscopes.

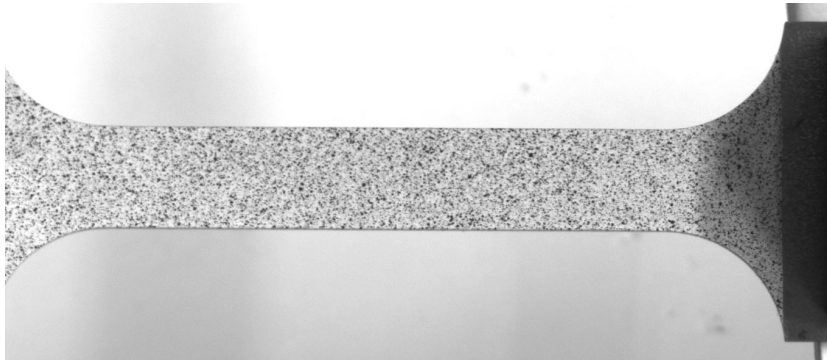


**Figure 2.15:** An example of the type of black and white contrast that is optimal for DIC analysis. This sample has been painted in order to achieve the desired appearance. The picture is from the eCorr v4.0 documentation site [60].

## 2.17 Electron Backscatter Diffraction

Electron backscatter diffraction (EBSD), when used as an additional characterization technique to SEM, makes it possible to determine grain orientations, texture and phase identification. EBSD patterns are generated on a phosphor screen by backscatter diffraction of a stationary beam of high energy electrons from a volume of approximately 20 nm deep in the specimen [61]. The specimen is tilted  $70^\circ$  in order to increase the intensity of the electron backscatter pattern by reducing the path length of the backscattered electrons. This results in the characteristic Kikuchi pattern seen as gray lines in figure 2.16.

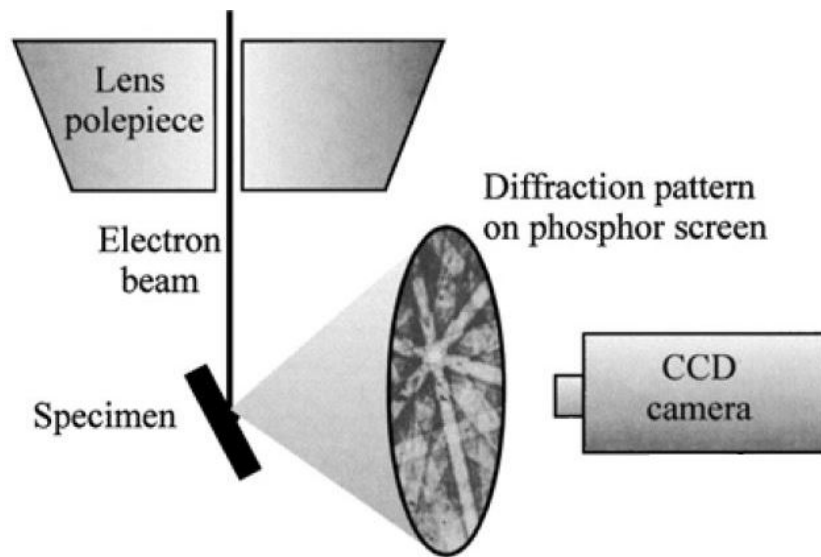


**Figure 2.16:** Illustration of the setup used to produce electron backscatter diffraction. A high energy beam of electrons hits the tilted specimen, creating an EBSD pattern when backscattered electrons hit the phosphor screen. Figure from Humphreys [62].

Every point in a specimen surface will result in different backscatter patterns. These patterns are analyzed by specialized software to derive the crystal orientation at each point. In the present work, EBSD will be used to attain color coded grain maps and kernel average misorientation (KAM) maps, in order to analyze the location of cracks and the surrounding dislocation density. In a grain map, each point in the image is colored according to the crystallographic direction that points along the direction normal to the image plane (Figures 4.52 and 2.18). In a KAM map, the mean of the scalar misorientation between groups of pixels is mapped [61]. The kernel average misorientation map is useful when there are areas of the sample in which the local misorientation is high (e.g. regions of high dislocation density).

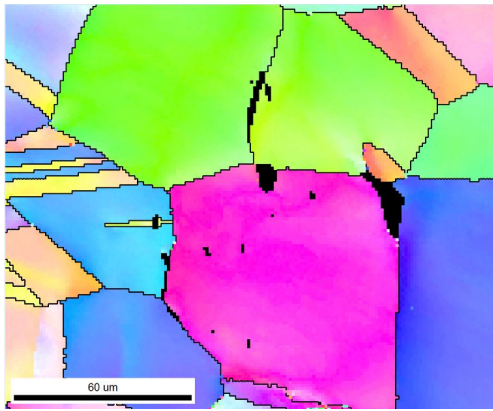


**Figure 2.17:** Example of a color coded grain map.

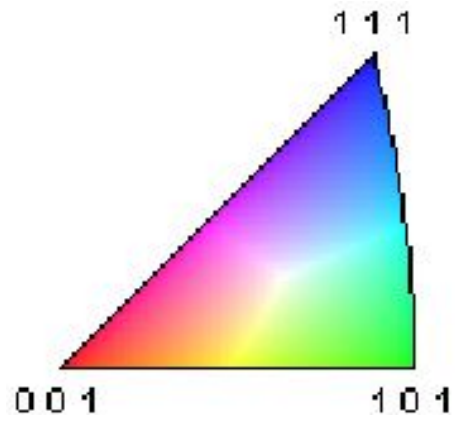


**Figure 2.18:** Orientation triangle showing how the colors are assigned to various orientations.



## 3 Experimental

### 3.1 Material

Two versions of the same Inconel 718 alloy were tested in this study: one coarse grained material (P3A01 - 1900) and one fine grained (P3A01 - 1850A). The microstructures are displayed in Figures 3.1 and 3.2. For simplicity, P3A01 - 1900 and P3A01 - 1850A will usually be referred to as 1900 and 1850A, respectively. In the material characterization work, fine grained material with two different designations was used, namely 1850A and 1850B. These are samples from the same material, only from slightly different parts of the ingot. Materials were supplied by the manufacturer ATI Metals. The manufacturer also supplied information on the ultimate tensile strength (UTS), yield strength (YS) and other key properties of the two alloys. Grain sizes of the same materials were measured by Haaland [41]. Both materials were Inconel 718 with low carbon (C), low nitrogen (N) and high niobium (Nb) compositions. Key properties of the materials are presented in Table 3.1. The composition of this specific alloy is presented in Table 3.2. Heat treatments are shown in Table 3.3.

*Table 3.1: Key properties of the examined materials.*

Material ID	UTS [MPa]	YS [MPa]	Microstructure	Average grain size [ $\mu\text{m}$ ]
P3A01 - 1850A	1498	1293	Fine grained	11.5
P3A01 - 1900	1341	1109	Coarse grained	95.0

*Table 3.2: Composition of the materials.*

Element	C	S	Al	Co	Cr	Fe	Mo	Nb
Wt %	0.004	0.0006	0.53	0.01	17.64	18.64	2.88	5.35
Element	Ni	P	Si	Ti	O	N	B	
Wt %	Bal.	0.009	0.02	1	<0.0005	0.0029	0.005	

*Table 3.3: Heat treatment of the materials.*

Sample type	Content	Heat treatment
P3A01 - 1900 P3A01 - 1850A P3A01 - 1850B	Low C and N Higher Nb	Hold 718°C/8h - Cool at 37.7°C/h to 621°C - Hold at 621°C/8h - Air Cool

In making of the materials, P3A01-1850A and P3A01-1850B were intended to have coarse microstructures. This failed to materialize when the ingot

size was scaled up from laboratory tests. Instead, they achieved fine grained microstructures. Therefore, these materials could be used as fine grained material in the present work, even though all the materials underwent the same heat treatment.

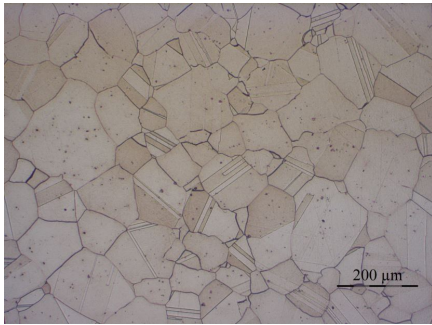


**Figure 3.1:** P3A01 - 1900:  
Coarse grained material (100X).

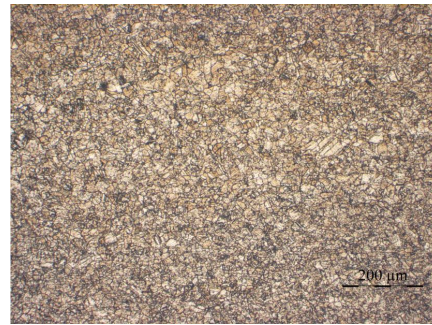


**Figure 3.2:** P3A01 - 1850A:  
Fine grained material (100X).

### 3.2 Specimen Dimensions and Sample Preparation

The samples for tensile testing had a t-bone shape and a notch cut into the middle of the gauge length. The notch was 2 mm deep, with a 200  $\mu\text{m}$  radius at the notch root. Dimensions of the samples are shown in Figure 3.3.

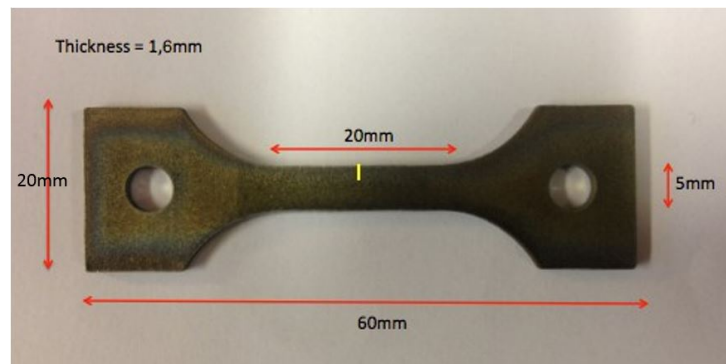


**Figure 3.3:** Dimensions of the tensile test samples. The notch, marked in yellow, is 2 mm deep.

Preparation of the notched tensile samples was performed by first grinding the two larger sides of the sample with 800 grit Struers SiC paper. The grinding was followed by mechanical polishing down to 1  $\mu\text{m}$  using a Struers TegraPol-31 automatic polishing machine. The parameters used for automatic polishing are described in Appendix A. The 1.6 mm thin sides of the

samples, as well the inside of the notch, were subjected to grinding with 800 and 1200 grit Struers SiC papers. Polishing was not possible in these areas. The samples were subjected to cleaning with soap and water, using a cotton swab, between each polishing step. Figure 3.4 displays a sample polished to 1  $\mu\text{m}$ . After grinding and polishing, the samples were etched for a duration of approximately 15 minutes in Kallings etch no. 2 [63] (constituted by 2 g  $\text{CuCl}_2$ , 50 ml HCl and 50 ml ethanol) in order to make the microstructure visible in optical microscope.



*Figure 3.4: Appearance of a sample after grinding and polishing.*

If the sample were to be examined by EBSD after tensile testing, the sample was electropolished on both sides of the gauge length in a Struers LectroPol-5 electropolishing machine (after testing and investigation in SEM was completed). The electrolyte used was Struers A2 (constituted by 910 ml of Struers A2-I [64] and 78 ml Struers A2-II [65]). The parameters used in electropolishing are shown in Table 3.4.

*Table 3.4: Parameters developed for electropolishing.*

Electrolyte	Voltage [V]	Flow rate	Time [s]	Temperature [ $^{\circ}\text{C}$ ]
A2	45	14	12	10

### 3.3 Tensile Test Equipment

The basis for the tensile testing was a ME-Meßsysteme GmbH load cell, with a capacity of 1 Ton equivalent load. A tensile sample was mounted in the machine as shown in Figure 3.5. The load cell was mounted to the desk by use of two vices to reduce vibration and make the setup stable during increase of the load. Increasing or decreasing the load was achieved by cranking the

machine by hand using a wrench. Data from the load cell was recorded by connecting the cell to a computer with dedicated software.

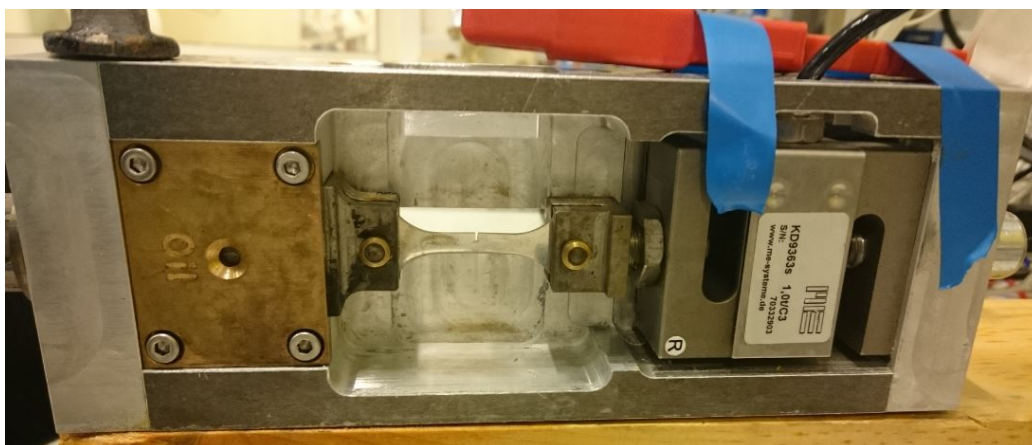


*Figure 3.5:* Tensile test setup for testing a reference sample in air. The red clip taped to the tensile machine is for connecting to a reference electrode and is not used when testing in air.

### 3.4 Optical Microscope Equipment

It was decided that new equipment should be obtained prior to the start of this work. Previous equipment had proved inadequate in the effort to obtain useful pictures from the in situ tensile testing. A new microscope, objective, camera and light source were ordered, with the hope that better image quality might allow the use of Digital Image Correlation software (DIC) to analyze pictures obtained during testing. Part of the objective of this work has therefore been to develop a test procedure and setup that would allow analysis of the strain field around the notch in the tensile specimen, by use of the new equipment and DIC software. To the authors knowledge, DIC analysis has not previously been combined with in situ tensile testing, and would thereby present a novelty in the field of hydrogen embrittlement research.

The microscope consisted of a Mitutoyo<sup>TM</sup> video microscope unit with a Mitutoyo<sup>TM</sup> M PLAN APO 10X objective and was directly connected to a EO 3112C color LE USB digital camera and MI-15 illuminator light source. This gave a total magnification of approximately 160X. At first, the microscope was mounted on a x-y-micro movement stage, allowing fine focus of the image, as well as moving the microscope across the specimen surface in one direction (either sideways or up and down). The digital camera was connected to

a computer where images could be viewed and saved, using uEye Cockpit software from IDS Imaging Development Systems GmbH. This initial setup is displayed in Figure 3.6.



*Figure 3.6: Initial setup for the microscope showing the microscope connected to a 10X objective, digital camera, light source and micro movement stage. The digital camera is connected to a computer.*

Because the optical microscope equipment had not been used in previous work, the setup was subject to gradual change. As the equipment was used, aspects that could be improved revealed themselves.

After using the initial optical microscope setup for the first experiments, gradual improvements were made until arriving at the final setup used in this work. Part of the problem with the initial setup was that it was very sensitive to vibrations from movement and other adjacent experiments in the laboratory. It was also problematic that the microscope could only be moved in x and y directions, not in the z direction. To alleviate these problems, the microscope was fastened to a height-adjustable plate using screws, which in turn was fastened to the x-y-micro movement stage. This allowed movement in three directions, as well as reducing much of the vibrations. To further reduce the issues with vibrations, the whole setup was moved to a room separate from other experiments. The final setup is displayed in Figures 3.7 and 3.8.



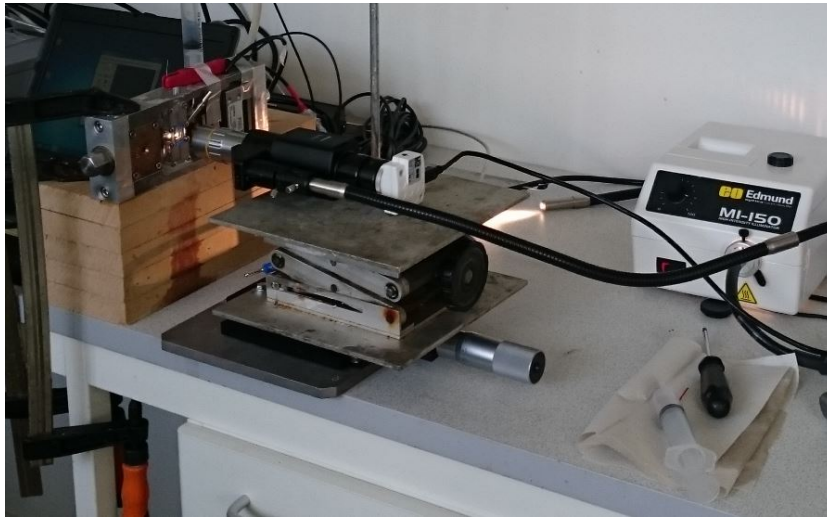


*Figure 3.7: Final setup for the optical microscope equipment, showing the microscope connected to a 10X objective, digital camera and light source; this time fastened to a height-adjustable plate, which in turn was fastened to the micro movement stage. The digital camera is connected to a computer.*



*Figure 3.8: Final setup viewed from above.*

### 3.5 Designing New Electrolyte Chambers

Electrolyte chambers were developed in master's theses and preceding project works by Haaland [41], Stenerud [66] and Krosness [67]. These two-part electrolyte chambers allow for exposure to an electrolyte and cathodic polarization of the sample during testing. The chambers were made of Poly

Carbonate and were held together by eight stainless steel screws (as seen in Figure 3.9). The front side of the chambers had been polished to obtain a transparent finish to allow microscopic examination of the sample surface during testing. However, in the project work prior to this master's thesis, performed by the author [9], visibility was found to be an issue. Bubbles gathering on the surface was also found to be a problem when attempting to photograph the specimen surface.



**Figure 3.9:** *The old design for the electrolyte chambers. The front panel is made from polycarbonate, polished to make the sample visible.*

On the basis of this, it was determined that new chambers should be developed. The goal was to design new chambers that allowed for an equal amount of electrolyte on both sides of the sample, in addition to incorporating a glass window in front of the specimen in order to enhance visibility. New front parts were designed for this purpose, the sketches for which are included in appendix B. The front halves were made of plexiglass. Fabrication was performed by the fine-mechanical workshop at The Faculty of Natural Sciences and Technology at NTNU. The back part of the chamber was kept unchanged. Therefore, the backside designed by Haaland, Stenerud and Krosness was used together with the new fronts. Pictures of the new chambers can be seen in Figures 3.10 and 3.11.

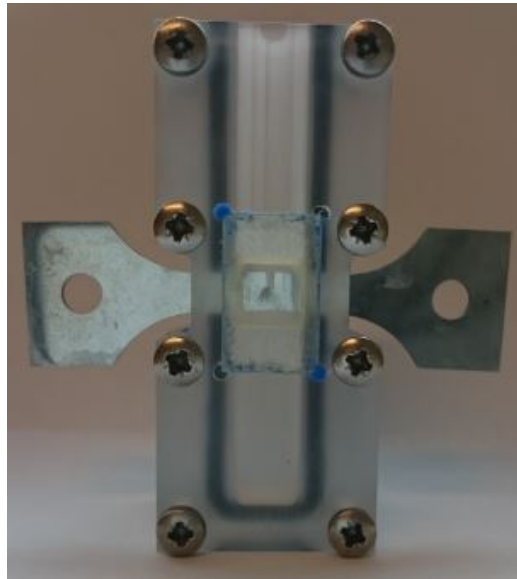


**Figure 3.10:** The new design for the electrolyte chambers. There is a glass plate covering a hole in the middle of the front panel, providing a window with high visibility to the sample.

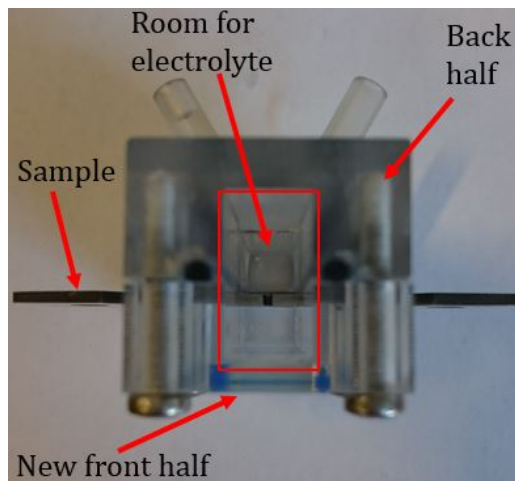


**Figure 3.11:** The new electrolyte chamber viewed from the top.

### 3.6 Stepwise Tensile Test Procedure

The samples were first measured in order to calculate the cross section area and the proper load. Measurements of the cross section was performed using a Leica<sup>TM</sup> MEF4M optical microscope in order to accurately measure the



height of the sample at the notch. A Mitutoyo<sup>TM</sup> digital caliper was used to measure the width and length of the sample.

There were two types of tensile experiments performed in this work: "fracture tests" and "stop tests". The fracture tests were, as the name implies, strained stepwise until fracture. The purpose of the fracture tests was to gain a reference value for when the samples fractured, in addition to be able to examine the fracture surfaces of the specimens after testing. The stop tests were strained in the same way, but were stopped at the point where a crack could be detected. The purpose of the stop tests was to investigate the crack initiation and propagation in Inconel 718 under the influence of hydrogen. Some of the stop tests were stopped at lower loads, in order to examine when and where cracks would initiate in the microstructure. The procedures for the two types of experiments are shown in Table 3.5.

**Table 3.5:** *Experimental procedure.*

Experiment	Initial load	Subsequent loading procedure	Experiment end
Fracture test	100 % of YS	4 % of YS every hour	Complete fracture
Stop test	100 % of YS	4 % of YS every hour	Stopped when a crack was detected

Aside from when the experiments ended, fracture tests and stop tests followed the same procedures. The starting point for loading was at 100 % of the yield strength supplied by ATI metals. The samples were held at this load for one hour, before the load was increased by 4 % of YS and held for another hour. This procedure was continued until the experiment ended. Percent of yield strength was chosen as a measure for the load in order to compare the two different materials, as well as to compare results with previous work in which this measure had been used. A graph illustrating the loading-curve of such an experiment is shown in Figure 3.12. The experiments were performed at room temperature (RT). The samples were subjected to in situ cathodic polarization during testing with a constant current density of -1 mA/cm<sup>2</sup>. The galvanostatic polarization was achieved through connection to a Gamry<sup>TM</sup> potentiostat. The current density was arbitrarily chosen to achieve a high degree of hydrogen evolution on the surface of the sample. Pictures of the material surface were taken with the microscope at each load, and the current density, along with the potential, was monitored throughout the experiment.

Three of the experiments, namely 1900 SN-3, 1850A SN-7 and 1850A SN-8, utilized an Elektronlabor Schrems PGU-10V-1A-E potentiostat instead of the Gamry<sup>TM</sup> potentiostat. The Elektronlabor Schrems potentiostat was

used for the experiments that were moved to a separate room in order to reduce vibrations from adjacent equipment.

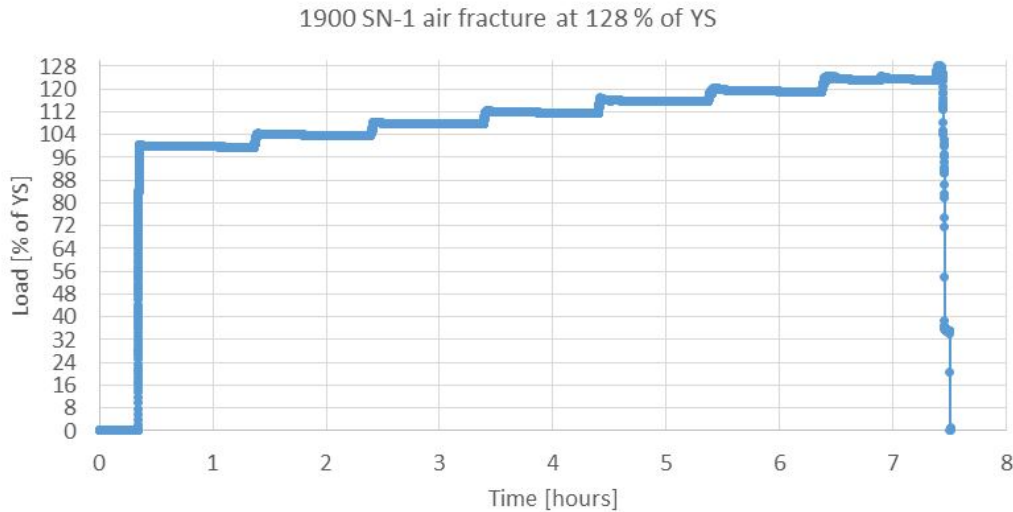


**Figure 3.12:** A graph illustrating the loading procedure of the tensile tests.

During the load increases, the current was paused in order to avoid bubbles on the surface, such that clear pictures of the microstructure could be obtained. The 4 % load increase was achieved by raising the load in increments of about 50 N over a period of approximately 15 minutes, with pictures taken at each increment in order to document the gradual changes in the microstructure. The purpose of this was to obtain a series of pictures that could be analyzed with digital image correlation software. After the load had been increased by 4 % of YS, the current was turned on again and run for another hour.

All experiments, except for one, were cathodically polarized in a 2:1 mixture of glycerol and 85 % ortho-phosphoric acid ( $\text{H}_3\text{PO}_4$ ). This solution had a pH of -0.30 at room temperature. The 2:1 mixture of glycerol and 85 % ortho-phosphoric acid will be referred to as Glycerol for the remainder of this thesis. One sample was tested in a 3.5 % NaCl solution, in order to examine whether or not there would be a difference in image quality of the optical microscope images. The NaCl solution had a pH of 6.58 at room temperature. For Glycerol, a  $\text{Hg}/\text{Hg}_2\text{SO}_4$  (saturated  $\text{K}_2\text{SO}_4$ ) reference electrode was used. A saturated calomel reference electrode (SCE) was utilized for the NaCl solution.

### 3.7 Examination in Scanning Electron Microscope

After tensile testing, all samples were subjected to examination in a scanning electron microscope (SEM). The objective for the stop-tested samples was to examine the crack initiation sites and propagation paths at high magnification. For the fractured samples, the goal was to determine the nature of the fracture by examining the fracture surface.

The samples were examined in one of two SEMs: either a Zeiss Supra 55VP Low Vacuum Field Emission SEM or a Zeiss Ultra 55 Limited Edition Field Emission SEM. EDAX Energy dispersive spectroscopy (EDS) was used to investigate chemical content while in the SEM. Before examination in SEM, the samples were cleaned in an ultrasonic bath for 2 minutes.

### 3.8 EBSD

Only a few samples were selected for EBSD analysis. These were selected on the basis of an investigation of the sample surface in SEM, revealing cracks that would be suitable for EBSD. Before EBSD analysis could be performed, the samples had to be prepared by electropolishing, using the parameters described in 3.4. EBSD was used to collect color coded grain maps and kernel average misorientation (KAM) maps, in order to analyze the location of cracks and the surrounding dislocation density. This is useful in determining the initiation points of cracks and the mechanism of hydrogen embrittlement.

A Zeiss Supra 55VP SEM with an EBSD detector was used to obtain diffraction patterns from the sample surface. NORDIFF software was used to obtain a diffraction pattern from the SEM and the pattern was indexed by the EDAX OIM software. TSL OIM software was used to construct color coded grain maps and kernel average misorientation maps.

### 3.9 Analysis Using Digital Image Correlation Technology

One of the main objectives of this work was to examine the possibility of using digital image correlation software to analyze the optical microscope images obtained during testing. A procedure for performing such analysis had to be developed, as this had not previously been performed on images from in situ hydrogen tensile testing. Several aspects of the experimental setup needed to be optimized, leading to the final setup described in section 3.6.

---

The software used in this work was eCorr v4.0, which was developed by Egil Fagerholt at SIMLab. The software is available online with accompanying documentation [60]. The eCorr software uses a finite element type of mesh to track the movement of blocks of pixels, in order to track the strain in the imaged surface.

Using the series of images obtained from the experiments, the eCorr software was utilized in an attempt to measure the strain field near the notch. For the sake of future continuation of this work, a user guide based on the experiences from this project was created. This is included in appendix C.

### 3.10 Test Matrix

In the preliminary testing of the equipment, a few samples with two notches and a few samples without notch were used to test the equipment and develop the initial experimental setup. This has affected the system for naming the samples used in the experiments: samples with a single notch were designated the letters SN (Single Notch). All samples have also been given a sample number, in addition to a number describing the type of material. A coarse grained sample could for instance be named 1900 SN-1; meaning single notched sample 1 from the coarse grained material P3A01-1900. Correspondingly, a fine grained sample could be named 1850A SN-3; meaning single notched sample 3 from the fine grained material P3A01-1850A.

In order to study crack initiation, the stop tests were planned to be stopped at various levels of load. The purpose was to examine the material surfaces at stages ranging from the first initiated cracks to the surface condition just before fracture. Initially, only two samples of each material was planned to be strained until fracture: one of each material in air and one of each in electrolyte with in situ cathodic polarization. A test matrix is presented in Table 3.6. This table presents the actual treatment of each sample. Due to the difficulty of stopping an experiment just before a sample fractures, some experiments that was meant to be stopped, were actually continued until fracture. Additionally, due to the manual nature of loading the samples, it was challenging to stop experiments at the exact planned load. Therefore, Table 3.6 presents a test matrix containing the actual outcome of each experiment, including the load at which the experiments were stopped.

*Table 3.6: The final outcome of the experiments, presented as a test matrix.*

Material	Name	Tested in	Fracture/stopped [% of YS]	in MPa
1900	SN-1	air	fracture at 128 %	1420
1900	SN-2	Glycerol	stop at 120 %	1333
1900	SN-3	3.5 % NaCl	stop at 120 %	1326
1900	SN-4	air	stop 121 %	1338
1900	SN-5	Glycerol	fracture at 123 %	1366
1900	SN-6	Glycerol	stop at 121 %	1341
1900	SN-7	Glycerol	stop at 116 %	1289
1900	SN-8	Glycerol	stop at 112 %	1246
1850A	SN-1	air	fracture at 115 %	1483
1850A	SN-2	Glycerol	stop at 113 %	1463
1850A	SN-3	air	fracture at 116 %	1502
1850A	SN-4	Glycerol	fracture at 115 %	1490
1850A	SN-5	Glycerol	stop at 112 %	1446
1850A	SN-6	air	stop at 115%	1494
1850A	SN-7	Glycerol	stop at 108 %	1400
1850A	SN-8	Glycerol	fracture at 111 %	1425

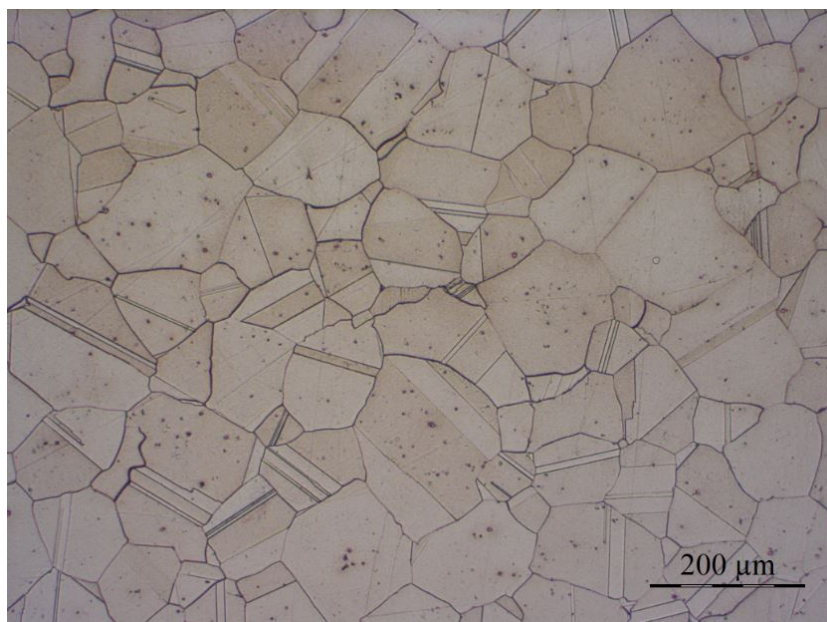
## 4 Results

### 4.1 Material Characterization

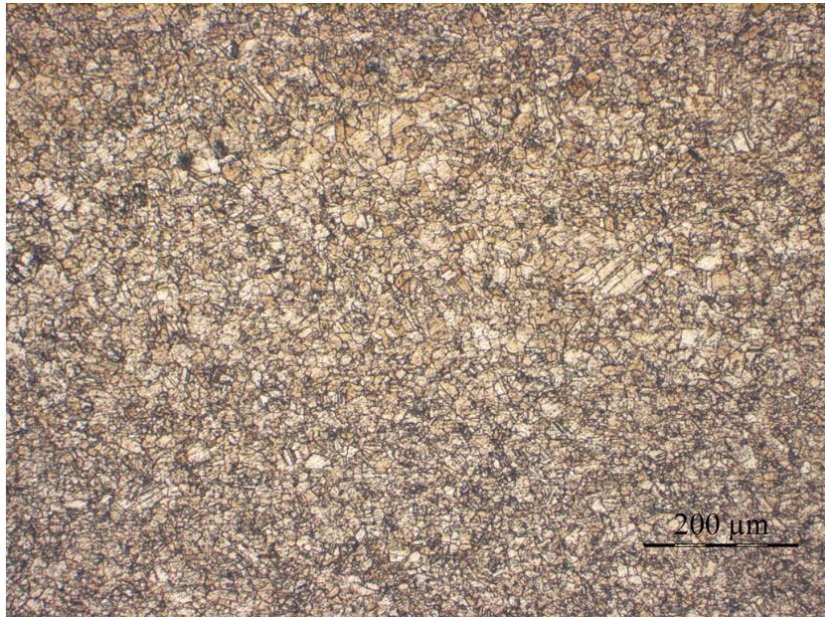
In order to establish the grain size, microstructure and particle content of the materials, a characterization was performed utilizing optical microscope and scanning electron microscope techniques. It was especially important to investigate the differences in particle content with regard to type, size, shape and amount, as these can affect the susceptibility to hydrogen embrittlement.

#### 4.1.1 Optical Microscope

Micrographs of the two examined grain sizes are displayed in Figures 4.1 and 4.2. In order to make the microstructure visible in optical microscope, the samples were etched for a duration of approximately 15 minutes in Kallings etch no.2 [63] after grinding and polishing. The images were obtained with a Leica<sup>TM</sup> MEF4M optical microscope, using a 10X objective. The ocular lens of the microscope contributed another 10X magnification, making the total magnification approximately 100X.



*Figure 4.1: Microstructure of the coarse grained P3A01-1900 material. 100X magnification in optical microscope.*



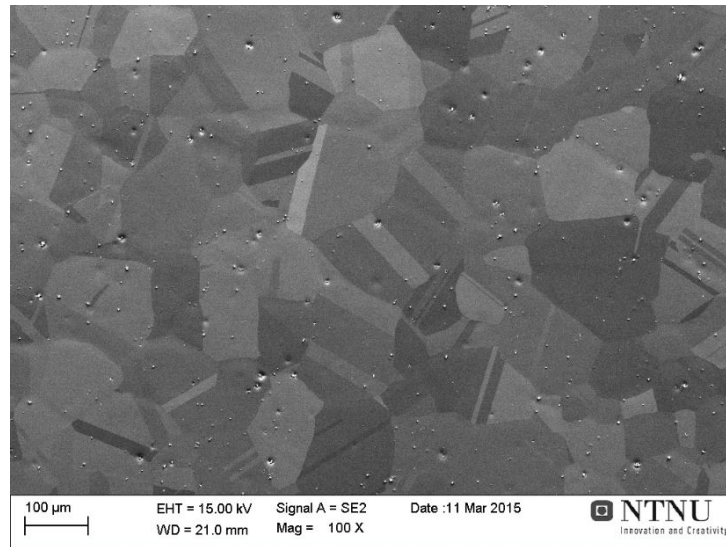
**Figure 4.2:** *Microstructure of the fine grained P3A01-1850B material. 100X magnification in optical microscope.*

Figure 4.1 illustrates twinning in the microstructure of the coarse grained material. The fine grained material also exhibited twins. Black spots believed to be particles were also visible. These were examined further by SEM and EDS in the following sections.

#### 4.1.2 Scanning Electron Microscope

Materials of both grain sizes were investigated in the SEM, using secondary electron signal, z-contrast with backscatter electron signal and EDAX Energy Dispersive Spectroscopy chemical analysis. Figure 4.3 shows a secondary electron microscope image of the coarse grained 1900 microstructure. Figure 4.4 shows a SEM image of the fine grained 1850B material. Particles in the coarse grained 1900 material are seen to be spherical. Most of the particles in the fine grained 1850B material have a rectangular shape. The size of the particles in both materials were in the order of 2  $\mu\text{m}$ , although there were variations in size.





**Figure 4.3:** Microstructure of the coarse grained P3A01-1900 material in SEM. The particles are spherical. The electropolishing treatment has etched the areas around particles, giving the impression that the particles are placed in small dimples. 100X magnification.

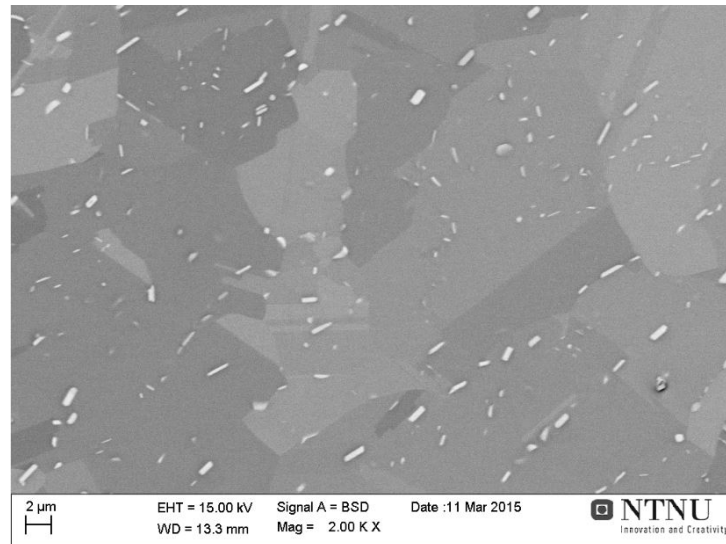


**Figure 4.4:** Microstructure of the fine grained P3A01-1850B material in SEM. The particles are rectangular and are scattered throughout the microstructure. 2000X magnification.

In order to examine the particles observed in the SEM images, chemical analysis was performed using EDAX EDS software. In Figure 4.5 a SEM



image illustrating the spots examined by EDS is shown for fine grained 1850A SN-6.

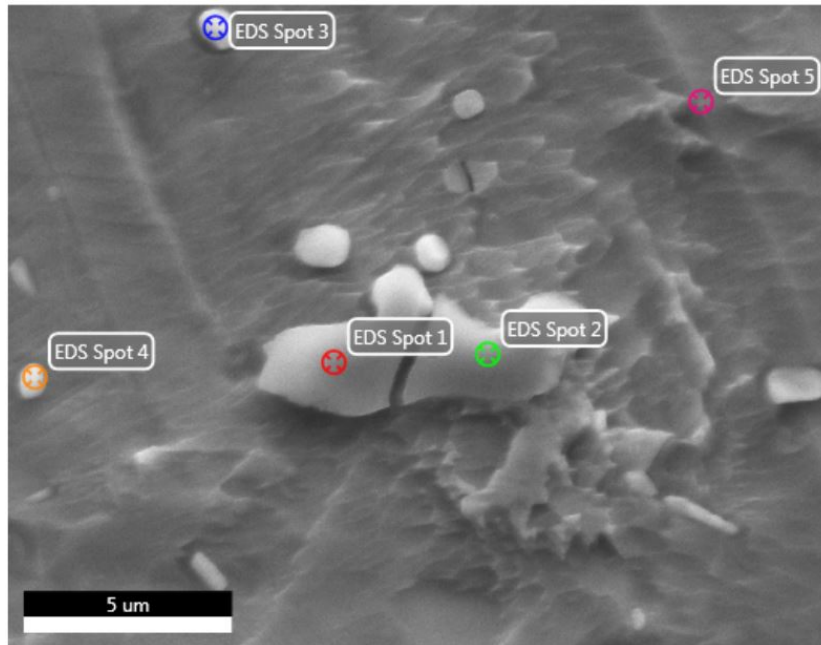


*Figure 4.5:* A map of spots examined by EDS in fine grained sample 1850A SN-6.

Tables 4.1, 4.2 and 4.3 present the measured chemical content from spots displayed in Figure 4.5.

*Table 4.1:* Chemical content of spot 1 (large particle) from fine grained 1850A SN-6

Element	Weight %	Atomic %	Error %
C	4.69	11.28	10.93
N	23.81	49.1	9.16
Al	0.55	0.59	12.99
Nb	3.94	1.22	6.45
Mo	1.06	0.32	17.61
Ti	40.8	24.6	1.69
Cr	5.72	3.18	4.63
Fe	5.83	3.01	4.66
Ni	13.61	6.7	3.61

**Table 4.2:** Chemical content of spot 3 (small particle) from fine grained 1850A SN-6

Element	Weight %	Atomic %	Error %
C	8.92	33.54	12.92
N	0.02	0.05	99.99
Al	0.95	1.59	14.72
Nb	17.47	8.49	5.01
Mo	2.2	1.04	12.54
Ti	1.93	1.82	9.92
Cr	5.36	4.65	4.44
Fe	6.62	5.35	4.25
Ni	56.54	43.48	2.4

**Table 4.3:** Chemical content of spot 5 (matrix) from fine grained 1850A SN-6

Element	Weight %	Atomic %	Error %
C	11.65	38.6	11.28
N	0.15	0.42	99.99
Al	0.85	1.26	15.48
Nb	3.77	1.62	9.56
Mo	2.51	1.04	10.73
Ti	0.93	0.77	14.74
Cr	15.97	12.22	2.42
Fe	17.03	12.13	2.84
Ni	47.13	31.94	2.59

Spots 1 and 2 (Table 4.1) on the large cracked particle, exhibited elevated levels of titanium and nitrogen, indicating that the particle could be a TiN-particle. Spots 3 and 4 (Table 4.2), exhibited elevated levels of niobium, indicating that the the smaller white particles are  $\delta$ -particles. Note that the ratio of Ni to Nb is 3:1, appropriate for  $\delta$ . As a reference, the chemical content of the matrix was also measured. Spot 5 (matrix, Table 4.3) exhibited chemical content very close to what was given as the actual composition in Table 3.2. The carbon content is almost equal for all spots, indicating that the carbon measured is contamination from inside the SEM chamber, according to senior engineer Yingda Yu at NTNU.

In Figure 4.6, a SEM image illustrating the spots examined by EDS is shown for coarse grained 1900 SN-8.

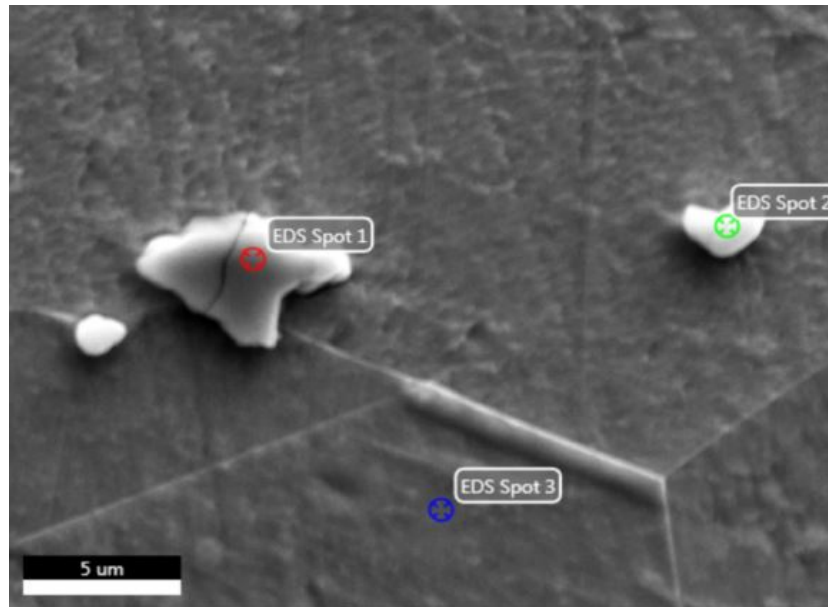


**Figure 4.6:** A map of spots examined by EDS in coarse grained sample 1900 SN-8.

Tables 4.4, 4.5 and 4.6 present the measured chemical content from spots displayed in Figure 4.6.

**Table 4.4:** Chemical content of spot 1 (large particle) from coarse grained 1900 SN-8

Element	Weight %	Atomic %	Error %
C	2.15	5.38	9.09
N	22.75	48.93	7.38
Al	0.37	0.41	8.09
Nb	3.84	1.25	2.35
Mo	0.58	0.18	7.74
Ti	66.22	41.65	1.32
Cr	1.14	0.66	5.46
Fe	1.12	0.61	5.9
Ni	1.83	0.94	5.41

**Table 4.5:** Chemical content of spot 2 (small particle) from coarse grained 1900 SN-8

Element	Weight %	Atomic %	Error %
C	15.76	47.24	10.48
N	6.13	15.76	13.91
Al	0.33	0.44	10.58
Nb	55.44	21.49	1.25
Mo	2.05	0.77	7.1
Ti	11.86	8.91	2.91
Cr	1.93	1.34	4.98
Fe	1.96	1.26	5.32
Ni	4.56	2.79	3.53

**Table 4.6:** Chemical content of spot 3 (matrix) from coarse grained 1900 SN-8

Element	Weight %	Atomic %	Error %
C	1.25	5.73	13.77
N	0	0	99.99
Al	0.52	1.07	11.9
Nb	4.31	2.56	5.49
Mo	2.35	1.35	6.56
Ti	1.06	1.22	4.88
Cr	17.96	19.04	1.81
Fe	18.64	18.4	2.14
Ni	53.92	50.63	2.17

Spots 1 on the large cracked particle exhibited elevated levels of titanium and nitrogen (Table 4.4), indicating that the particle is a TiN-particle. Spot 2 exhibited elevated levels of niobium and carbon (Table 4.5), indicating that the particle might be NbC. The measurement of the 1900 SN-8 sample showed low carbon content, except for spot 2, further indicating that the particle is NbC. The chemical content of spot 3 (matrix, Table 4.6) exhibited chemical contents very close to what was given as the actual composition in Table 3.2. EDS examinations of two more coarse grained 1900 samples are included in appendix D, for further supporting evidence. These measurements support that the smaller spherical particles in the 1900 material may be NbC-particles, and that the coarse particles may be TiN.

The two materials appear to contain different types of particles. The fine grained 1850A seems to contain  $\delta$ -particles, in addition to coarse TiN-particles.

Visual inspection of the fine grained samples in SEM have shown that the smaller rectangular particles (believed to be  $\delta$ ) far outnumber the large Ti-rich particles.

The coarse grained 1900 seems to primarily contain spherical NbC-particles, but also coarse TiN-particles. No signs of  $\delta$ -particles were found in this material.

### 4.1.3 Particle Fraction

An image analysis software, iSolution<sup>TM</sup>, was used to manipulate the contrast of the SEM images and measure the particle area fraction of the materials. The software could automatically provide the particle area fraction based on the difference in grayscale of particles and matrix after the contrast had been adjusted. Figures 4.7 and 4.8 display manipulated SEM images of the coarse grained and fine grained material, respectively, showing particles in white.



*Figure 4.7: P3A01 - 1900: Coarse grained material. 250X magnification. Particle area fraction of 0.12 %.*

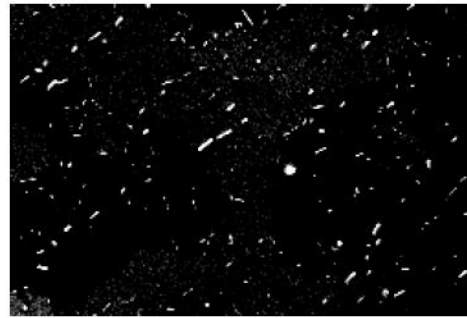


*Figure 4.8: P3A01 - 1850B: Fine grained material. 2000X magnification. Particle area fraction of 1.44 %.*

Five measurements were taken from both materials. The average particle area fraction is used as the area fraction in this work. For the fine grained material, both 1850A and 1850B were measured. These are samples from the same material, only from slightly different parts of the ingot. Table 4.7 shows the results from measuring particle area fraction in the fine grained and coarse grained material.

## 4.2 Tensile Test Results of Fracture Tests

This section presents the results from the experiments where samples were strained until fracture. The fracture tests were performed in order to provide references for which levels of load the stop tests should be stopped at. The

**Table 4.7:** Results from the measurement of particle area fraction.

Material ID	Microstructure	Particle area fraction [%]	Standard deviation
1900	Coarse grained	0.12	0.064
1850A 1850B	Fine grained	1.44	0.299

fracture experiments are the same as those performed in the preceding project work to this master's thesis [9]. The graphs presented in Figures 4.9 and 4.10 give the results from the experiments, but also serve to illustrate how the stepwise loading experiments were performed. It can be seen from the figures that the load was increased stepwise by 4 % of yield strength once every hour. The fracture strengths were recorded and are presented in Table 4.9. This shows that cathodic polarization to promote hydrogen evolution on the surface leads to a reduction in fracture strength. Even though the sample size from the fracture tests is small, these results display the same tendency of lower fracture strengths for samples tested in hydrogen, as was found in the project work. A table reiterating the properties of the examined materials is given in Table 4.8.

**Table 4.8:** UTS and YS of both materials, including stress corresponding to 4 % of YS, which was the standard load increment.

Material	Microstructure	UTS [MPa]	YS [MPa]	4 % of YS [MPa]
P3A01-1850A	Fine grained, rectangular $\delta$ - and coarse TiN-particles (1.44 %)	1498.2	1292.7	51.7
P3A01-1900	Coarse grained, globular NbC- and coarse TiN-particles (0.12 %)	1341	1109.4	44.4

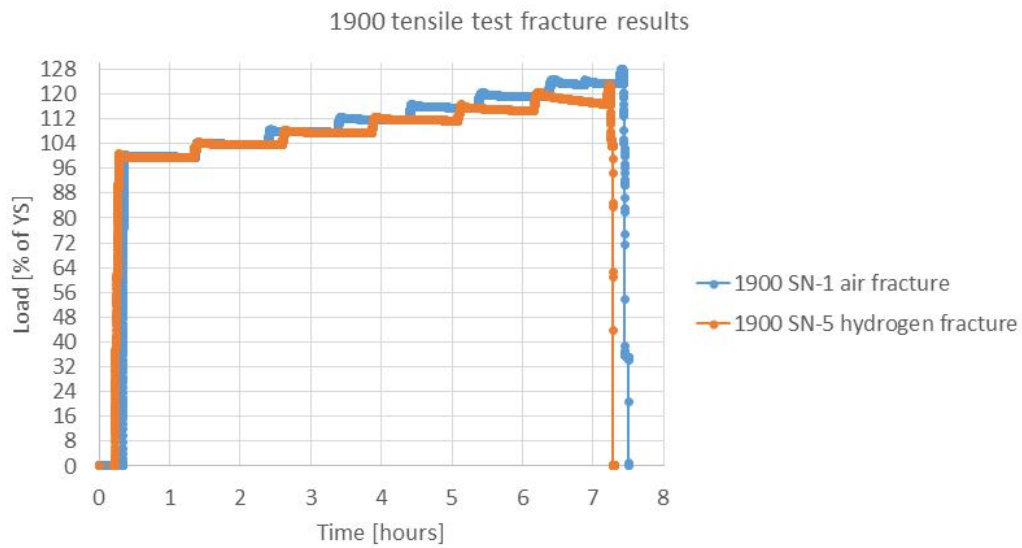


**Figure 4.9:** Tensile test results of the fracture tests of 1900 coarse grained material.

The plan was at first to perform reference tests of one fracture test in air and one in Glycerol for each material. However, because the fine grained material tested in air fractured earlier than expected, two reference tests in air were performed for this material. An unexpected fracture of sample 1850A SN-8 tested in Glycerol is the reason for also having two hydrogen fracture tests for the fine grained material.

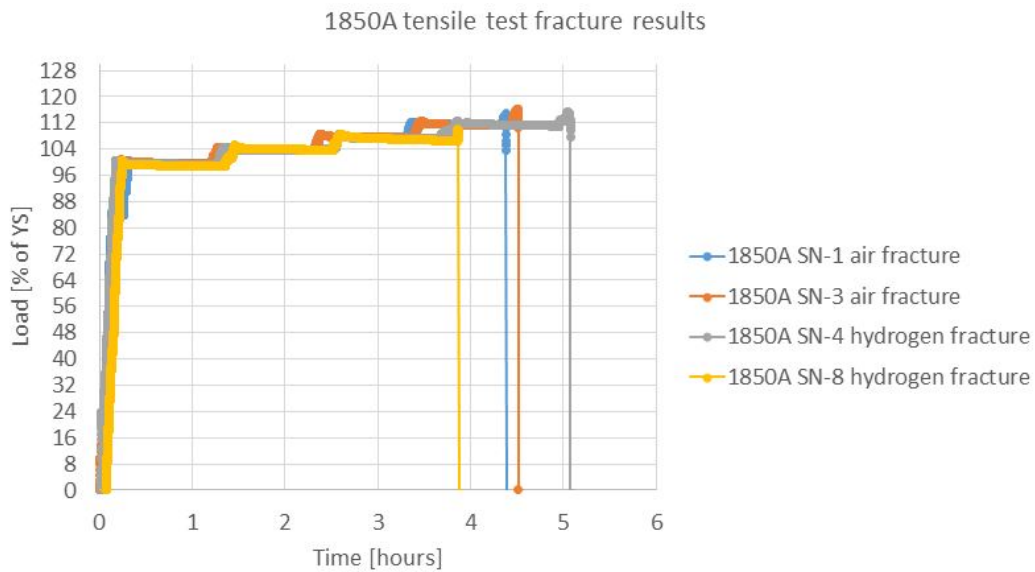


**Figure 4.10:** Tensile test results of the fracture tests of 1850A fine grained material.

The fracture strengths presented in Table 4.9 are given as average values. However, it is important to note that only one sample from each condition was tested for the coarse grained 1900 material. Thus, the values given are not average values, but rather single measurements. For the fine grained 1850A material, two samples were tested for each condition. It can be seen from Table 4.9 that the coarse grained 1900 material fractured at values above the ultimate tensile strength (UTS) provided by ATI Metals. The phenomenon of fracturing above the given UTS might be due to a strengthening effect from the geometry of the sample and the notch. The coarse grained material suffered a larger percentage drop in YS than the fine grained material.

**Table 4.9:** Tensile test fracture results summarized.

Type:	Grain size	Tested in	Avg. FS [% of YS]	Avg. FS [MPa]	Avg. FS [% of UTS]
1900	Coarse grained	air	128	1421	106
1900	Coarse grained	Glycerol	123	1366	102
1850A	Fine grained	air	115.5	1493	99.7
1850A	Fine grained	Glycerol	113	1458	97.3

Figure 4.11 displays an example of the recorded potential from a stepwise tensile loading experiment. The dips in the curve show the potential while the current was turned off during loading, in order to obtain images that were as clear as possible and without hydrogen bubbles on the surface. These low potential dips were, in other words, recorded while the electric circuit was not



closed. Therefore, the actual numeric values of the dips in potential may be neglected. The potential for this sample during polarization was measured to be relatively stable at  $-1070$  mV vs.  $\text{Hg}/\text{Hg}_2\text{SO}_4$  when the current density was held constant at  $-1$  mA/cm<sup>2</sup>.

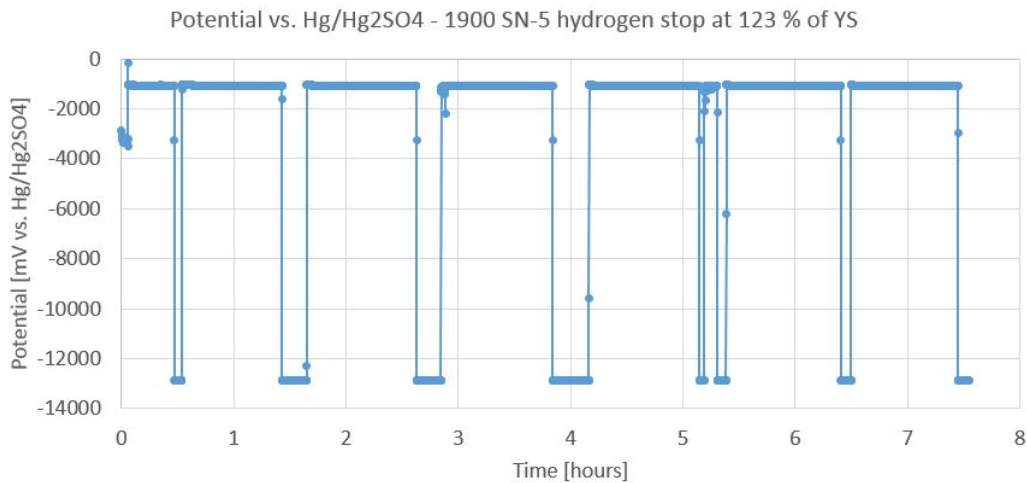


**Figure 4.11:** Potential-time curve for coarse grained sample 1900 SN-5 tested in Glycerol. The low points on the curve (around  $-13\ 000$  mV) show the potential when there was no cathodic current, as it was turned off while the load was gradually increased.

Potential-curves for all experiments performed with the Gamry<sup>TM</sup> potentiostat can be viewed in Figure 4.12. Most of the potential-curves were relatively stable between  $-1050$  and  $-1200$  mV vs.  $\text{Hg}/\text{Hg}_2\text{SO}_4$ . However, samples 1900 SN-7 and 1900 SN-8 stand out somewhat from the others. 1900 SN-7 was stable at about  $-1250$  mV vs.  $\text{Hg}/\text{Hg}_2\text{SO}_4$  and 1900 SN-8 was stable at about  $-1350$  mV vs.  $\text{Hg}/\text{Hg}_2\text{SO}_4$ . There is no obvious reason for the two samples to deviate from the others, but the difference might be due to the etching process, which varied in time from sample to sample. Also, a new batch of etching liquid was mixed toward the end of the project. Even though it was mixed according to the same specifications as the first batch, it required longer times to obtain the same level of etching. This new batch was used to etch the microstructure of samples 1900 SN-7 and SN-8 and might have affected the material surface enough to alter the potential slightly.

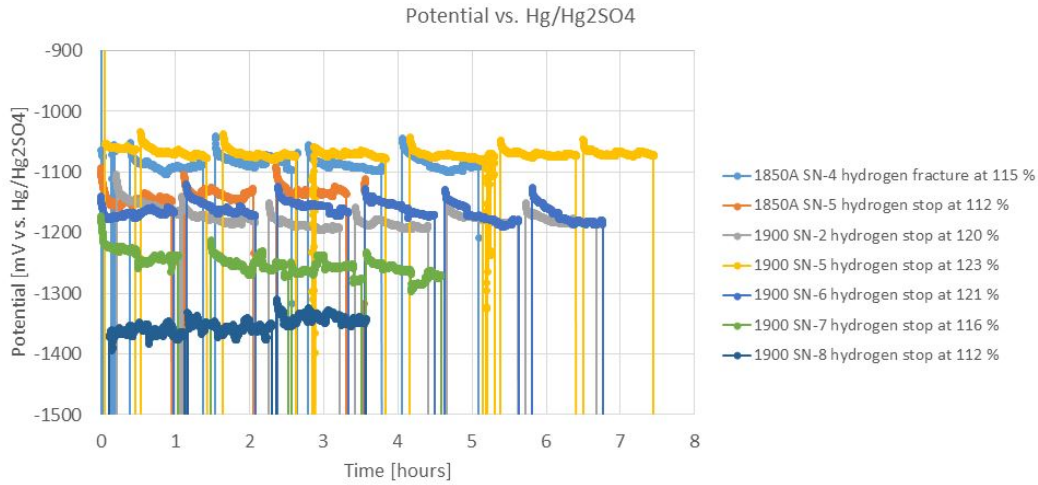


**Figure 4.12:** Potential-curves for the experiments.

Data supplied by Gamry Instruments [68] reports that an Ag/AgCl reference electrode has a potential of 0.198 V vs. Normal Hydrogen Electrode (NHE), while Hg/Hg<sub>2</sub>SO<sub>4</sub> has a potential of 0.654 V vs. NHE. This information has been used to make Table 4.10 (the values are valid at room temperature). The values given are for the lowest measured potential (1900 SN-8) and highest measured potential (1850A SN-5).

**Table 4.10:** Highest and lowest measured potential from the tensile tests. Including values converted to Ag/AgCl.

	mV vs. Hg/Hg <sub>2</sub> SO <sub>4</sub>	mV vs. Ag/AgCl
Most positive (1850A SN-5)	-1050	-594
Most negative (1900 SN-8)	-1370	-914

Three experiments utilized a different potentiostat than the others. The potentiostat in this case was an Elektroniklabor Schrems PGU-10V-1A-E. There were some problems with the plotting of potential-curves from the files generated by this potentiostat. Therefore, a table is given with the potential values from the beginning and end of these experiments. The values are presented in Table 4.11. For sample 1900 SN-3, a standard calomel electrode (SCE) was used, due to testing in 3.5 % NaCl synthetic seawater solution.

**Table 4.11:** Potential-results from the three experiments using the Elektroniklabor Schrems potentiostat.

Sample	Treatment	Electrolyte	Reference electrode	Initial potential [mV]	Final potential [mV]
1900 SN-3	Stop at 120 %	3.5 % NaCl	SCE	-1305	-1195
1850A SN-7	Stop at 108 %	Glycerol	Hg/Hg <sub>2</sub> SO <sub>4</sub>	-1265	-1283
1850A SN-8	Fracture at 111 %	Glycerol	Hg/Hg <sub>2</sub> SO <sub>4</sub>	-1128	-1128

According to Gamry Instruments [68] mV vs. SCE at room temperature can be converted to mV vs. Ag/AgCl by adding 43 mV to the SCE values. This results in an initial potential of -1258 mV vs. Ag/AgCl and a final potential of -1151 mV vs. Ag/AgCl for sample 1900 SN-3 tested in 3.5 % NaCl. In comparison with Table 4.10, it can be seen that 1900 SN-3 had a significantly lower potential than the other experiments. A similar potential for Inconel 718 tested in 3.5 % NaCl was found in project work performed by the author (-1320 (initial) and -1180 (final) mV vs. Ag/AgCl) [9].

### 4.3 SEM Images - Fracture Tests

The fracture surfaces of the specimens were examined in scanning electron microscope in order to characterize the fracture to be either ductile or brittle. The area of the fracture surface was also measured in the SEM, in order to later calculate the reduction of area and compare the samples tested in air and electrolyte.

All samples strained to fracture were imaged in the same manner in the scanning electron microscope. The entire fracture surface was examined for all samples. However, the key difference between the samples tested in air and those in Glycerol was found near the notch. Brittle fracture characteristics could be seen near the notch in the specimens tested with hydrogen. At the center of the fracture surface, all samples exhibited ductile fracture characteristics. Therefore, only images from the notch area and the center of the samples are presented here. Figure 4.13 shows where the images were taken when examining the fracture surfaces.

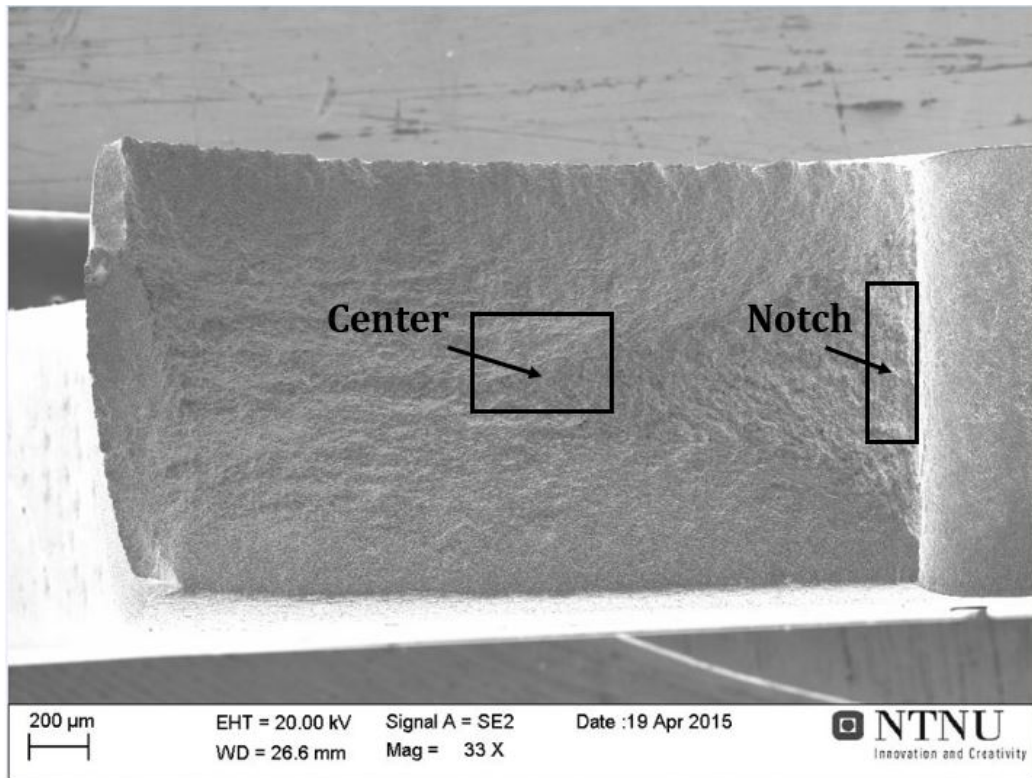


**Figure 4.13:** All fracture surfaces were examined in the same manner, capturing pictures from the notch area as well as the center. This is a map of the fracture surface of the fine grained 1850A SN-4 strained to fracture in Glycerol. 33X magnification.

### 4.3.1 Fine Grains - 1850A SN-1 Air Fracture

Figure 4.14 shows a SEM image from the notch area of the fine grained 1850A SN-1 strained until fracture in air. This sample exhibited ductile dimpled features across the entire fracture surface.

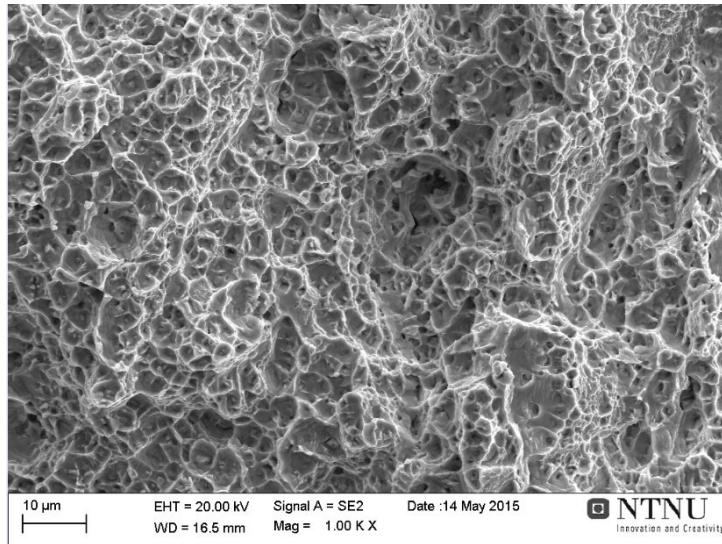


*Figure 4.14: Fine grained sample 1850A SN-1 exhibiting ductile fracture characteristics near the notch edge. 1000X magnification.*

### 4.3.2 Fine Grains - 1850A SN-4 Hydrogen Fracture

Figure 4.15 shows a SEM image from the notch area of the fine grained 1850A SN-4 strained until fracture in Glycerol. The fracture surface displays brittle transgranular cleavage features near the notch. Figure 4.16 shows the dimpled features from the center of the fracture surface of the same sample.

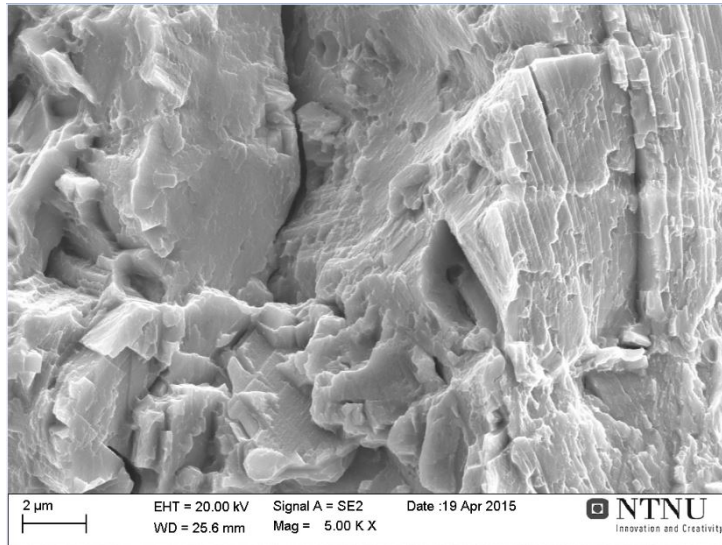


**Figure 4.15:** Fine grained sample 1850A SN-4 exhibiting brittle cleavage fracture characteristics near the notch edge. 5000X magnification.

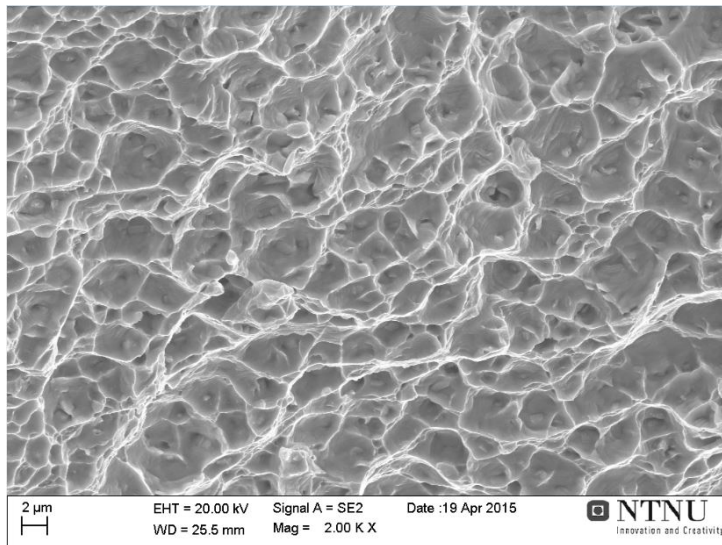


**Figure 4.16:** Fine grained sample 1850A SN-4 exhibiting ductile fracture characteristics near the center of the fracture surface. 2000X magnification.



### 4.3.3 Coarse Grains - 1900 SN-1 Air Fracture

Figure 4.17 shows a SEM image from the notch area of the coarse grained 1900 SN-1 strained until fracture in air. This sample exhibited ductile dimpled features across the entire fracture surface.

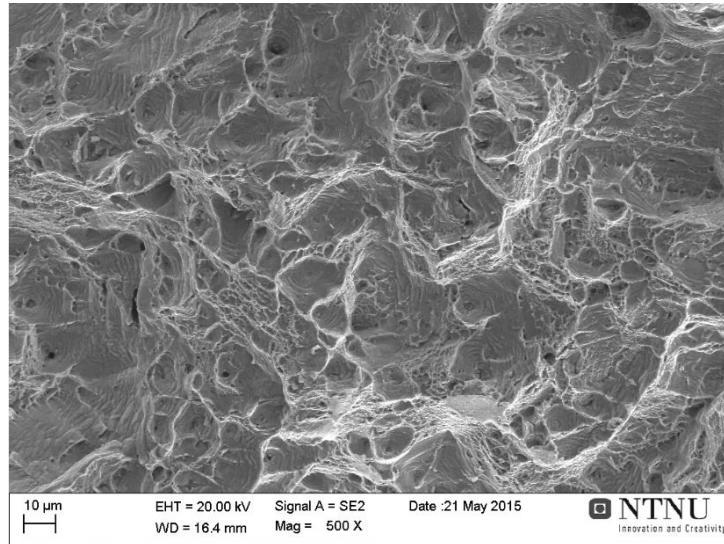


*Figure 4.17: Coarse grained sample 1900 SN-1 exhibiting ductile fracture characteristics near the notch edge. 500X magnification.*

### 4.3.4 Coarse Grains - 1900 SN-5 Hydrogen Fracture

Figure 4.18 shows a SEM image from the notch area of the coarse grained 1900 SN-5 strained until fracture in Glycerol. The fracture surface displays brittle transgranular cleavage features near the notch. Figure 4.19 shows the dimpled features from the center of the fracture surface of the same sample.

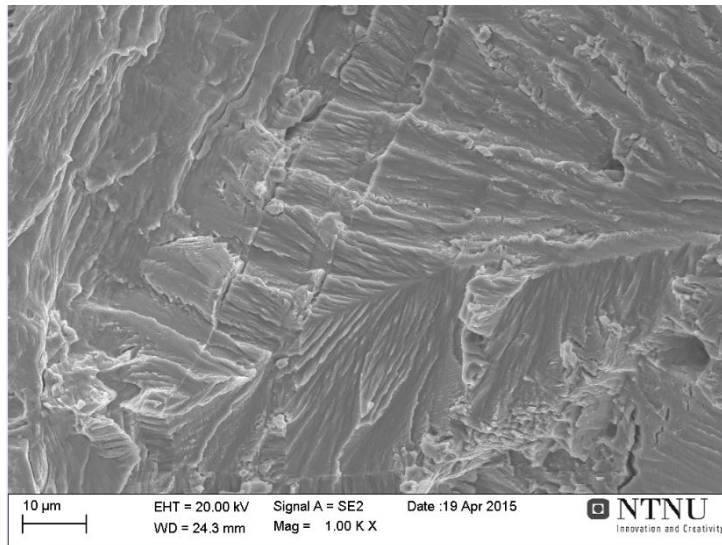


**Figure 4.18:** Coarse grained sample 1900 SN-5 exhibiting brittle cleavage fracture characteristics near the notch edge. 1000X magnification.

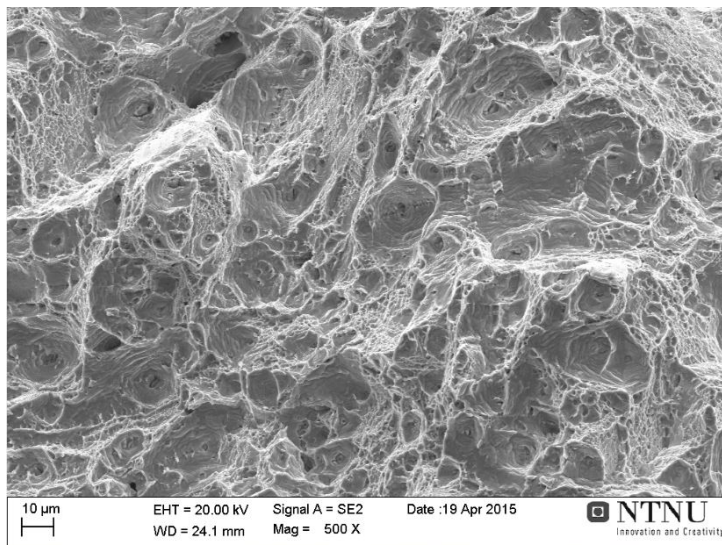


**Figure 4.19:** Coarse grained sample 1900 SN-5 exhibiting ductile fracture characteristics near the center of the fracture surface. 500X magnification.

From the fractographs in the above sections, it is clear that all samples subjected to hydrogen charging have been embrittled to some degree. The reference samples for both the fine grained and coarse grained samples exhibited ductile features only. All the other samples had been embrittled near the surface of the material. This is evidenced by the faceted features indicating



brittle transgranular fracture. Ductile features near the middle of the surface were found in all samples.

#### 4.4 Depth of Brittle Area

An effort was made to quantify the degree of embrittlement by measuring the depth of the brittle area. The depth was taken as the length from the edge where the fracture initiated to the area where ductile features became dominating. In all samples, the fracture initiated at the edge of the fracture surface corresponding to the notch. In other words, the depth of the brittle area was taken as the length from the notch edge to the area of where the fracture became ductile (measured by a line straight inward from the edge). Table 4.12 summarizes the measured extent of the brittle areas.

**Table 4.12:** Depth of the brittle area of the fracture surfaces observed in the SEM.

Sample	Test type	Depth of brittle area [ $\mu\text{m}$ ]
1900 SN-1	air	0
1900 SN-5	in situ charging in Glycerol	240.4
1850A SN-1	air	0
1850A SN-3	air	0
1850A SN-4	in situ charging in Glycerol	79.6
1850A SN-8	in situ charging in Glycerol	101.1

It is evident from the results in Table 4.12 that none of the samples tested in air exhibited any brittle fracture characteristics. All samples tested with in situ polarization showed some embrittlement near the notch edge. The coarse grained 1900 material had a larger brittle area than the fine grained 1850A.

#### 4.5 Measurements of Reduction of Area

In order to obtain a measure of the ductility of the samples, reduction of area (RA) was calculated after fracture. This was done by measuring the cross sectional area before and after tensile testing. Before testing, the cross section area of the notched part of the specimen was measured: the height of the notch area was measured using an optical microscope; the width was measured using a caliper at three different places on the gauge, using the average value in calculations. After fracture, the cross section area was measured by imaging the fracture surface directly from above in the SEM, then

using the SEM software to measure the length of the sides, as shown in Figure 4.20. All sides were measured and the area was calculated by assuming the fracture surface could be approximated by a rectangle. This assumption is not completely correct; however, it proved difficult to find a more accurate measure.

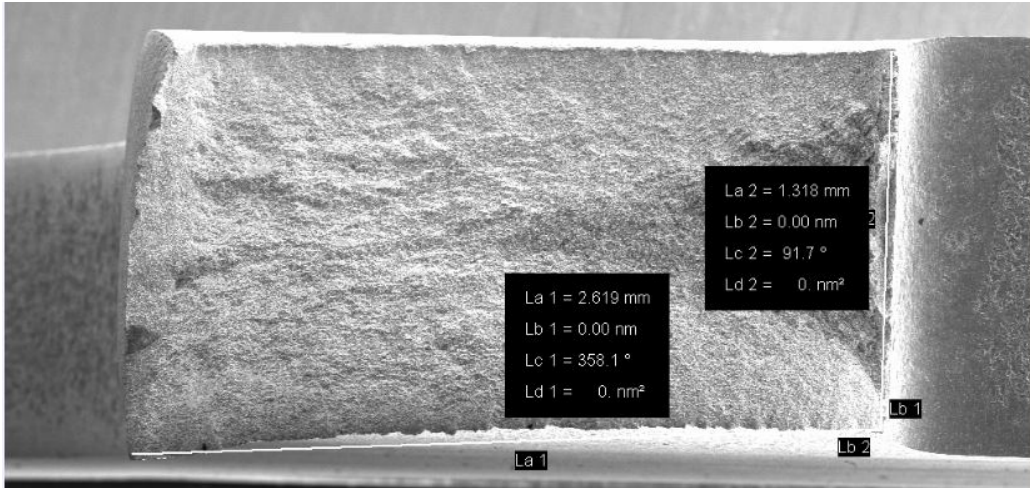


**Figure 4.20:** After fracture, the cross section area was measured by imaging the fracture surface directly from above in the SEM, then using the SEM software to measure the length of the sides.

**Table 4.13:** Results from measurements of reduction of area

Sample	Test type	% RA
1900 SN-1	air	25.2
1900 SN-5	in situ charging in Glycerol	26.4
1850A SN-1	air	20.1
1850A SN-3	air	23.9
1850A SN-4	in situ charging in Glycerol	6.4
1850A SN-8	in situ charging in Glycerol	16.8

From the results presented in Table 4.13, it can be seen that the coarse grained 1900 samples experienced no reduction in RA (i.e. no reduction of ductility), while the fine grained 1850A samples experienced a marked decrease in reduction of area. These results are opposite from the ones obtained in previous project work by the author [9], in which the 1900 material exhibited a reduction in ductility, while the fine grained 1850B material exhibited no reduction. This suggests that the RA results should be interpreted with

care, as only a few samples were tested and the results are vulnerable to inaccuracies in the measuring method as well as scatter.

#### 4.6 SEM Images - Stop Tests

The specimens which had been tested and stopped before fracture were also examined in scanning electron microscope. This time the objective was to examine how cathodic charging, i.e. hydrogen, would affect crack initiation and propagation. The polished and etched sides of the specimens were exhaustively examined in the SEM; thousands of images were obtained in total. However, only a few images from each sample could be included in this thesis. Consequently, the images presented here are included to exemplify what has been found in the investigation of each specimen. Comments on the tendencies found in each sample will follow for all samples, with a summary at the end of this section. Samples tested and stopped in air are referred to as "air stop". Samples tested and stopped with in situ cathodic polarization are referred to as "hydrogen stop".

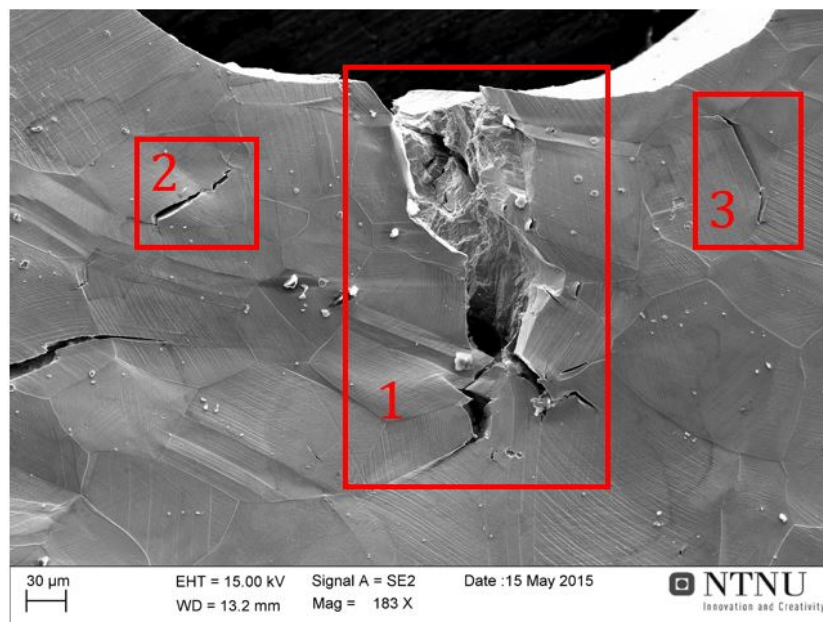


**Figure 4.21:** This picture illustrates the difference between a main crack and secondary cracks. The main crack is marked number 1; a crack propagating from the notch root, clearly on its way to failure. The cracks marked by numbers 2 and 3 are examples of secondary cracks; cracks initiating in the microstructure around the main crack. 183X magnification.

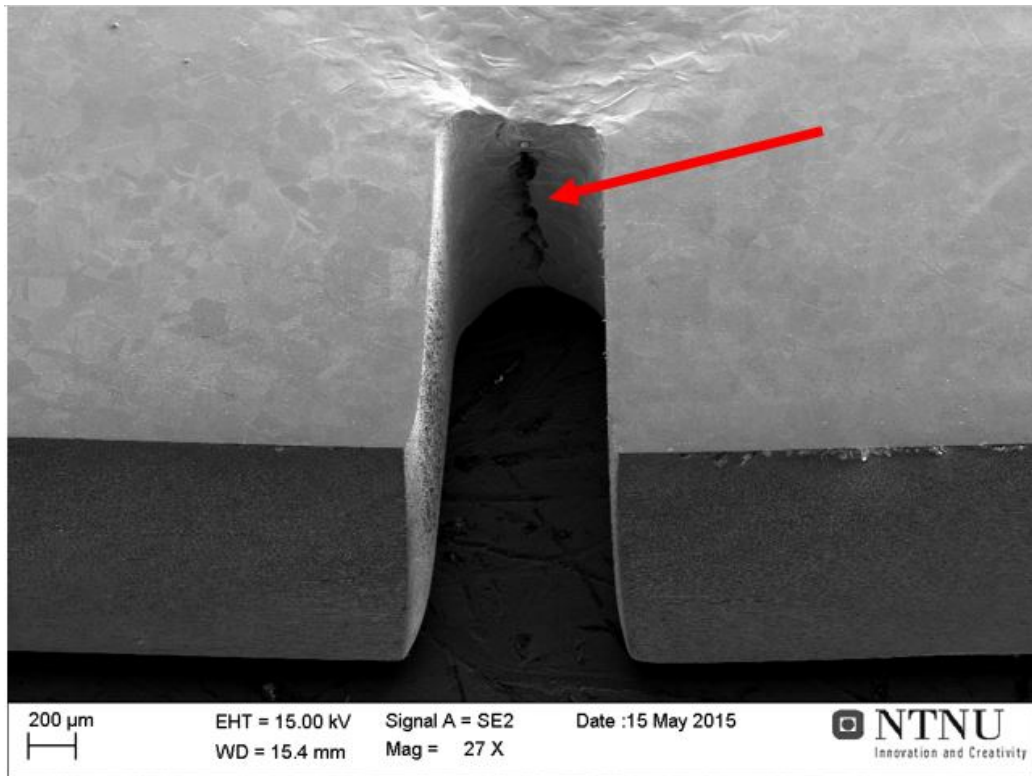


**Figure 4.22:** An example of a main crack propagating from the notch root. All samples exhibited main cracks that propagated from inside the notch. However, they had not always reached the sides of the sample when the experiment was stopped. 27X magnification.

Figures 4.21 and 4.22 illustrates the different types of cracks observed in the stop tests. It was useful to distinguish between main cracks (large cracks propagating from the notch root) and secondary cracks (which had initiated in the microstructure adjacent to the main crack, at the sides of the sample). Figure 4.22 shows where all the main cracks initiated. Large cracks propagating from the rough inside of the notch root were observed for all samples. The results from the fracture tests (section 4.3) provide information the appearance of the inside of these cracks.

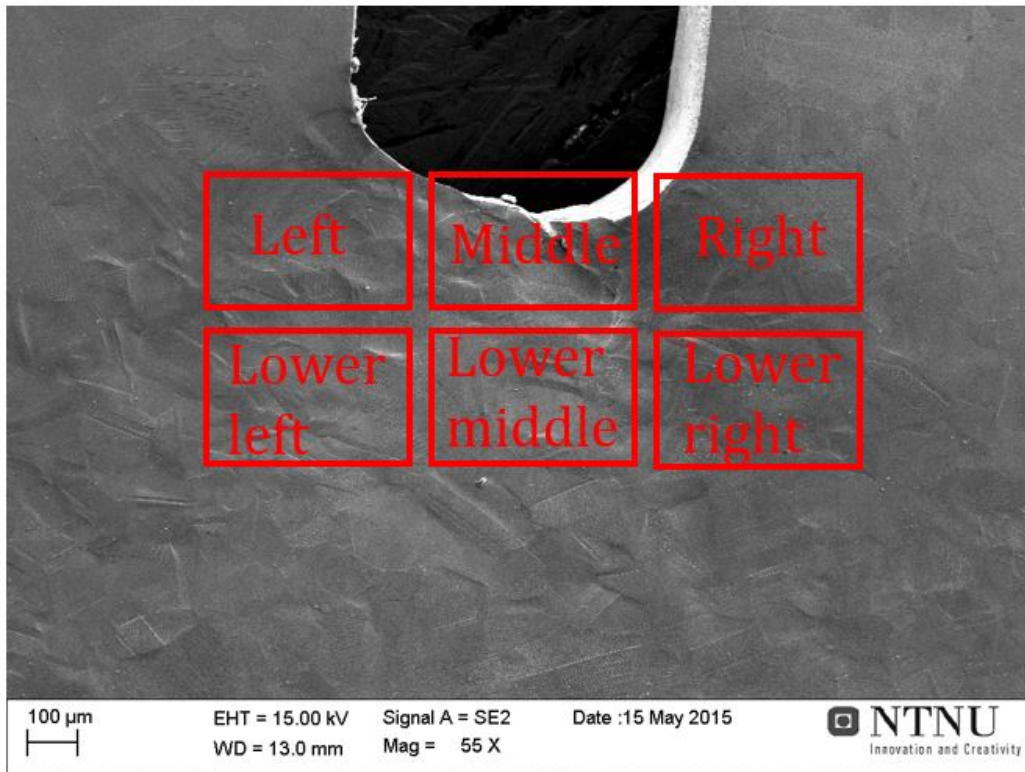


*Figure 4.23: A map of the areas imaged in the SEM. 55X magnification.*

For some pictures there will be a need to describe where on the specimen surface the picture is from. This will be referenced by using the designations presented in Figure 4.23. This information will be given in the figure captions.



#### 4.6.1 Coarse Grained Material: P3A01-1900 SN-1 Air Stop at 128 % of YS

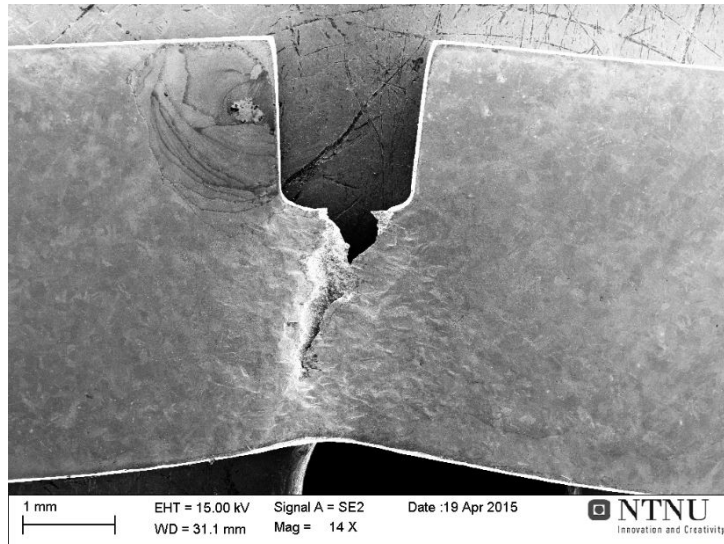


*Figure 4.24: Coarse grained sample 1900 SN-1 strained until a large crack appeared. Except from the main crack, no cracking could be seen on the surface of the sample. 14X magnification.*

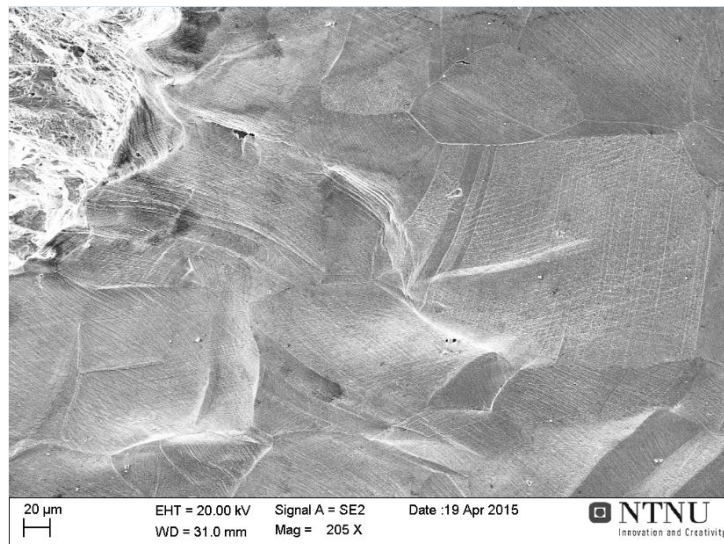


*Figure 4.25: A closer look at the microstructure next to the main crack, revealing no visible secondary cracking in this sample tested in air. Part of the fracture surface can be seen in the upper left corner of the picture. 205X magnification.*

The 1900 SN-1 sample was actually intended to be strained to fracture in air, which it essentially was, as the load could not be increased any further without tearing the sample in two. The sample was taken out of the tensile apparatus and imaged in SEM before it was reinserted and strained to fracture at a later time. This allowed examination of the surface of a sample that had been strained to the maximum load it could tolerate. A large crack, almost leading to complete fracture can be seen in Figure 4.24. This is referred to as the main crack. In Figure 4.25, the microstructure next to the crack exhibits no secondary cracking, even though the sample has essentially been strained to fracture.

#### 4.6.2 Coarse Grained Material: P3A01-1900 SN-4 Air Stop at 121 and 127 % of YS

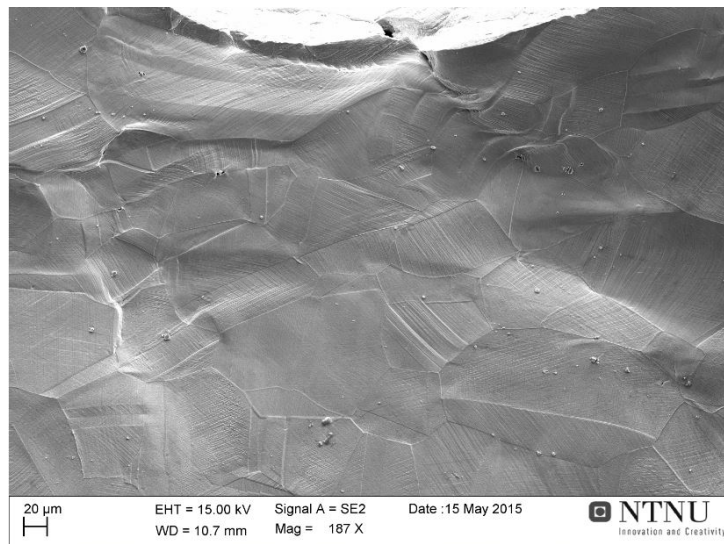


**Figure 4.26:** Coarse grained sample 1900 SN-4 re-loaded to 127 % of YS in air. Other than the main crack, no cracking could be seen on the surface of the sample. 187X magnification.

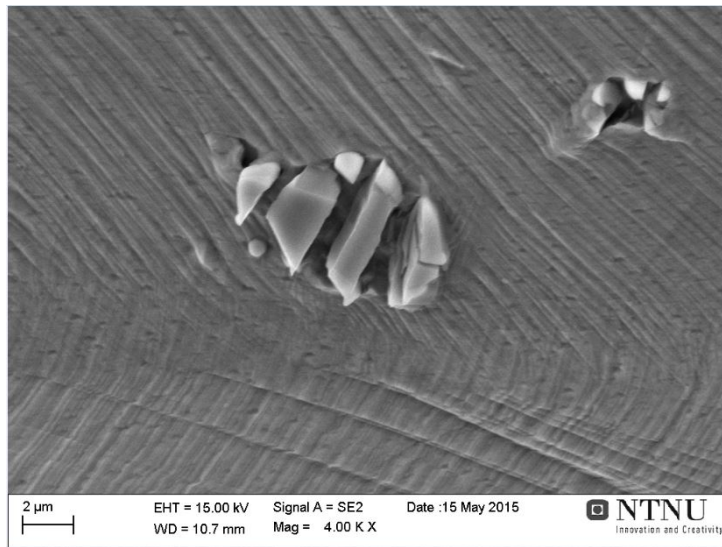


**Figure 4.27:** Some cracked particles could be observed in sample 1900 SN-4 re-loaded to 127 % of YS in air. 4000X magnification.

Sample 1900 SN-4 was first tested in air and stopped at 121 % of yield strength. It then exhibited no visible cracking when imaged in the SEM. The sample was subsequently re-loaded to 127 % of YS. By then, one main crack had initiated on the notch root, and propagated so that it just reached the side of the sample. This can be observed in the top of Figure 4.26. No secondary cracking could be observed, although several cracked particles were found. This is illustrated by Figure 4.27. Nonetheless, no cracks appeared to be propagating from the cracked particles.



#### 4.6.3 Coarse Grained Material: P3A01-1900 SN-2 Hydrogen Stop at 120 % of YS

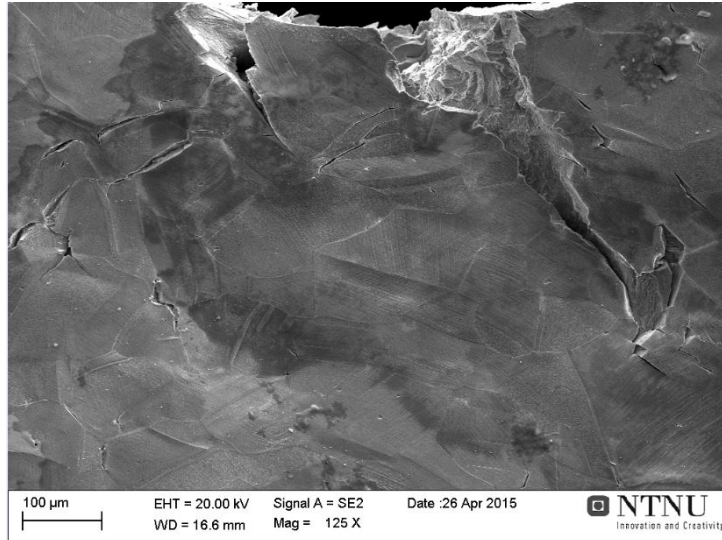


*Figure 4.28: Two large main cracks were found on this side of the sample. Several secondary cracks can also be seen in the picture of coarse grained sample 1900 SN-2, which was stopped at 120 % of YS. 125X magnification.*

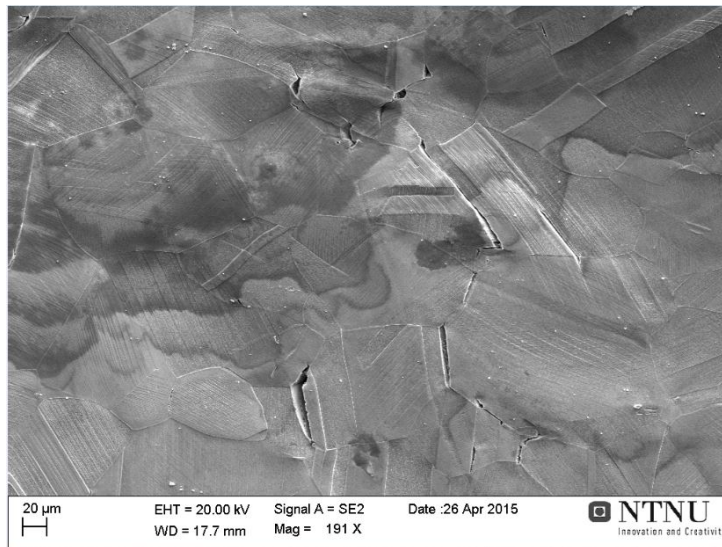


**Figure 4.29:** Picture showing several secondary cracks initiated at twins and grain boundaries in coarse grained sample 1900 SN-2, which was stopped at 120 % of YS. The picture is taken from the lower left area under the notch. 191X magnification.

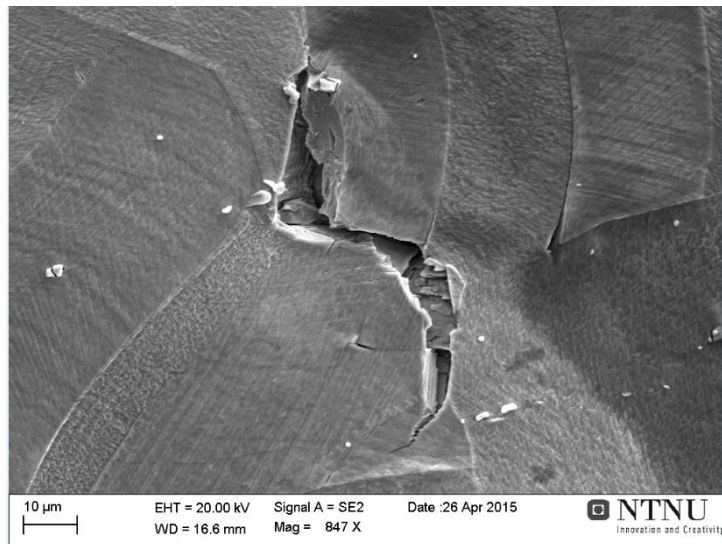


**Figure 4.30:** Close-up of a crack initiated at a twin boundary in coarse grained sample 1900 SN-2, which was stopped at 120 % of YS. The picture is taken from the lower middle area under the notch. 847X magnification.

Several large cracks were found propagating from the notch, as seen in Figure 4.28. One of these seemed to be the main crack, which had propagated the

furthest. A substantial number of secondary cracks had initiated in the area adjacent to the main crack. Figure 4.29 shows an image of the microstructure from the lower left area under the notch, where several secondary cracks have initiated at grain boundary corners and twins. A close-up of initiation at a twin is provided in Figure 4.30. Cracks mainly seem to initiate at grain boundary corners and twin boundaries. However, cracks that had propagated transgranularly could be found in the microstructure. Secondary cracks had formed at 45 °angles to the notch root, but also in the area directly below the notch. It is a possibility that initiation happens at grain boundary corners and twin boundaries, but propagation happens transgranularly. This is suggested by the fact that most small cracks could be seen initiating at GBs and twins, while most larger cracks passed through several grains.

#### 4.6.4 Coarse Grained Material: P3A01-1900 SN-3 Hydrogen Stop at 120 % of YS

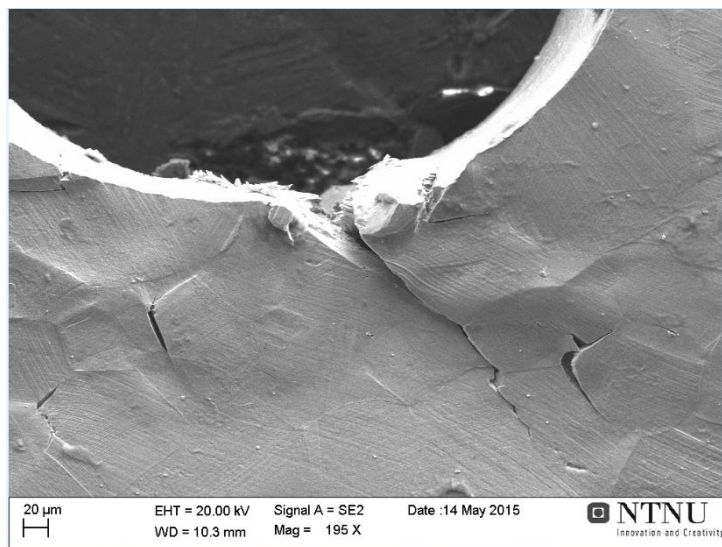


**Figure 4.31:** Picture showing several secondary cracks initiated adjacent to the main crack in coarse grained sample 1900 SN-3, which was stopped at 120 % of YS and polarized in 3.5 % NaCl. 195X magnification.

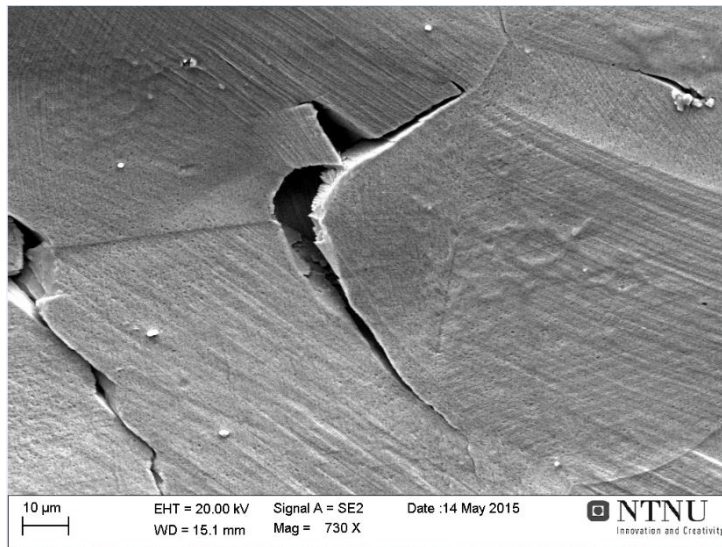


**Figure 4.32:** Close-up of a crack initiated at a grain boundary in coarse grained sample 1900 SN-3, which was stopped at 120 % of YS and polarized in 3.5 % NaCl. The picture is taken from the lower right area under the notch. 730X magnification.

Sample 1900 SN-3 was tested in a 3.5 % NaCl solution, with the additional purpose to explore whether or not the image quality of the optical image series could be increased. The main crack could be seen propagating from the notch, surrounded by secondary cracks, as shown in Figure 4.31. Secondary cracks appear to have initiated preferentially at grain boundary corners and twin boundaries. Figure 4.32 displays a crack that seems to have initiated at the corner of grain boundaries. Several cracked particles were present, but not many larger cracks seem to have propagated from these. Some examples of transgranular propagation could be seen as well. Most of the secondary cracking happened at 45° angles from the notch (max stress).

A residue was discovered on the surface, which could possibly be corrosion products. This residue was not found in other experiments. The potential was measured to lie between -1258 and -1151 mV vs. Ag/AgCl, which should be enough to prevent corrosion. However, it is believed that the residue may have appeared during the load increases, when the current was turned off. This is suggested by the fact that experiments from previous work [9] displayed no corrosion under comparable potentials with no stops in the current.



#### 4.6.5 Coarse Grained Material: P3A01-1900 SN-6 Hydrogen Stop at 122 % of YS

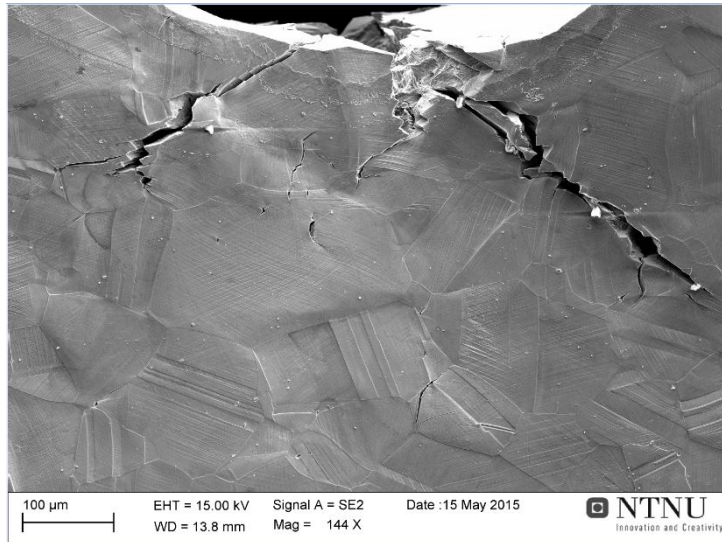


*Figure 4.33:* Picture showing several secondary cracks initiated adjacent to the main crack in coarse grained sample 1900 SN-6, which was stopped at 122 % of YS. 144X magnification.

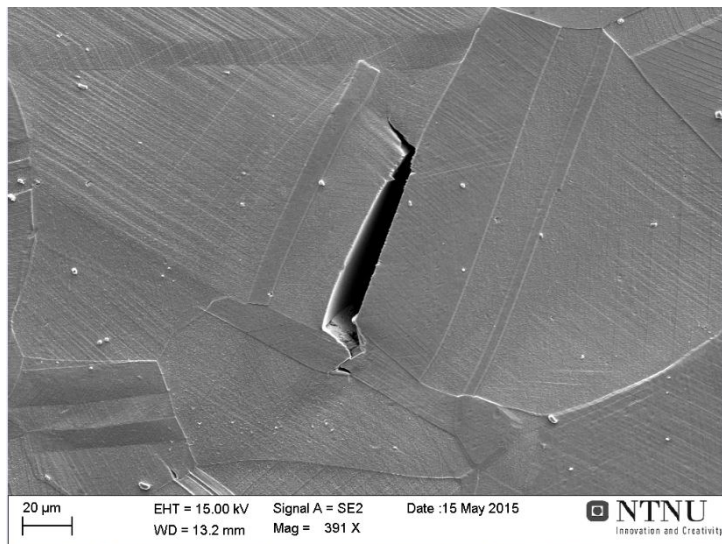


*Figure 4.34:* Picture showing a secondary crack initiated at a twin boundary in coarse grained sample 1900 SN-6, which was stopped at 122 % of YS. 391X magnification.

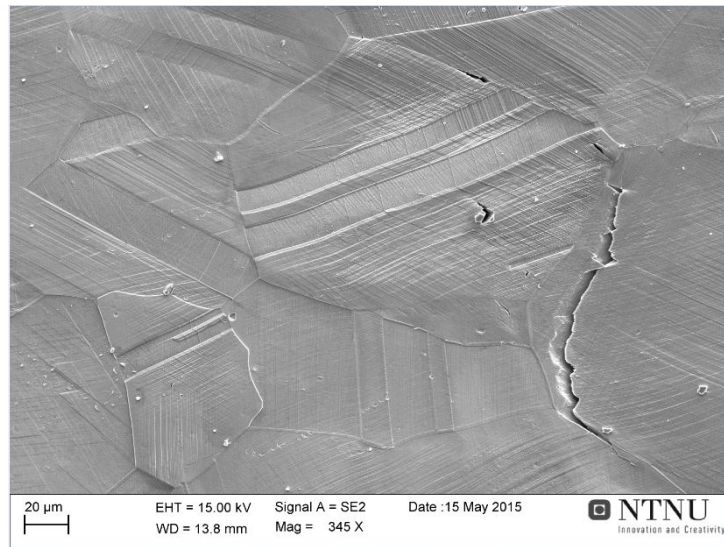


**Figure 4.35:** Close-up of a crack that seemed to have initiated at a grain boundary corner, and propagated inside the grain, in coarse grained sample 1900 SN-6. The picture is taken from the lower right area under the notch. 345X magnification.

The two main cracks in sample 1900 SN-6 have propagated at  $45^\circ$  angles to the notch root, as shown in Figure 4.33. Many secondary cracks were found in the middle of the sample, directly under the notch area. Several secondary cracks had initiated along grain and twin boundaries, as illustrated by Figures 4.34 and 4.35. However, cracks are also seen to pass through grains. The two main cracks seem to have propagated along the already initiated cracks present along the  $45^\circ$  max stress lines.

#### 4.6.6 Coarse Grained Material: P3A01-1900 SN-7 Hydrogen Stop at 116 % of YS

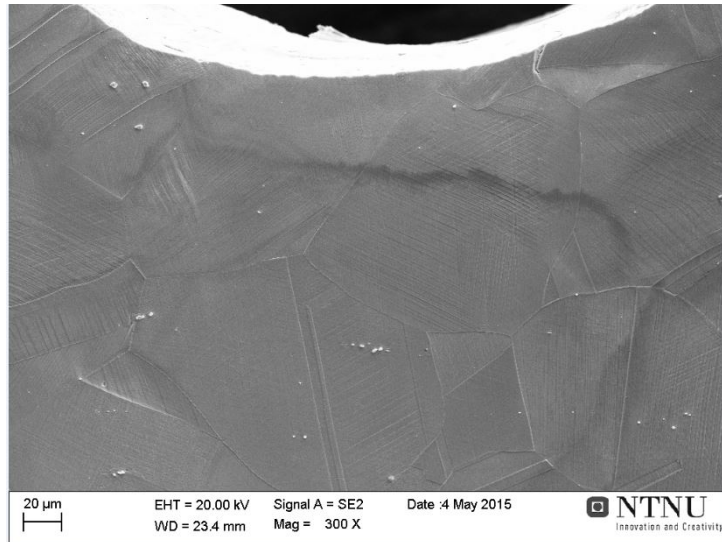


*Figure 4.36: No significant cracking is visible in coarse grained sample 1900 SN-7, which was stopped at 116 % of YS. 300X magnification.*

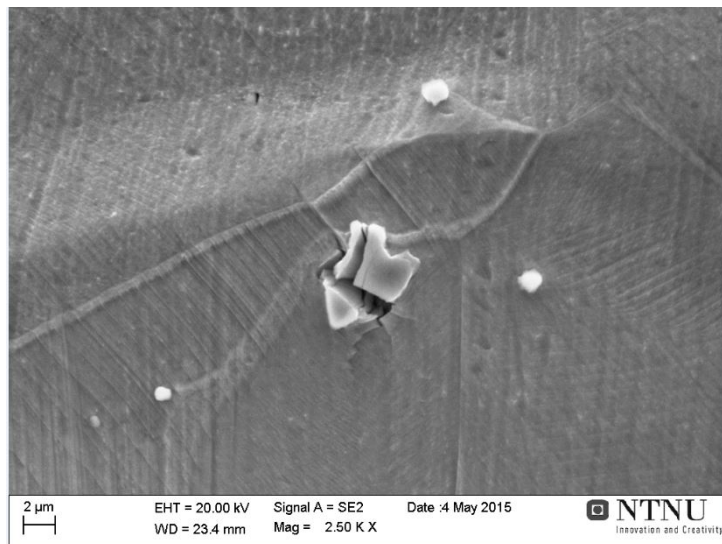


*Figure 4.37: Close-up of a cracked particle in coarse grained sample 1900 SN-7, which was stopped at 116 % of YS. 2500X magnification.*

Very little secondary cracking was found in sample 1900 SN-7, as displayed in Figure 4.36. A few very small cracks could be found that had initiated

at cracked particles, which can be seen in Figure 4.37. The particle has the same appearance as the large Ti-rich particles found in several other samples. Still, cracks in cracked particles had not propagated any further. One small crack was found, initiated at grain boundary. The main crack had begun propagating inside the rough notch area.

#### 4.6.7 Coarse Grained Material: P3A01-1900 SN-8 Hydrogen Stop at 112 % of YS

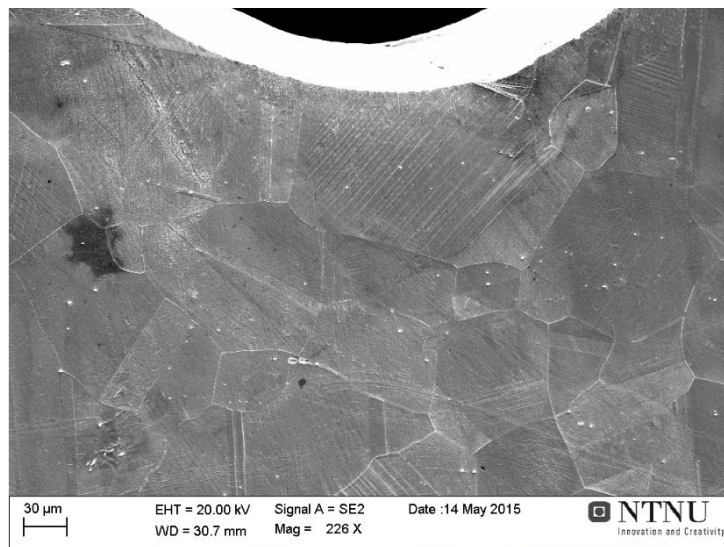


**Figure 4.38:** No cracking is visible in coarse grained sample 1900 SN-8, which was stopped at 112 % of YS. 226X magnification.



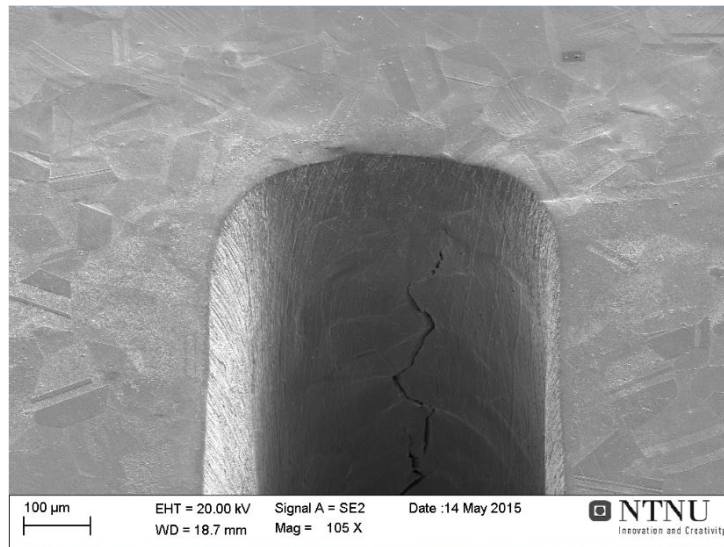


**Figure 4.39:** A picture showing the inside of the notch area of coarse grained sample 1900 SN-8, which was stopped at 112 % of YS. 105X magnification.

Essentially no secondary cracking was detected in sample 1900 SN-8 (Figure 4.38), loaded to 112 % of yield strength. One small secondary crack was found initiated at a grain boundary, but it had not propagated further. One cracked particle, exhibiting high Ti-levels when examined by EDS, was found (the particle is displayed in Figure 4.6, from section 4.1.2). Figure 4.39 displays how the main crack had initiated inside the notch root, but not yet propagated to reach the sides of the sample. As previously mentioned, the main cracks initiated in this area for all samples, due to the rougher surface inside the notch.

#### 4.6.8 Summary of Findings from Stop Tests of Coarse Grained Material

The samples tested in air exhibited no secondary cracking, even at loads that led to fracture. Several cracked particles were found, but no cracks had propagated from these. The cracked particles were most often coarse Ti- and N-rich particles, believed to be TiN-particles. However, cracked NbC-particles were also observed.

For the samples tested with in situ hydrogen charging, the first signs of secondary cracking appear at load levels in the region of 116 % of yield strength. The very first cracks initiate at grain boundaries. Cracked particles also appear at the same time. Despite this, no cracks that had clearly propagated

from cracked particles could be observed. These cracks seem to stop once they hit the matrix. At loads of 120 % of YS and up, numerous secondary cracks could be observed. Most cracks were found to initiate at the corners of grain boundaries and at twins. However, once cracks reach a threshold size, they continue to propagate transgranularly. Most of the secondary cracks were found along lines at approximately 45° angles to the notch root; this corresponds to the regions of highest deformation. Still, as large cracks propagated from the rough area inside the notch, several secondary cracks would develop in the middle area directly underneath the notch root.

#### 4.6.9 Fine Grained Material: P3A01-1850A SN-6 Air Stop at 115 % of YS

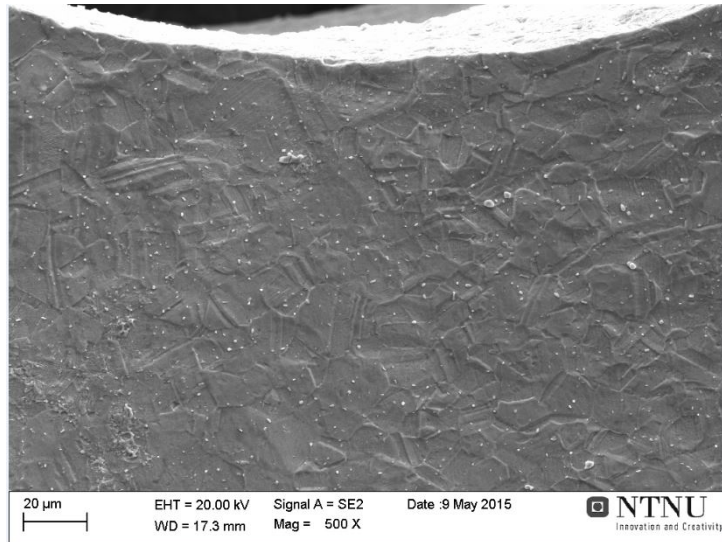


**Figure 4.40:** No secondary cracking was observed in the fine grained sample 1850A SN-6 that was stopped at 115 % of YS in air. 500X magnification.

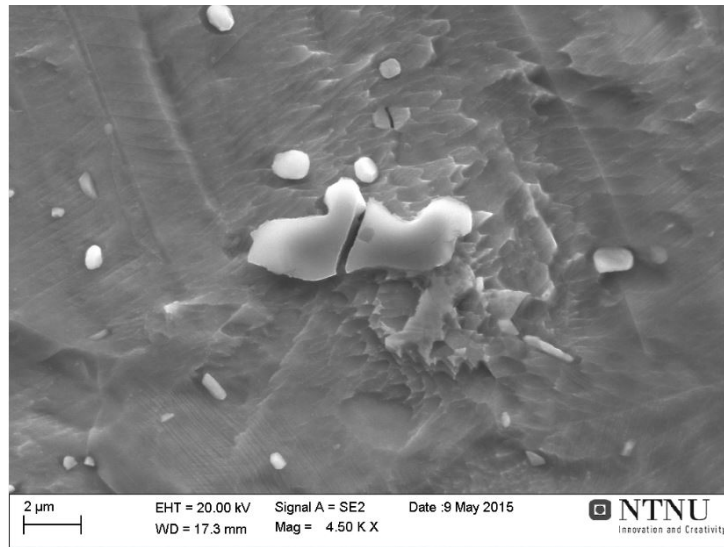


**Figure 4.41:** Image of a cracked particle in the fine grained sample 1850A SN-6 that was stopped at 115 % of YS in air. This particle was examined by EDS, where elevated Ti- and N-content was found. 4500X magnification.

No secondary cracking could be found in 1850A SN-6 loaded to 115 % of YS in air, as indicated by Figure 4.40. The only sign of crack initiation was at cracked particles, as in Figure 4.41. There were several of these. EDS was performed on large particles, small particles and the matrix. One of the large particles contained Ti and N and could be a TiN-particle (Figure 4.41). The smaller particles appear to be  $\delta$ , as they exhibited high niobium contents (contents suggested a relationship of approximately three times as high Ni as Nb, indicative of  $\delta$ ). It was later attempted to reload the sample after examination in SEM, in order to propagate a crack, but the sample failed immediately after re-application of load.

#### 4.6.10 Fine Grained Material: P3A01-1850A SN-2 Hydrogen Stop at 113 % of YS

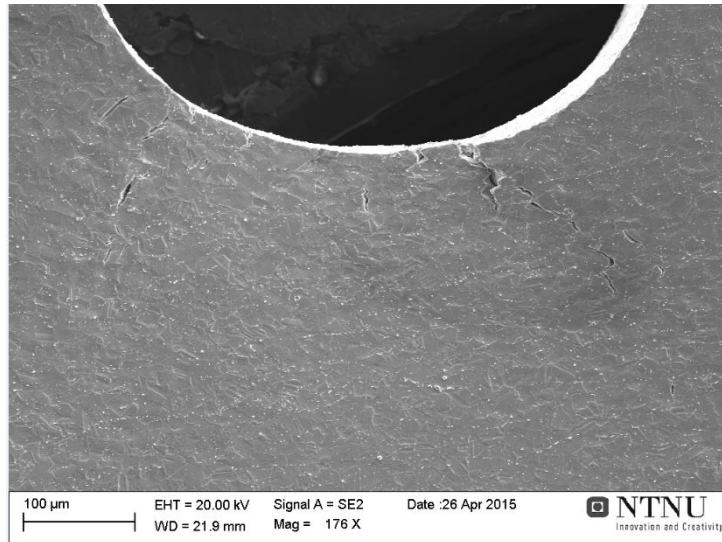


*Figure 4.42: Secondary cracks, especially evident at 45 degree angles to the notch root, were observed in the fine grained sample 1850A SN-2 that was stopped at 113 % of YS in Glycerol. 176X magnification.*

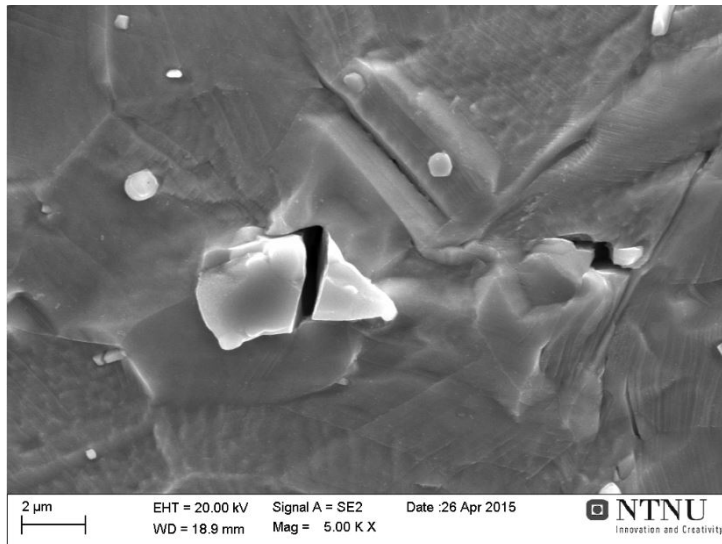


*Figure 4.43: Image of a cracked particle in the fine grained sample 1850A SN-2 that was stopped at 113 % of YS in Glycerol. 5000X magnification.*

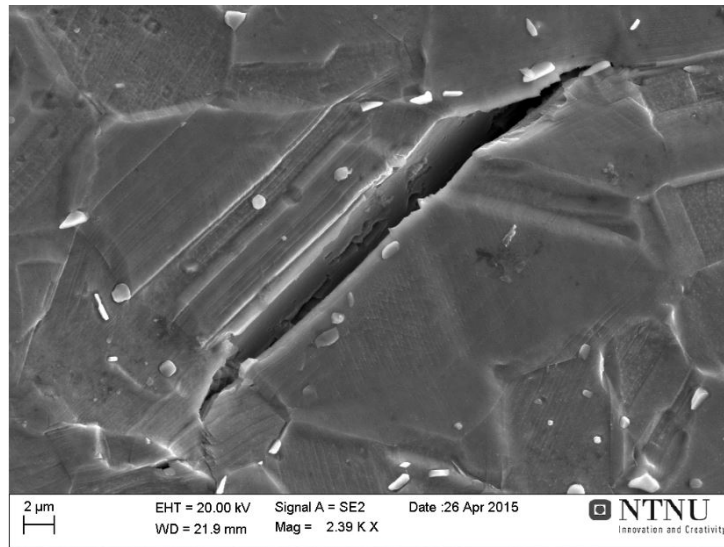


**Figure 4.44:** Cracking at a twin boundary in the fine grained sample 1850A SN-2 that was stopped at 113 % of YS in Glycerol. 55X magnification. 2390X magnification.

Significant amounts of secondary cracking could be detected in 1850A SN-2, loaded to 113 % of YS in Glycerol. Secondary cracks were particularly frequent at 45° angles from the notch, which correspond to the areas of maximum stress. This is shown in Figure 4.42. Secondary cracking could also be seen in the middle of the sample. Images displaying initiation at particles and twins are presented in Figures 4.43 and 4.44. However, it is difficult to determine if this is a clear tendency in the fine grained material. The particle in Figure 4.43 exhibited elevated levels of Ti-content in EDAX EDS analysis, which means that it is probably a large TiN-particle. Very few cracks that actually seem to propagate from the cracked particles were found.



#### 4.6.11 Fine Grained Material: P3A01-1850A SN-5 Hydrogen Stop at 112 % of YS

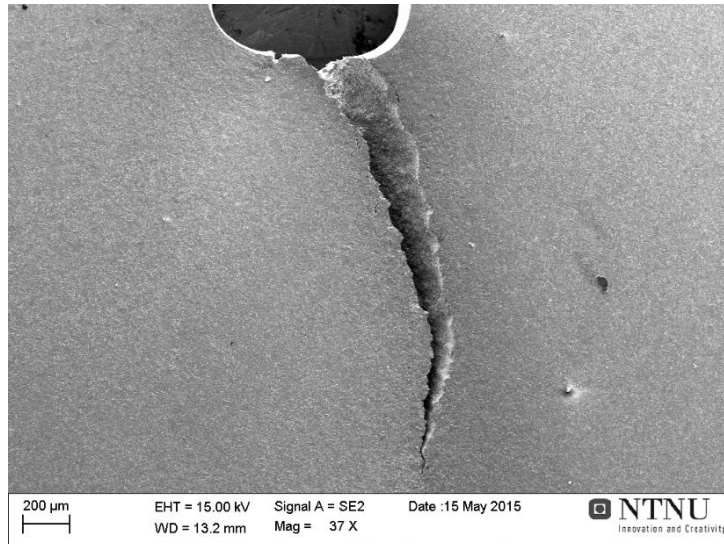


*Figure 4.45:* A large main crack was observed in the fine grained sample 1850A SN-5 that was stopped at 112 % of YS in Glycerol. 37X magnification.

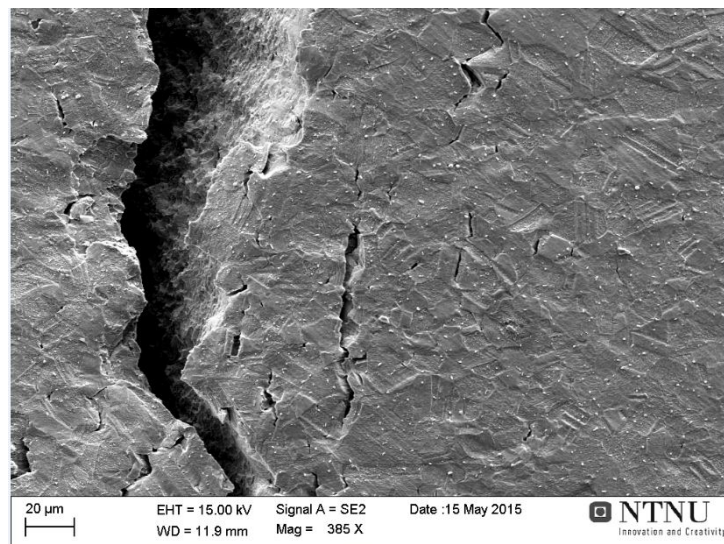


*Figure 4.46:* Secondary cracking was observed in the area adjacent to the main crack in the fine grained sample 1850A SN-5 that was stopped at 112 % of YS in Glycerol. 385X magnification.

In sample 1850A SN-5, loaded to 112 % of YS in Glycerol, one large main crack had propagated at an angle to the notch root (Figure 4.45). Significant amounts of secondary cracks were found in the vicinity of the crack, as displayed in Figure 4.46. Significant secondary cracking was also found opposite the main crack at a 45° angle to the notch root. Some cracking along grain boundaries and twins could be observed, although it is difficult to tell whether or not it is preferential to initiation inside grains. Particles do not appear to noticeably affect crack initiation and propagation.

#### 4.6.12 Fine Grained Material: P3A01-1850A SN-7 Hydrogen Stop at 108 % of YS

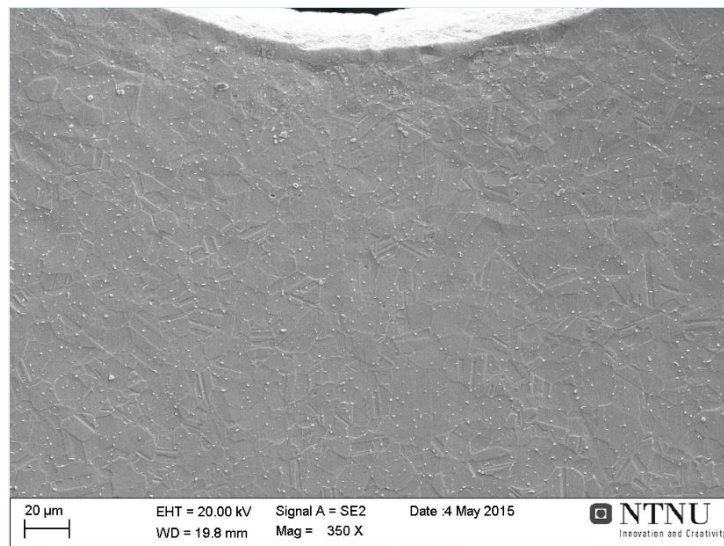


**Figure 4.47:** No surface cracking was found in the fine grained sample 1850A SN-7 that was stopped at 108 % of YS in Glycerol. 350X magnification.

No secondary cracking could be observed in sample 1850A SN-7, loaded to 108 % of YS in Glycerol. This is illustrated by Figure 4.47. One cracked particle was observed, with a similar appearance to the TiN-particle from 1850A SN-6 in section 4.6.9.

#### 4.6.13 Summary of Findings from Stop Tests of Fine Grained Material

No secondary cracks were detected in the sample that was loaded to 115 % of YS and stopped in air. Coarse particles that exhibited elevated Ti- and N-content had cracked, but no propagation into the matrix could be seen.

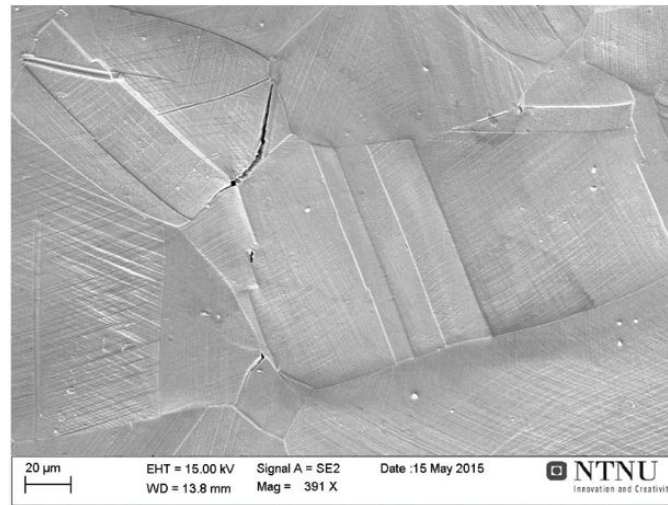
For the fine grained samples tested with in situ hydrogen charging, no secondary cracks were detected for the stop test at 108 % of YS. At higher loads, however, the specimens exhibited significant amounts of secondary cracking. The density of cracks was highest along lines at approximately 45° angles to the notch root. Initiation of cracks was found at grain boundaries and twins. However, due to the small grain size, it was difficult to determine if this was a clear tendency. That is to say that indications of preferential initiation at grain boundaries and twins are present, but there is need for further supporting evidence. Particles did not appear to affect crack initiation or propagation.

#### 4.7 EBSD

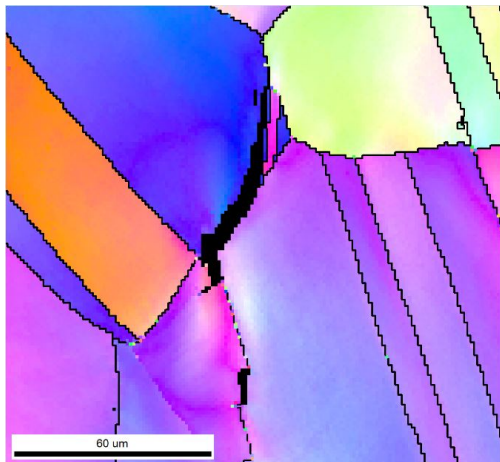
EBSD was utilized to examine selected areas of certain samples, in order to establish further proof of crack initiations sites and deformation patterns. The images from EBSD provide clear maps of the grains and grain boundaries, making it possible to draw conclusions on whether or not a crack initiated and propagated along a boundary.

Two samples were chosen for EBSD analysis, one of each grain size. These were samples 1900 SN-6, tested in Glycerol and stopped at 122 % of YS; and 1850A SN-5, tested in Glycerol and stopped at 112 % of YS. It is important to note that the samples were electropolished before EBSD analysis. This means that a thin layer has been removed from the surface. Therefore, the surface imaged by EBSD is not perfectly identical to the surface from the SEM images. However, as only a thin surface layer has been removed, the EBSD images will still represent the same cracks going through the same grains as in the SEM images.

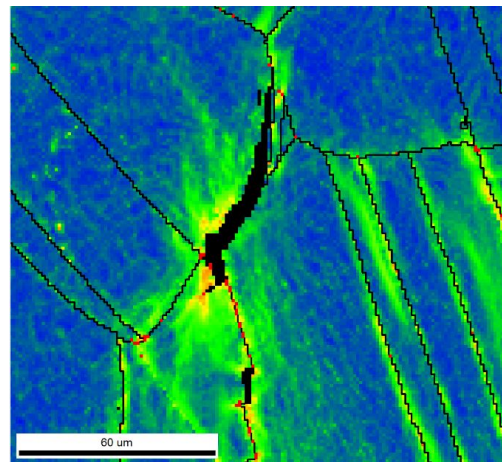




**Figure 4.48:** A SEM image of coarse grained sample 1900 SN-6, loaded to 122 % of YS in Glycerol. A crack can be seen along a grain boundary. 391X magnification.



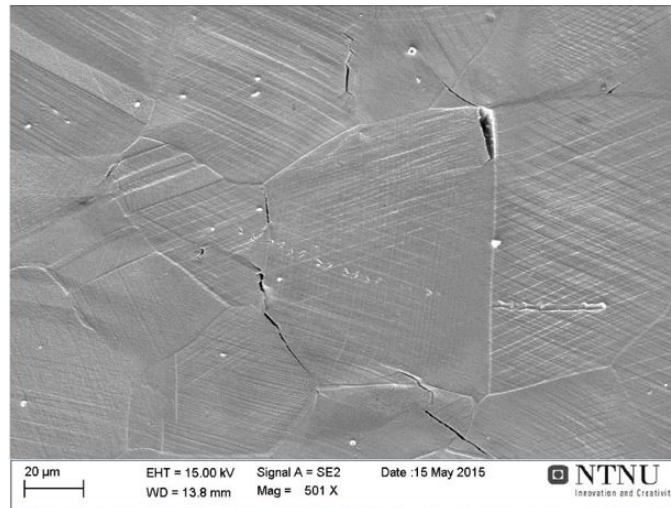
**Figure 4.49:** A grain map from sample 1900 SN-6; the same area as in Figure 4.48. 681X magnification.



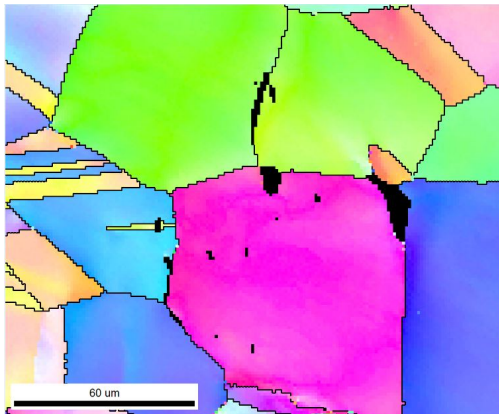
**Figure 4.50:** Kernel average misorientation map of an area from coarse grained 1900 SN-6. 681X magnification.

Figure 4.49 displays a color coded grain map of an area from sample 1900 SN-6. The black areas represents cracks. In Figure 4.50, a kernel average misorientation (KAM) map is displayed. This map displays the average misorientation of one point compared to its neighbouring points. Warmer colors indicate higher degrees of misorientation, which also signifies high deformation. It is clear from Figure 4.50 that the hydrogen induced secondary crack

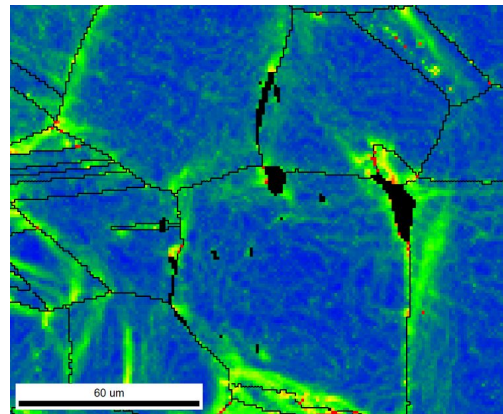
is surrounded by significantly deformed regions. These localized strains are indicative of enhanced local plasticity around hydrogen induced secondary cracks, supporting hydrogen induced local plasticity (HELP) as a mechanism for HISC.



**Figure 4.51:** A SEM image of sample 1900 SN-6. Cracks can be seen at the corners of grain boundaries. 501X magnification.



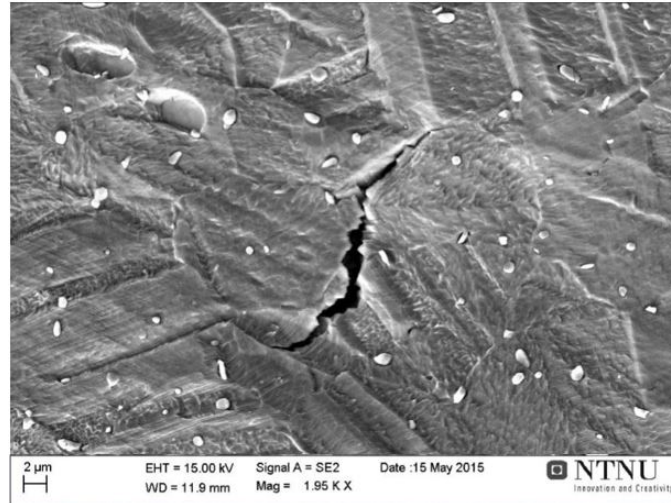
**Figure 4.52:** A grain map of an area from coarse grained 1900 SN-6; the same area as shown in Figure 4.51.



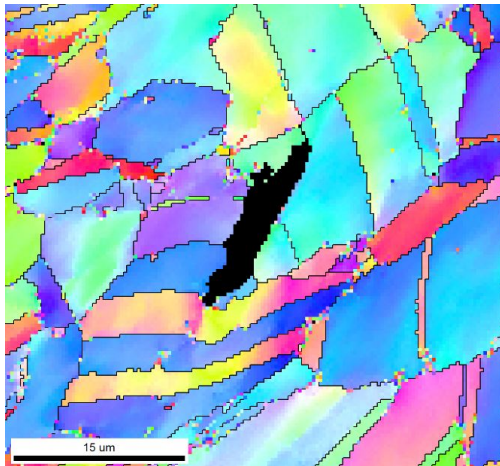
**Figure 4.53:** Kernel average misorientation map of an area from coarse grained 1900 SN-6.

Figure 4.52 displays a color coded grain map of an area from sample 1900 SN-6. The black areas represent cracks and particles. In Figure 4.53, a KAM map is displayed. The same tendency as in Figure 4.50 is displayed

here; regions of high deformation surrounding cracks, crack tips and grain boundary corners.



**Figure 4.54:** A SEM image of sample 1850A SN-5, loaded to 112 % of YS in Glycerol. A crack has propagated through several grains. 1950X magnification.



**Figure 4.55:** A grain map from the same area as in Figure 4.54 from fine grained 1850A SN-5.

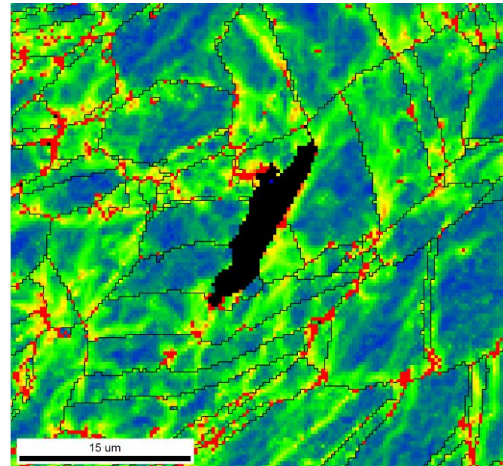


**Figure 4.56:** Kernel average misorientation map of an area from fine grained 1850A SN-5.

Figure 4.55 gives an example of transgranular crack growth in the fine grained material. Figure 4.56 shows how deformation is concentrated along grain boundaries, with especially high deformation at grain boundary corners, sug-

gesting that the transgranular crack probably initiated at a grain boundary corner.

## 4.8 In Situ Optical Microscope Images

Optical microscope image series were obtained from some of the tensile tests. The following section provides some of the image series that were captured. The deformation around the notch often led to a darkening of certain parts of the images, due to scattering of the light. Deformation would also make it more difficult to keep the image in focus. However, the image series occasionally proved successful at capturing propagating cracks at the notch root, as in Figures 4.61 through 4.64. The development of the microstructure of the coarse grained sample 1900 SN-6 is shown in Figure 4.57 to 4.64, going from zero load all the way to crack propagation at 119.7 % of yield strength.

The magnification of the images obtained from the optical microscope used for in situ testing was calculated to be roughly 160X.

### 4.8.1 Coarse Grained Material

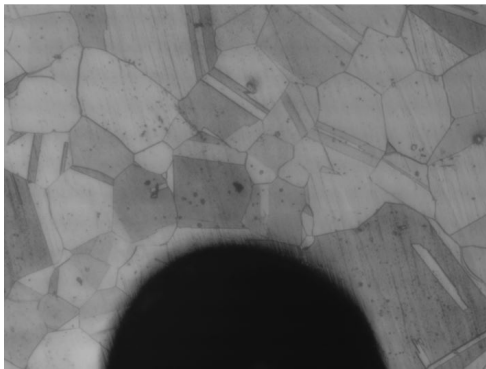


**Figure 4.57:** *In situ optical image of 1900 SN-6 in Glycerol at zero load. 160X magnification.*

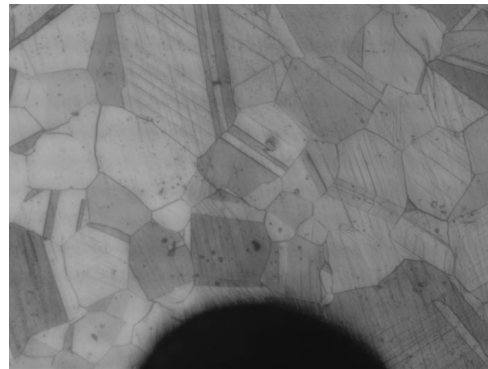


**Figure 4.58:** *1900 SN-6 in Glycerol at 793 MPa load (71 % of YS). 160X magnification.*



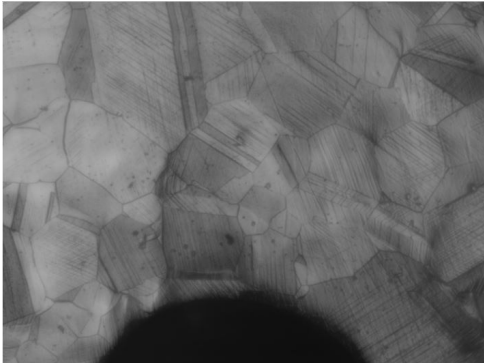


**Figure 4.59:** 1900 SN-6 in Glycerol at 1082 MPa load (97 % of YS). Slip lines are visible within the grains. 160X magnification.

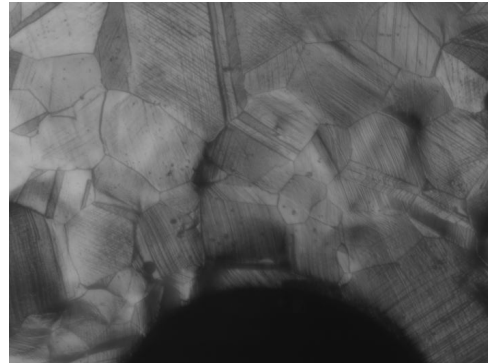


**Figure 4.60:** 1900 SN-6 in Glycerol at 1202 MPa load (108 % of YS). Some areas have begun to appear darker. 160X magnification.

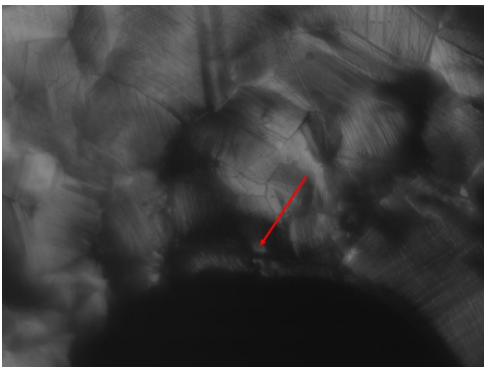


**Figure 4.61:** A crack has initiated at the notch root. 1310 MPa load (118 % of YS). 160X magnification.

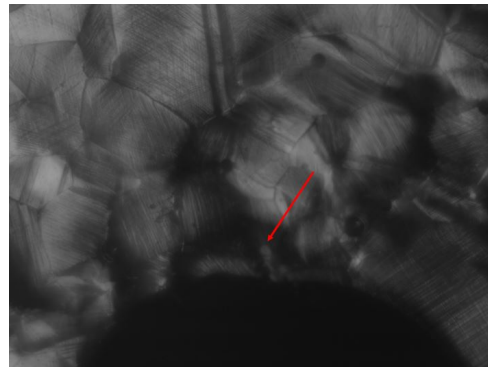


**Figure 4.62:** The crack can be seen propagating at the notch root. 1322 MPa load (119.0 % of YS). 160X magnification.

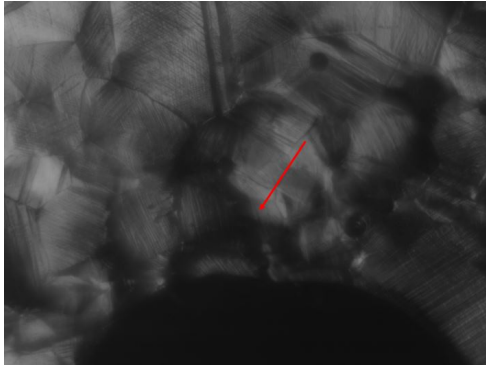


**Figure 4.63:** The crack can be seen propagating further at the notch root. 1327 MPa load (119.5 % of YS). 160X magnification.

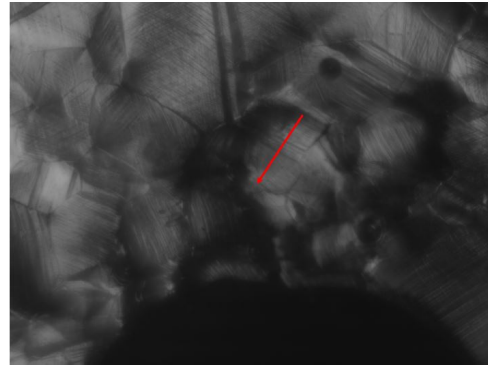


**Figure 4.64:** The experiment was stopped when the crack was discovered. 1329 MPa load (119.7 % of YS). 160X magnification.

The series of images from Figure 4.57 through Figure 4.64 display the loading of coarse grained sample 1900 SN-6 in Glycerol, from unloaded (Figure 4.57) to a propagated crack (Figure 4.64). The images gradually become darker, as deformation on the surface seemingly disperses more light. Due to hydrogen bubbles building up in the electrolyte, it also became increasingly more challenging to obtain clear and in-focus images.

#### 4.8.2 Fine Grained Material

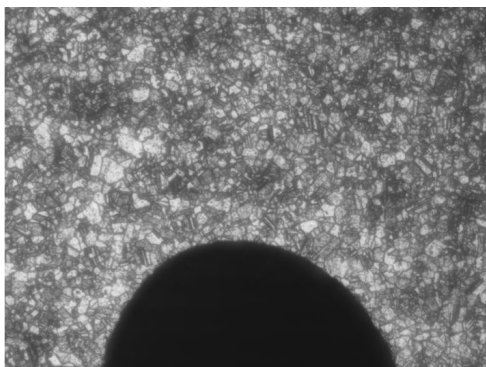


**Figure 4.65:** In situ optical image of 1850A SN-8 in Glycerol at zero load. 160X magnification.

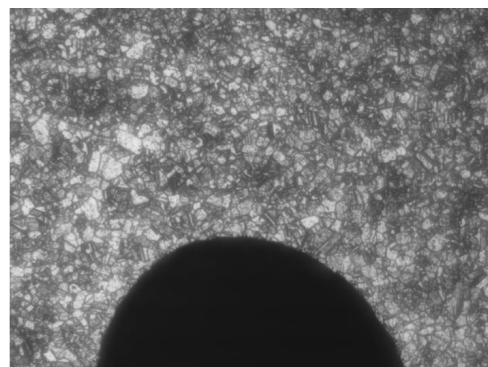


**Figure 4.66:** 1850A SN-8 in Glycerol at 782 MPa load (60 % of YS). 160X magnification.

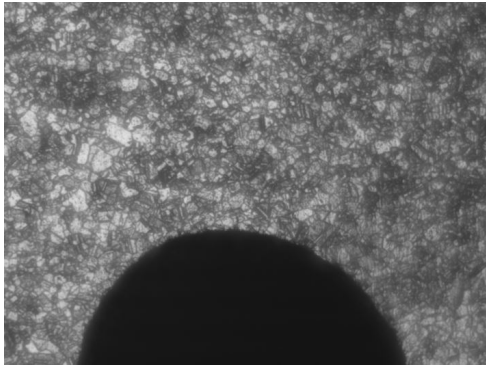


**Figure 4.67:** 1850A SN-8 in Glycerol at 1066 MPa (82 % of YS). 160X magnification.

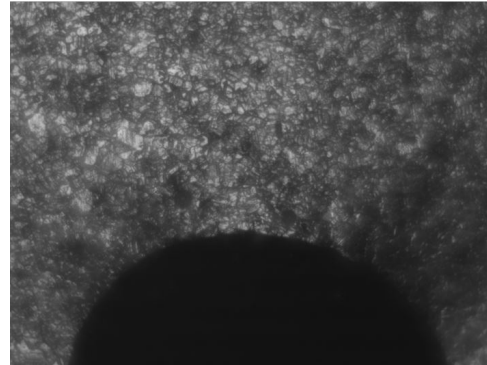


**Figure 4.68:** 1850A SN-8 in Glycerol at 1382 MPa load (106 % of YS). 160X magnification.

Figures 4.65 through 4.68 displays in situ optical images of sample 1850A SN-8 in Glycerol. It can be seen in Figure 4.68 that deformation is beginning to make the image darker. It is also less clear than the previous ones, due to small bubbles floating in the electrolyte. Still, the microstructure of the fine grained material provides the optical in situ images with a random greyscale texture that is ideal for digital image correlation analysis. This particular series of images was therefore utilized in the attempt to use DIC to analyze the local strains surrounding the notch.

#### **4.9 An Attempt to Use Digital Image Correlation Technology to Map Strains**

One of the main objectives of this work was to investigate the possibility of using DIC software to analyze the images obtained with the optical microscope during testing. As this had not previously been attempted, the setup was continually subject to change in order to improve the image quality of the optical images, in an attempt to make analysis with DIC possible. The best image series were selected for DIC analysis. Using the eCorr v4.0 software, it was experimented with different settings and parameters for the sake of performing an analysis of the strain.

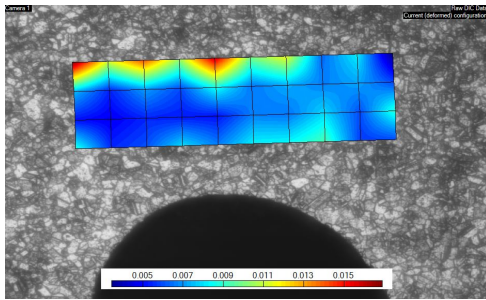


**Figure 4.69:** Superimposed strain map on an image of 1850A SN-8 in Glycerol at 118 MPa load (9 % of YS). 160X magnification.

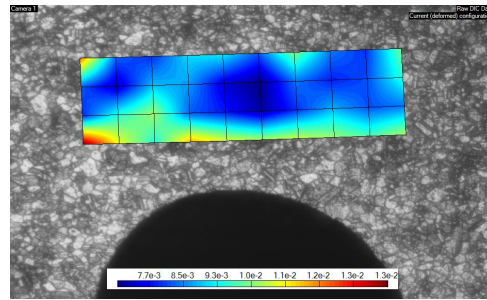


**Figure 4.70:** Superimposed strain map on an image of 1850A SN-8 in Glycerol at 616 MPa load (48 % of YS). 160X magnification.

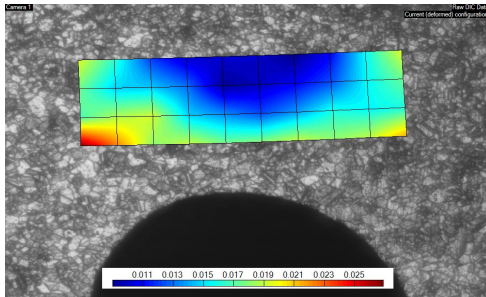


**Figure 4.71:** Superimposed strain map on an image of 1850A SN-8 in Glycerol at 923 MPa load (71 % of YS). 160X magnification.

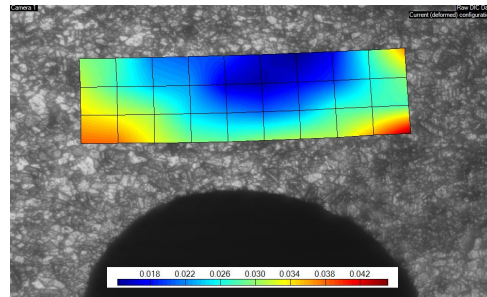


**Figure 4.72:** Superimposed strain map on an image of 1850A SN-8 in Glycerol at 1136 MPa load (88 % of YS). 160X magnification.

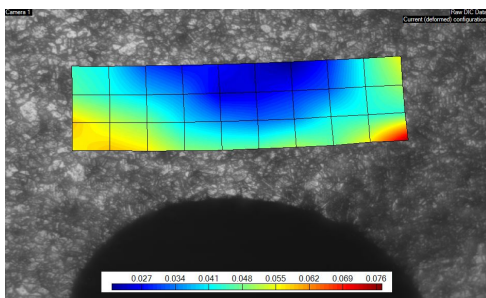


**Figure 4.73:** Superimposed strain map on an image of 1850A SN-8 in Glycerol at 1293 MPa load (100 % of YS). 160X magnification.

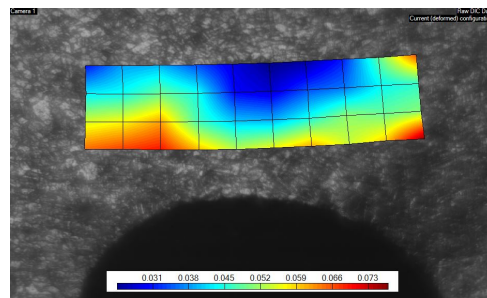


**Figure 4.74:** Superimposed strain map on an image of 1850A SN-8 in Glycerol at 1335 MPa load (103 % of YS). 160X magnification.



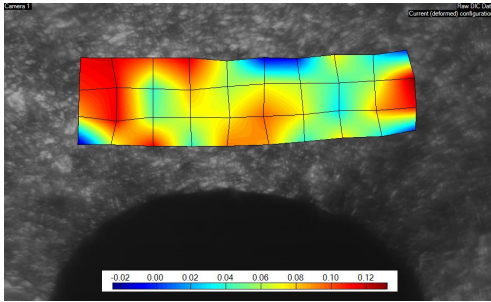


**Figure 4.75:** 1850A SN-8 in Glycerol at 1349 MPa load (104 % of YS). The DIC software has lost track of the microstructure, leading to breakdown of the strain map. 160X magnification.

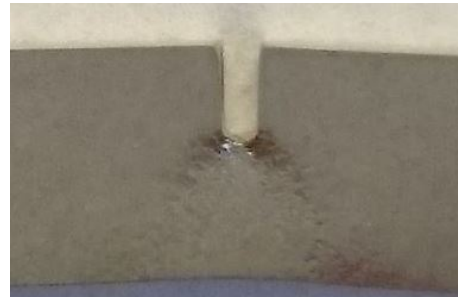


**Figure 4.76:** Deformation at the notch in a coarse grained sample strained until 122 % of YS. The lines at approximately 45° from the notch show areas of high deformation.

Figures 4.69 through 4.75 show how a standard mesh, generated in eCorr v4.0, has been used to track the movement of fixed spots on the sample surface, and used the collective movement of the nodes in the mesh to make a map of the principal strains in the sample. The color bar at the bottom of each picture represents the principal strain ( $\epsilon_1$ ); warmer colors indicate higher values of strain. The size of the mesh elements is 150 by 150 pixels. These images show that it is indeed possible to map the strains under the notch area, as long as the image quality is sufficient. The analysis shows that the strains are highest at approximately 45° angles to the notch root (indicated by red color at the corners of the mesh). This agrees with observations in SEM as well as the deformation observed macroscopically on the sample surface (Figure 4.76). Figure 4.75 shows what happens when the image quality deteriorates; the software loses track of the sample surface and produces a strain map that clearly does not represent reality.

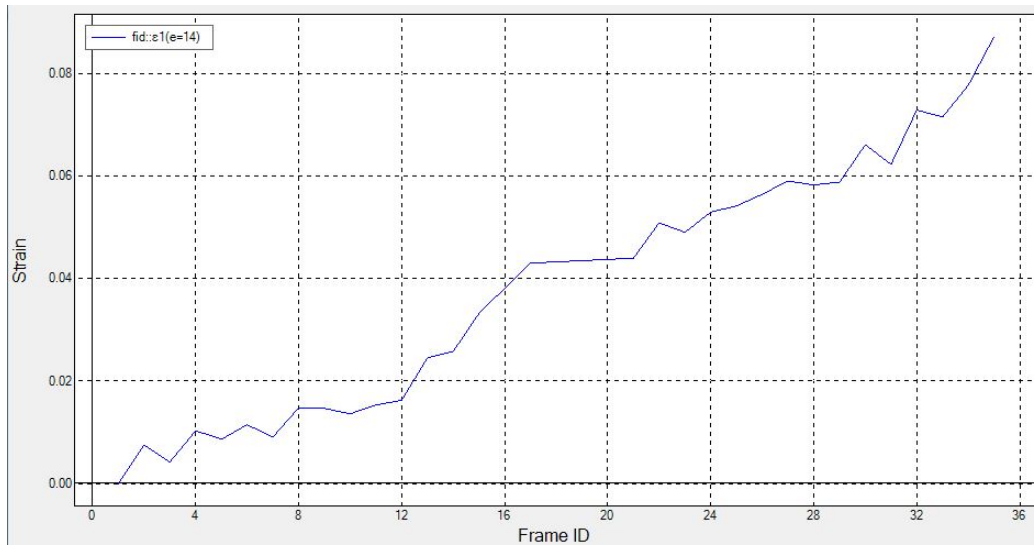


**Figure 4.77:** The graph shows the principal strain development for a mesh element from the center of the row closest to the notch in the mesh. Values start at 0 and pass through 0.05 at 104 % of YS at frame 23.

The principal strain of a single element is plotted in Figure 4.77. This is plotted for the element in the middle of the row closest to the notch. As the graph is from the same analysis as the images presented above, the data from the curve is not valid above 104 % of YS, corresponding to frame ID 23. The graph shows that the element experienced a strain of  $\varepsilon_1 = 0.05$  at 104 % of YS.

A custom mesh intended to fit the shape of the notch was designed by Ph.D. candidate Petter Henrik Holmstrøm from the Department of Structural Engineering at NTNU. The mesh is displayed in Figure 4.78. Due to the darkening of the images in the areas close to the notch, the mesh could not be successfully used in the analysis. It does, however, show that it is possible to make a mesh that is customized to fit the particular shape of the samples used in this master's thesis.

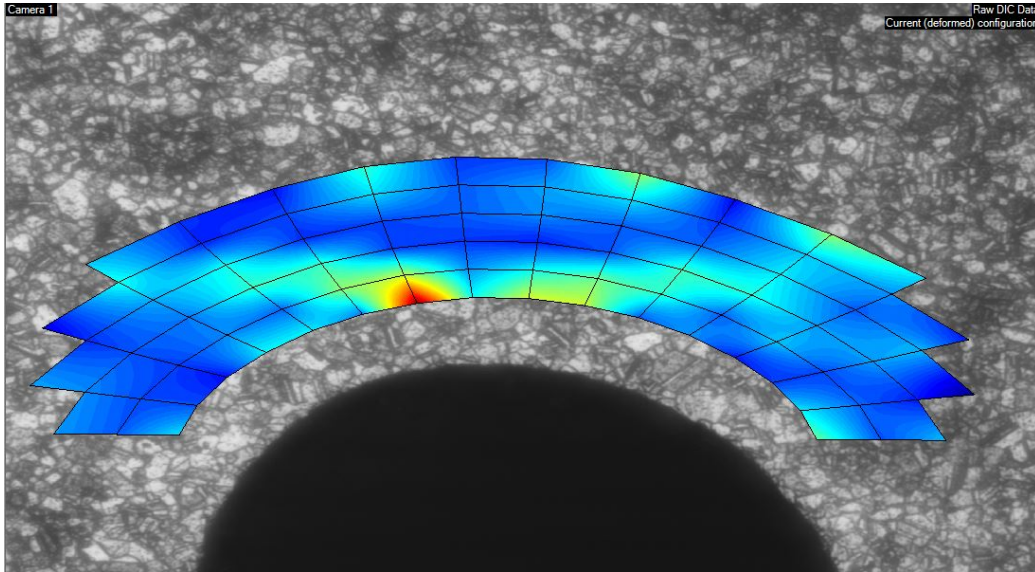


**Figure 4.78:** A custom mesh designed to fit the shape of the notch was designed in ABAQUS.

The DIC analysis performed here is very rough, when considering that the images might still contain some noise from vibrations in the setup, in addition to the fact that keeping the images in focus became a problem as the load increased above yield stress. Additionally, images were only obtained during the hourly increase of load, which means that the sample was subject to cold creep between each load increase. The above analysis should therefore only be seen as a visual representation of the principal strain localizations, and a first step toward developing this into a fully working method for accurately measuring strains during stepwise tensile testing with in situ cathodic polarization. For the sake of future continuation of this work, a user guide based on the experiences from this project was created. This is included in appendix C.

## 5 Discussion

### 5.1 Material Characterization

A characterization of the two versions of Inconel 718 that was tested in this work was performed, revealing a difference in grain size, particle content and shape.

The coarse grained 1900 material contained spherical NbC-particles and coarse TiN-particles, no  $\delta$ -particles were found when using EDS. The fine grained 1850 material contained rectangular  $\delta$ -particles, in addition to coarse TiN-particles. The  $\delta$ -particles far outnumbered the TiN-particles in this case. In the fine grained material, the total particle content was found to be about 10 times as high as in the coarse grained material. The marked difference in content of  $\delta$ -particles might lead to a difference in susceptibility to HISC for the two materials. It has been reported by several articles that  $\delta$  lowers ductility [5] and decreases resistance to hydrogen embrittlement [19] [20].

### 5.2 Fracture Tests

The main purpose was to obtain reference values for fracture loads, to be used in the stop tests. Still, some valuable information can be extracted from these experiments.

Even though the number of samples is low, the results are valuable when used to support other similar results. It was found that in situ charging with hydrogen lowered the yield strength of both materials when compared to samples tested in air. This supports a trend that was observed in project works prior to this master's thesis [9]. However, while results from the project work found that the fine grained material experienced a higher reduction in YS, the opposite has been found in the present work (higher reduction for coarse grained material).

In the present work, the fine grained 1850A was shown to experience a more severe reduction in ductility (reduction of RA) than the coarse grained 1900. This difference in reduced ductility was predicted by the difference in  $\delta$ -particles [5]. However, the coarse grained material displayed a larger brittle area in the fracture surface. The difference in  $\delta$ -content, as well as the contradicting evidence from reduction in YS, ductility and extent of brittle areas make it challenging to reach a clear conclusion on the effect of grain size on the susceptibility to hydrogen embrittlement.

Investigation of the fracture surfaces in SEM provided clear evidence that Inconel 718 is indeed affected by hydrogen embrittlement. The samples fractured in air exhibited ductile features across the entire fracture surface. Samples tested with hydrogen charging displayed typical transgranular brittle features in the surface area close to the notch. This is concurrent with the fact that when a stress is applied, hydrogen will diffuse under a stress gradient toward places of high stress [37]. All the samples exhibited ductile, dimpled features in the center of the fracture surfaces. For the specimens charged in situ with hydrogen, a brittle crack had propagated transgranularly from the notch root. According to Robertson et al., the fracture mode depends on the details of the hydrogen distribution. Transgranular fracture is observed when hydrogen distribution is enhanced at the tip of a notch because that is where the hydrogen concentrates due to the stress field [27].

It is interesting to note that the fracture surfaces of all samples subjected to cathodic polarization show clear signs of brittle crack propagation, even though some samples were only charged for a few hours. Fine grained samples were charged between 4 and 5 hours before fracturing. The coarse grained material was charged approximately 7 hours before fracture. This suggests that having hydrogen present at the surface of a gradually loaded sample has a rapid effect when the crack is propagated by incremental loading.

### 5.3 Potential

The recorded potential-curves display a difference in potential for some of the samples. This difference was approximately 300 mV between the most positive and the most negative potential measured. The variation is believed to be due to a change in the etching fluid used to bring out the microstructure. A new batch of etching fluid was used for the samples exhibiting the most negative potentials. Although it was made following the same recipe, the new batch demanded longer etching times than the first batch. This is believed to have affected the oxide layer of the samples.

### 5.4 Stop Tests - Effects of Hydrogen on Crack Initiation and Propagation

The results from the stopped tensile tests are qualitative rather than quantitative, because they are based on visual inspection of material surfaces. This inspection has, however, been thoroughly conducted by use of optical microscope, scanning electron microscope, and techniques such as EBSD.

Without hydrogen present on the surface, neither of the two materials exhibited any secondary cracking. A large crack would develop in the rough area inside the notch, and the samples would fracture by ductile mechanisms as this crack propagated. Not even at the fracture load could any signs of secondary crack initiation be observed.

When subjected to in situ cathodic polarization, both materials exhibited severe secondary cracking at higher loads. Even at the lowest stop-loads, it was possible to detect one or two beginning surface cracks. However, more than a few secondary cracks should be present in order to safely assume that hydrogen embrittlement is the reason for crack initiation. R. N. Parkins stated that as one or two small cracks in the necked region may be the result of near-surface inclusions, environmentally initiated or assisted cracking may be associated with multiple cracks not just confined to the necked region ([69] via [45]).

For the coarse grained P3A01-1900 material, crack initiation largely begun at grain boundaries, corners of grain boundaries and twins when hydrogen was present at the surface. This was evidenced by a trend in the SEM images at all loads, and by EBSD images confirming that cracks had indeed initiated grain boundaries. Kernel average misorientation maps showed localized deformation at grain boundaries, twins and grain boundary corners, making it further plausible that cracks would initiate there. Theory also supports grain boundaries as areas that may be especially vulnerable to HE: Brass et al. have shown that there are cases of preferential diffusion along grain boundaries in stable FCC structures, such as nickel or stainless steel [47] [48]. Also, hydrogen will diffuse under a stress gradient toward places of high stress [37]. Since the grain boundaries and twins were shown to experience local high strains, it is conceivable that hydrogen may have concentrated in these areas. Still, as cracks developed past the confines of a single grain, they would generally propagate transgranularly. This is also evidenced by the fracture surfaces of the fractured samples, exhibiting pure transgranular fracture near the notch. This suggests that the grain boundaries both on the surface and inside the material had not been weakened enough by environmental effects for cracks to propagate intergranularly.

The fine grained 1850A material first displayed signs of secondary cracking above 108 % of yield strength. Several examples of crack initiation at grain boundaries and twins were found. However, as the grains were small, it was more difficult to decipher a trend in the initiation sites for the fine grained material than for the coarse grained. Cracks were regularly seen to have

propagated across grains, but initiation points were harder to determine. Examination by EBSD yielded grain maps and kernel average misorientation maps, which displayed crack propagation across several grains. The KAM maps revealed very high deformation density along grain boundaries compared to the matrix. This establishes as probable that crack initiation happens preferentially at grain boundaries for the fine grained material as well. From the fracture surfaces imaged in SEM, it was found that crack propagation happens transgranularly.

The kernel average misorientation maps collected from materials of both grains sizes show that hydrogen induced cracks are surrounded by significantly deformed regions. This is especially evident in Figure 4.50. According to Laureys et al., such local high strains indicate that crack growth is probably accompanied by local plastic deformation, suggesting that the HELP mechanism might be the dominating mechanism for hydrogen induced stress cracking in this instance [54]. The hydrogen enhanced localized plasticity model is based on observations that the presence of hydrogen in solid solution will increase the mobility of dislocations, increasing the dislocation density at crack tips, which creates regions with localized high deformation.

Cracked particles could be found at the surface of the material, even when stopped at low loads. Surprisingly, no indication was found that particles affected the initiation or propagation of cracks. The cracks in particles were halted immediately when they encountered the matrix. In both materials, it was found that coarse particles containing Ti and N would crack at low loads, but no evidence of cracks propagating from these was found in any of the samples.

There is obviously a significant difference in crack initiation with and without hydrogen present at the surface. All samples tested in air presented without any signs of secondary cracking, whereas all samples tested with cathodic polarization showed at least some signs of surface cracking. At higher load, secondary cracking was highly prevalent in the samples exposed to hydrogen. The environmental hydrogen has clearly affected the Inconel 718 material, confirming that it is susceptible to hydrogen embrittlement.

## 5.5 Effect of Grain Size on Hydrogen Embrittlement

No clear difference in crack initiation or propagation was found between the two materials. Cracks appeared to initiate at the same places, and both

grain sizes displayed transgranular crack propagation. Some differences were found in the fracture test results, as discussed above. The coarse grained 1900 material experienced a larger reduction in yield strength when exposed to hydrogen. However, as only one sample was tested for each condition for the 1900 material, this is not enough to conclude unless all results point to the same conclusion. The fine grained 1850A material exhibited the most severe reduction in ductility, but the coarse grained material displayed the largest brittle areas. Clearly, these results are not concurrent.

The marked difference in content of  $\delta$ -particles, combined with literature suggesting  $\delta$  is crucial to HE susceptibility, renders it impossible to reach a certain conclusion on what effect the grain size of Inconel 718 has on hydrogen embrittlement.

## 5.6 Development of New Equipment and Experimental Setup

New equipment was developed over the course of this work. New electrolyte chambers used for environmental exposure were developed, based on a previous design by Haaland [41] and Stenerud [66] and Krosness [67]. The new design comprised the front half of a chamber, designed to provide equal amounts of electrolyte on both sides of the sample, in addition to a glass window. The glass window provided an improved view of the sample surface compared to the old design. This made it possible to obtain detailed pictures of the microstructure of the materials, even when tested in electrolyte.

Vibrations in the images presented a problem, as they made it impossible for the DIC software to distinguish between vibrations and actual strain. Steps were taken to alleviate this, including moving the whole setup to a room without other experiments, in order to eliminate vibrations from nearby equipment such as aquarium pumps. Most of the vibrations were successfully eliminated. However, some noise might still originate from very small vibrations. Further improvements could be made in future work, for instance by purchasing a stand from the manufacturer of the microscope. The stand currently used for the microscope was developed in this project, using an x-y micro movement stage and a height adjustable plate originally intended for other equipment. It should also be attempted to solve the problem with images getting darker as the load and deformation increases.



## 5.7 Test Method

The tensile test method used in this work is an easy-to-use method for performing tests of susceptibility to HISC of various material. The fact that the loading of samples is carried out by hand, and the fact that the tensile machines are relatively small, ensures that the setup is both portable and has a low operating cost. The need for manual increase of loads at regular intervals does, however, demand that an operator is present for most of the experiments, which could be several hours long. The basic tensile testing equipment can be used for regular tensile testing and for testing with environmental exposure, as done in the present work.

The fact that load increases are performed manually introduces some inaccuracies when considering application of exact load. It also makes it nearly impossible to maintain the load at a constant value over time, as this calls for an operator to manually adjust the load throughout the duration of the experiment. Nonetheless, the manual operation does have some advantages. It was found that with practice, the relaxation (cold creep) of the samples could be used to detect the formation of small cracks at the notch root. One could, with relative ease, sense the significant increase in relaxation of the sample when a crack started to propagate. This was especially convenient when performing the stop tests in this work. The tensile equipment is therefore considered to be suitable for crack initiation experiments.

There is still room for improvement of the test method. Although the setup now includes the possibility of measuring load and testing with environmental exposure, a very useful addition to the setup would be an integrated means of measuring elongation. It is possible to measure the reduction of area (RA) fairly accurately, by measuring the sample before and after testing, but measuring elongation is problematic, especially with fractured samples. If a strain gage, or similar equipment, could be implemented into the existing setup, this would represent a valuable addition to the information that can be collected with this equipment. One such attempt was made in this work, by investigating the possibility of using DIC analysis of images obtained during testing. However, this method, which will be discussed further below, is more suitable for measuring local strains.

An optical microscope connected to a digital camera was utilized to provide images of the material surface during the tensile experiments. The purpose was to capture the development of the microstructure and be able to detect initiating cracks at an early stage, as well as to obtain series of images that could be used for analysis with DIC technology. As has been demonstrated

by the images in section 4.8, the image quality deteriorated as the specimens were strained at higher loads. This is probably a result of deformation in the sample dispersing light differently as more deformation was introduced, as well as small bubbles building up in the viscous Glycerol electrolyte. Reduced image quality made it challenging to detect early cracks, as they would not initiate until the surface was significantly deformed. This made it difficult to discern cracks from other dark areas. It was eventually learned that by using an image viewing program that allowed the operator to quickly play through the images that were captured so far, in a movie-like fashion, cracks could more easily be detected. Playing through the images in this fashion made cracks more detectable, because these would appear and begin to propagate more quickly than the other dark areas when viewed in quick succession.

In the present work and in preceding master's theses [70] [41], the load has been given as % of yield strength. Due to the notch effect, the YS of a notched sample may differ from an un-notched sample. This means that the notched samples may not actually begin to yield at 100 % of the YS used in this work. This may have an effect on the results and an alternative to % of YS should be explored. In conjunction with this project, a simulation of a tensile test was made in ABAQUS by Haiyang Yu at Department of Structural Engineering at NTNU. This was completed late in the semester and was therefore not utilized in the present work. It may, however, be suitable for use in future work.

## 5.8 Digital Image Correlation - Progress Made and Future Potential

It was attempted to map principal strains on the specimen surface by use of eCorr v4.0 digital image analysis software. The attempt proved partly successful, in the sense that a map showing the development of strain in a series of images was successfully created, although the analysis could not be performed on a full series of images. The images at high loads were too dark to allow analysis in eCorr. Hydrogen bubbles would gather in the Glycerol electrolyte, and some of these were so small that they would not leave the electrolyte. This, in addition to surface deformation, contributed to lower the image quality as the experiment went on. However, it might be possible to improve the image quality by performing the cathodic polarization in a different electrolyte or by experimenting with different light sources.

The microstructure of the fine grained material was found to be suitable for digital image correlation analysis. As long as the images remained clear and

relatively bright, analysis using DIC could be successfully performed. The coarse grained microstructure was, on the contrary, not fit for DIC. The mesh used for analysis should have a mesh size fitting at least three grains (or other pattern element) inside one mesh element. This demanded a senselessly large mesh size at the magnification used in our images. That is not to say that DIC analysis of the coarse grained alloy is not possible, only that it might not be suitable for analysis at the current magnification.

As this was a first attempt at using DIC to map strains in optical images from in situ hydrogen tensile testing, the main objective was to investigate whether or not it was possible. This work has provided promising results, which suggest that the use of DIC to map strains using only the etched metal surface as contrast pattern is indeed possible. However, the setup is not fully developed. DIC analysis was not possible at higher loads. Therefore, further efforts should be made to improve the image quality at higher loads, in order to perform analysis from zero load until crack initiation. Efforts to further reduce vibrations will also be key in developing this into a successful method.

## 5.9 Validity of the Results

For the fractures tests, the number of samples were limited. This should be considered when evaluating these results. The low number of samples makes the results vulnerable to scatter and inaccuracies in measuring methods. Therefore, the need for concurrent results is high when attempting to use the fracture results to determine effects of hydrogen or grain size. A conclusion in one direction or the other with regard to the effect of grain size is therefore not justifiable due to conflicting evidence. On the other hand, the evidence for transgranular crack propagation is high. This was evidenced by all samples in the fracture tests. The same was proven in project work leading up to this work [9]. Additionally, the stop tests indicated transgranular crack propagation for materials of both grain sizes.

Some results, such as the measurement of cross sectional area after fracture, are subject to some inaccuracy due to the method of measurement. It was assumed that the cross sectional area could be approximated by a perfect rectangle, an assumption which is not entirely true. However, as it was difficult to find better alternatives, it was believed that this measuring method would at least provide an indication of the reduction of ductility. Other results include the EDS measurements. In these, particles of different chemical content were categorized on the basis of the EDS results. The EDS is not a perfect tool for measuring chemical content, and will have some error in

its measurements. On the other hand, the measurement of chemical content in the matrix was proven to be reasonably accurate. This suggests that the particle measurements probably should have a similar level of accuracy. The ratio of the main elements in particles such as NbC and TiN was not perfect, though they were still interpreted as evidence for the mentioned particles. Theory gives some support to these conclusions, by predicting the particles normally present in this alloy.

The SEM results from the stop tests are qualitative rather than quantitative. Although more than a thousand SEM images were obtained in this work, the conclusions from the stop tests are based on the qualitative evaluation of these images. An attempt to quantify the number of cracks and initiation sites was not made here. The results are, however, supported by SEM, EBSD and theory.

The difference in particle content is considered one of the reasons why a conclusion on the effect of grain size is not justifiable based on this work. As previously mentioned, the literature reports that  $\delta$ -particles will have an unfavorable effect on mechanical properties. In future attempts to investigate the effect of grain size on hydrogen embrittlement, materials with comparable amounts of particles should be used. It should also be considered using different starting loads for the two grain sizes, in order to provide equal hydrogen charging times.

## 6 Conclusion

### 6.1 Conclusion

The following conclusions have been reached in this project:

- Two versions of Inconel 718 (UNS N07718) were characterized, revealing different types of particles in the two. No  $\delta$ -particles were found in the coarse grained P3A01-1900. Significant amounts of  $\delta$ -particles were found in the fine grained P3A01-1850A. Other particles were also found to be present in both materials.
- Inconel 718 is susceptible to hydrogen induced stress cracking, as evidenced by embrittled fracture surfaces and secondary cracking. This is true for both fine and coarse grained material.
- No secondary cracking was found in samples tested in air.
- Secondary cracking was found in all samples tested with cathodic polarization.
- Crack initiation at the sample surface happened preferentially at grain boundaries, grain boundary corners and twins.
- Crack propagation happened transgranularly.
- Hydrogen induced localized plasticity (HELP) is assumed to be the dominating mechanism for HISC, as suggested by significantly deformed regions near the crack edge and surrounding the crack tip.
- Particle content does not appear to affect crack initiation, as no evidence of this was found.
- A method for using digital image correlation technology to map local strains from in situ tensile testing was developed, although more work is necessary to refine the method and setup.
- Fine grained microstructure in Inconel 718 provides a suitable contrast background for DIC; coarse grained Inconel 718 is not suitable at the magnification used in this work.

## 6.2 Recommendations for Future Work

- The effect on grain size on HE in Inconel 718 is still not resolved. More work should be performed in order to contribute to a better understanding of this effect.
- In future attempts to examine the effect of grain size, material with equal amounts of  $\delta$ -particles should be used.
- A larger number of samples should be tested when performing fracture tests, in order to reach statistically significant results.
- The method for using DIC to measure strain should be developed further, with emphasis on improving the image quality and reduce vibrations even further.
- Improving the microscope stand or purchasing equipment for this purpose should be considered.
- Fine grained materials should be used in future work with DIC. If coarse grained materials are to be examined, it may be necessary to reduce the magnification.
- The ABAQUS model developed by Haiyang Yu may be used in future work to predict when yielding will occur.
- Finding a way of integrating equipment for measuring elongation into the existing setup would provide valuable information. This should be investigated further.

---

# References

- [1] H.-T. Lee and W.-H. Hou, “Development of fine-grained structure and the mechanical properties of nickel-based superalloy 718,” *Materials Science and Engineering: A*, vol. 555, pp. 13–20, 2012.
- [2] S. Metals, “Inconel alloy 718,” *Publication No. SMC-045, Special Metals Corporation, Huntington, WV, USA*, 2007.
- [3] L. Fournier, D. Delafosse, and T. Magnin, “Cathodic hydrogen embrittlement in alloy 718,” *Materials Science and Engineering: A*, vol. 269, no. 1, pp. 111–119, 1999.
- [4] Y. Yao, X. Pang, and K. Gao, “Investigation on hydrogen induced cracking behaviors of ni-base alloy,” *International Journal of Hydrogen Energy*, vol. 36, no. 9, pp. 5729–5738, 2011.
- [5] G. Sjöberg and D. Cornu, “Hydrogen embrittlement of cast alloy 718 effects of homogenization, grain size and  $\delta$ -phase,” *Superalloys 718, 625, 706 and various derivatives*, pp. 679–690, 2001.
- [6] S. A. McCoy, S. K. Mannan, C. S. Tassen, D. Maitra, and J. R. Crum, “Investigation of the effects of hydrogen on high strength precipitation hardened nickel alloys for o & g service,” *CORROSION 2015*, 2015.
- [7] S. Huizinga, W. E. Like, B. McLoughlin, J. De Jong, *et al.*, “Offshore nickel alloy tubing hanger and duplex stainless steel piping failure investigations,” *CORROSION 2003*, 2003.
- [8] A. P. D. S. S. Shademan J. W. Martin *et al.*, “Uns n07725 nickel alloy connection failure,” *CORROSION 2012*, 2012.
- [9] K. Knarbak, *The effect of grain size on hydrogen embrittlement of Inconel 718*. Project thesis [unpublished work]. Trondheim, Norway: Institutt for produktutvikling og materialer, Norwegian University of Science and Technology, 2014.
- [10] N. Stoloff, “Wrought and p/m superalloys,” *ASM International, Metals Handbook. Tenth Edition.*, vol. 1, pp. 950–977, 1990.
- [11] J. K. Solberg, *Teknologiske metaller og legeringer*. Trondheim, Norway: Department of Materials Science and Engineering, NTNU, 2011, ch. 5.
- [12] S. Azadian, L. Wei, and R. Warren, “Delta phase precipitation in inconel 718,” *Materials characterization*, vol. 53, no. 1, pp. 7–16, 2004.
- [13] M. J. Cieslak, G. A. Knorovsky, T. J. Headley, and A. D. Romig Jr, “The solidification metallurgy of alloy 718 and other nb-containing superalloys,” *Superalloy*, vol. 718, pp. 59–68, 1989.

- 
- [14] T. Antonsson and H. Fredriksson, "The effect of cooling rate on the solidification of inconel 718," *Metallurgical and Materials Transactions B*, vol. 36, no. 1, pp. 85–96, 2005.
- [15] A. Mitchell, A. Schmalz, C. Schvezov, and S. Cockroft, "The precipitation of primary carbides in alloy 718," *Superalloys 718, 625 and various derivatives*, p. 79, 1994.
- [16] J. Oblak, D. Paulonis, and D. Duvall, "Coherency strengthening in ni base alloys hardened by do22  $\gamma$ " precipitates," *Metallurgical Transactions*, vol. 5, no. 1, pp. 143–153, 1974.
- [17] M. Sundararaman, P. Mukhopadhyay, and S. Banerjee, "Some aspects of the precipitation of metastable intermetallic phases in inconel 718," *Metallurgical Transactions A*, vol. 23, no. 7, pp. 2015–2028, 1992.
- [18] A. Devaux, L. Nazé, R. Molins, A. Pineau, A. Organista, J. Guédou, J. Uginet, and P. Héritier, "Gamma double prime precipitation kinetic in alloy 718," *Materials Science and Engineering: A*, vol. 486, no. 1, pp. 117–122, 2008.
- [19] L. Liu, K. Tanaka, A. Hirose, and K. F. Kobayashi, "Effects of precipitation phases on the hydrogen embrittlement sensitivity of inconel 718," *Science and Technology of Advanced Materials*, vol. 3, no. 4, pp. 335–344, 2002.
- [20] L. Liu, C. Zhai, C. Lu, W. Ding, A. Hirose, and K. F. Kobayashi, "Study of the effect of  $\delta$  phase on hydrogen embrittlement of inconel 718 by notch tensile tests," *Corrosion science*, vol. 47, no. 2, pp. 355–367, 2005.
- [21] F. Galliano, E. Andrieu, C. Blanc, J.-M. Cloue, D. Connetable, and G. Odemer, "Effect of trapping and temperature on the hydrogen embrittlement susceptibility of alloy 718," *Materials Science and Engineering: A*, vol. 611, pp. 370–382, 2014.
- [22] G. E. Dieter and D. Bacon, *Mechanical metallurgy*. McGraw-Hill New York, 1986, vol. 3.
- [23] T. L. Anderson, *Fracture mechanics: Fundamentals and applications*. CRC press, 2005.
- [24] W. D. Callister Jr, *Materials Science and Engineering An Introduction, 7th edition*. New York, USA: John Wiley & Sons, Inc., 2007.
- [25] R. M. Latanision and H. Opperhauser, "The intergranular embrittlement of nickel by hydrogen: The effect of grain boundary segregation," *Metallurgical Transactions*, vol. 5, no. 2, pp. 483–492, 1974.



- 
- [26] H. K. Birnbaum, “Mechanisms of hydrogen related fracture of metals,” DTIC Document, Tech. Rep., 1989.
- [27] I. Robertson, T. Tabata, W. Wei, F. Heubaum, and H. Birnbaum, “Hydrogen embrittlement and grain boundary fracture,” *Scripta metallurgica*, vol. 18, no. 8, pp. 841–846, 1984.
- [28] J. P. Hanson, M. Seita, *et al.*, “Hydrogen embrittlement behavior in precipitation hardened ni-base alloys,” *CORROSION 2015*, 2015.
- [29] R. T. Qu, M. Calin, J. Eckert, and Z. F. Zhang, “Metallic glasses: Notch-insensitive materials,” *Scripta Materialia*, vol. 66, no. 10, pp. 733–736, 2012.
- [30] W. H. Johnson, “On some remarkable changes produced in iron and steel by the action of hydrogen and acids,” *Proceedings of the Royal Society of London*, vol. 23, no. 156-163, pp. 168–179, 1874.
- [31] N. Standard, *Petroleum, petrochemical and natural gas industries: Materials selection and corrosion control for oil and gas production systems (ISO 21457:2010)*. Standard Norge, 2010.
- [32] K. Andersen, *HISC in Super Duplex Stainless Steels: A study of the relation between microstructure and susceptibility to hydrogen induced stress cracking*. Master’s thesis. Trondheim, Norway: Institutt for materialteknologi, Norwegian University of Science and Technology, 2013.
- [33] R. Gangloff, *Comprehensive structural integrity, vol. 6, i. milne, ro Ritchie, and b. ksrihalco, eds*, 2003.
- [34] H. K. Birnbaum and P. Sofronis, “Hydrogen-enhanced localized plasticity - a mechanism for hydrogen-related fracture,” *Materials Science and Engineering: A*, vol. 176, no. 1, pp. 191–202, 1994.
- [35] S. P. Lynch, “Progress towards understanding mechanisms of hydrogen embrittlement and stress corrosion cracking,” *CORROSION 2007*, 2007.
- [36] R. Johnsen, B. Nyhus, S. Wästberg, G. Ø. Lauvstad, *et al.*, “New improved method for hisc testing of stainless steels under cathodic protection,” *CORROSION 2007*, 2007.
- [37] M. E. Stroe, *Hydrogen embrittlement of ferrous materials*. Belgium: Université Libre de Bruxelles, 2006.
- [38] S. P. Lynch, “Metallographic contributions to understanding mechanisms of environmentally assisted cracking,” *Metallography*, vol. 23, no. 2, pp. 147–171, 1989.

- 
- [39] R. Mittal, *Strengthening Mechanism of Metals*. National Institute of Technology Rourkela, 2009, vol. 3.
- [40] J. F. Lessar and W. W. Gerberich, “Grain size effects in hydrogen-assisted cracking,” *Metallurgical Transactions A*, vol. 7, no. 7, pp. 953–960, 1976.
- [41] A. C. Haaland, *Hydrogen induced stress cracking of alloy 718 : Effects of chemical composition and microstructure*. Master’s thesis. Trondheim, Norway: Institutt for produktutvikling og materialer, Norwegian University of Science and Technology, 2014.
- [42] R. M. Latanision and H. Opperhauser, “Further observations on the effect of grain boundary segregation in the hydrogen embrittlement of nickel,” *Metallurgical and Materials Transactions A*, vol. 6, no. 1, pp. 233–234, 1975.
- [43] K. Takasawa, Y. Wada, R. Ishigaki, and R. Kayano, “Effects of grain size on hydrogen environment embrittlement of high strength low alloy steel in 45 mpa gaseous hydrogen,” *Materials transactions*, vol. 51, no. 2, p. 347, 2010.
- [44] S.-L. Chou and W.-T. Tsai, “Effect of grain size on the hydrogen-assisted cracking in duplex stainless steels,” *Materials Science and Engineering: A*, vol. 270, no. 2, pp. 219–224, 1999.
- [45] G. Lauvstad, R. Johnsen, I. Asbjørnsen, M. Bjurström, and C.-G. Hjorth, “Resistance toward hydrogen-induced stress cracking of hot isostatically pressed duplex stainless steels under cathodic protection,” *Corrosion*, vol. 66, no. 11, pp. 115 004–115 004, 2010.
- [46] E. Bardal, *Korrosjon og korrosjonsvern, 2. edition*. Tapir Akademiske Forlag, 1994.
- [47] A. Oudriss, J. Creus, J. Bouhattate, C. Savall, B. Peraudeau, and X. Feaugas, “The diffusion and trapping of hydrogen along the grain boundaries in polycrystalline nickel,” *Scripta Materialia*, vol. 66, no. 1, pp. 37–40, 2012.
- [48] A. M. Brass and A. Chanfreau, “Accelerated diffusion of hydrogen along grain boundaries in nickel,” *Acta Materialia*, vol. 44, no. 9, pp. 3823–3831, 1996.
- [49] A. M. Brass and J. Chene, “Influence of deformation on the hydrogen behavior in iron and nickel base alloys: A review of experimental data,” *Materials Science and Engineering: A*, vol. 242, no. 1, pp. 210–221, 1998.

- 
- [50] A Kimura and H. Birnbaum, “Hydrogen induced grain boundary fracture in high purity nickel and its alloys—enhanced hydrogen diffusion along grain boundaries,” *Acta Metallurgica*, vol. 36, no. 3, pp. 757–766, 1988.
- [51] W. M. Robertson, “Hydrogen permeation and diffusion in inconel 718 and incoloy 903,” *Metallurgical Transactions A*, vol. 8, no. 11, pp. 1709–1712, 1977.
- [52] M. Skjellerudsveen, O. M. Akselsen, V. Olden, R. Johnsen, and A. Smirnova, “Effect of microstructure and temperature on hydrogen diffusion and trapping in x70 grade pipeline steel and its weldments,” *EuroCorr 2010. Moscow*, 2010.
- [53] B. G. Pound, “Hydrogen trapping in precipitation-hardened alloys,” *Acta metallurgica et materialia*, vol. 38, no. 12, pp. 2373–2381, 1990.
- [54] A Laureys, T. Depover, R. H. Petrov, and K. Verbeken, “Microstructural characterization of hydrogen induced cracking in trip steels by ebsd,” in *Advanced Materials Research*, Trans Tech Publ, vol. 922, 2014, pp. 412–417.
- [55] J. Lufrano and P. Sofronis, “Enhanced hydrogen concentrations ahead of rounded notches and cracks—competition between plastic strain and hydrostatic stress,” *Acta materialia*, vol. 46, no. 5, pp. 1519–1526, 1998.
- [56] T. Tabata and H. K. Birnbaum, “Direct observations of hydrogen enhanced crack propagation in iron,” *Scripta metallurgica*, vol. 18, no. 3, pp. 231–236, 1984.
- [57] G. Stenerud, R. Johnsen, and J. S. Olsen, “The susceptibility to hydrogen induced stress cracking for uns n07718 and uns n07725 under cathodic polarization,” *CORROSION 2015*, 2015.
- [58] S. J. Kernion, J. H. Magee, K. A. Heck, and T. N. Werley, “Effect of microstructure and processing on the hydrogen embrittlement of ni-base superalloys,” *CORROSION 2015*, 2015.
- [59] N. McCormick and J. Lord, “Digital image correlation,” *Materials today*, vol. 13, no. 12, pp. 52–54, 2010.
- [60] eCorr v4.0, *Ecorr v4.0 documentation*, May 2015. [Online]. Available: <http://folk.ntnu.no/egilf/ecorr/doc/>.
- [61] A. J. Schwartz, M. Kumar, B. L. Adams, and D. P. Field, *Electron backscatter diffraction in materials science*. Springer, 2009, vol. 2.

- 
- [62] F. Humphreys, "Review grain and subgrain characterisation by electron backscatter diffraction," *Journal of materials science*, vol. 36, no. 16, pp. 3833–3854, 2001.
- [63] Pace Technologies, *Metallographic etchants*, Apr. 2015. [Online]. Available: <http://www.metallographic.com/Etchants/Etchants.htm>.
- [64] Struers<sup>TM</sup>, *Struers a2-i material safety data sheet*, Apr. 2008. [Online]. Available: [http://www.struers.com/resources/elements/12/87066/ELECTROLYTE%20A2-I%20\(M1201010%20-%202008-04-21\).pdf](http://www.struers.com/resources/elements/12/87066/ELECTROLYTE%20A2-I%20(M1201010%20-%202008-04-21).pdf) (Retrieved 29.05.2015).
- [65] Struers<sup>TM</sup>, *Struers a2-ii material safety data sheet*, May 2008. [Online]. Available: [http://www.struers.com/resources/elements/12/87068/ELECTROLYTE%20A2-II%20\(M1201002%20-%202008-04-21\).pdf](http://www.struers.com/resources/elements/12/87068/ELECTROLYTE%20A2-II%20(M1201002%20-%202008-04-21).pdf) (Retrieved 29.05.2015).
- [66] G. Stenerud, *Investigation of the effect of microstructure and inclusion content on hydrogen embrittlement in alloy 718*. Project thesis [unpublished work]. Trondheim, Norway: Institutt for produktutvikling og materialer, Norwegian University of Science and Technology, 2013.
- [67] O. M. Krosness, *Connection Between Critical Stress and Hydrogen Content for SDSS under Cathodic Protection*. Master's thesis. Trondheim, Norway: Institutt for produktutvikling og materialer, Norwegian University of Science and Technology, 2014.
- [68] Gamry Instruments, *Reference electrodes*, Dec. 2014. [Online]. Available: <http://www.gamry.com/products/accessories/reference-electrodes/>.
- [69] R. N. Parkins, "Slow strain rate testing-25 years experience," *ASTM SPECIAL TECHNICAL PUBLICATION*, vol. 1210, pp. 7–7, 1993.
- [70] G. Stenerud, *The Susceptibility to Hydrogen Induced Stress Cracking for Alloy 718 and Alloy 725*. Master's thesis. Trondheim, Norway: Institutt for produktutvikling og materialer, Norwegian University of Science and Technology, 2014.

# Appendix A

## Parameters for Sample Preparation Using Struers TegraPol-31

*Table A.1: First polishing step after grinding.*

Struers TegraPol-31 Step 1	
Surface	MD-Largo
Suspension	DiaPro All/Lar. 9 $\mu\text{m}$
Process time	4m 00s
Disc rotation speed	150 rpm

*Table A.2: Second polishing step.*

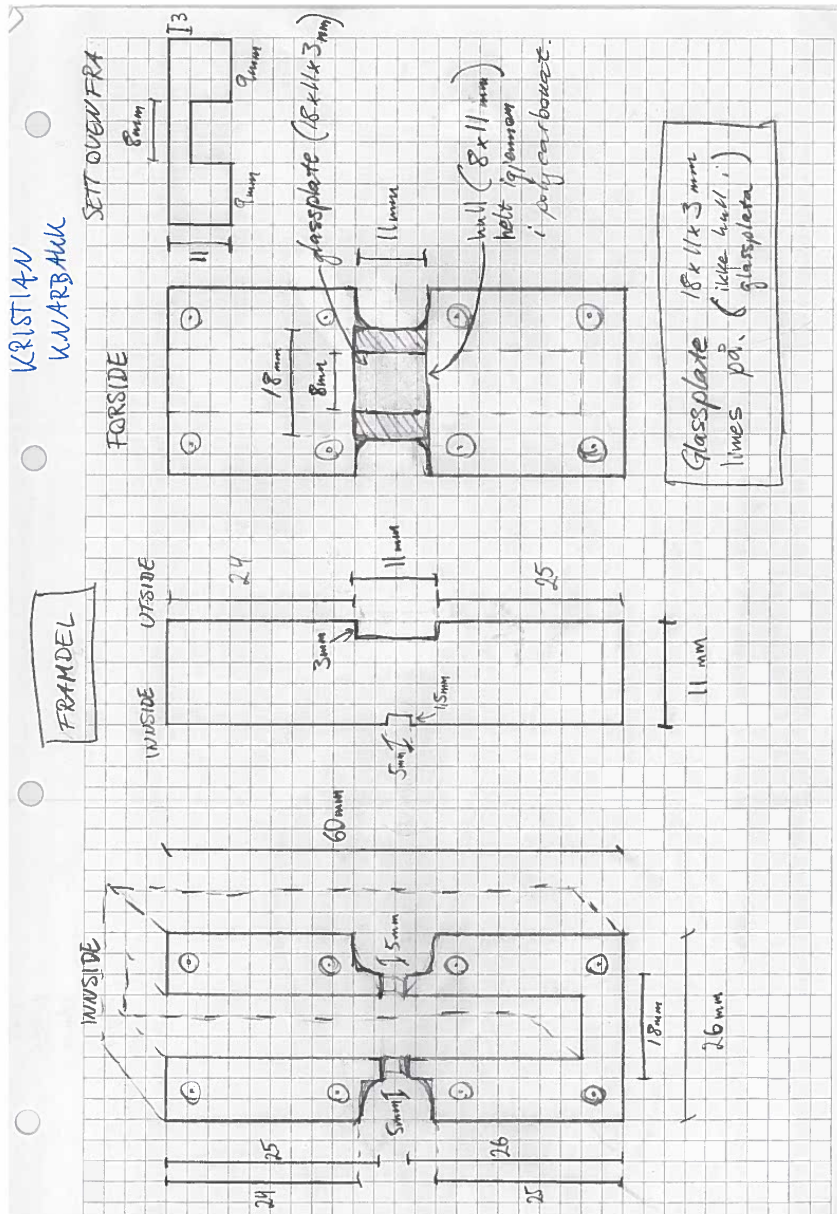
Struers TegraPol-31 Step 2	
Surface	MD-Dac
Suspension	DiaPro Dac 3 $\mu\text{m}$
Process time	4m 00s
Disc rotation speed	150 rpm

*Table A.3: Third and final polishing step.*

Struers TegraPol-31 Step 3	
Surface	MD-Nap
Suspension	DiaPro Nap-B 1 $\mu\text{m}$
Process time	3m 00s
Disc rotation speed	150 rpm

# Appendix B

## Electrolyte Chamber Working Drawing



# Appendix C

## eCorr v4.0 User Guide

Presented here is a user guide for eCorr v4.0, based on the experiences from this project. It is important to note that all images to be analyzed must have names on the form "UT\_0001", "UT\_0002" etc. All image names must be equally long and be numbered in increasing order. Images should be in black and white. The format should be bitmap (.bmp). No compressed formats should be used. When imaging the sample surface, a marker should be put on the screen at the notch root. This will help in adjusting the position of the microscope in order to keep the notch root at the same place throughout the experiment.

1. Open the PreProcessor by right-clicking PreProcessor and choosing "open PreProcessor" (Figure C.1).
2. Once in the PreProcessor, load the first image in the series of images to be analyzed. A picture is loaded by clicking the floppy disk icon and selecting "load image".
3. Press "fix aspect" (the icon with two crossing arrows).
4. In the menu on the right hand side of the screen, select "mesh generation".
5. To generate a standard square mesh, select "Generate structured Q4 mesh".
6. Choose element width and height in pixels.
7. The mesh can be moved or rotated by pressing "translate mesh" or "rotate mesh", respectively, in the Mesh Edit section.
8. Save the mesh in its own folder, preferably named after its size (e.g. 150x150).
9. Close the PreProcessor.
10. Make an input file by right-clicking "DIC" and selecting "New empty input file" (Figure C.2).
11. Right-click on "image folder" on the left in the input file editor window and select "browse image folder".

- 
12. Index the images by pressing "auto find" to the right in the input file editor window.
  13. Choose the mesh file by right-clicking "MeshFile" on the left hand side of the window and selecting "Browse mesh file". Select the mesh made previously.
  14. In the section called "DIC Core", select Multi-thread and type in the number of processor core you wish to use (most new computers have 4 core processors). This will affect the speed of the analysis.
  15. It is now possible to start the analysis. However, based on experience from this work, a few more tweaks should probably be made. Firstly, use the grayvalue correction by pressing "Grayvalue Correction" and check the boxes named "Use Grayvalue Normalization" and "All Images" (Figure C.3).
  16. It will probably also be necessary to use the Multiscale fast fourier transform function. This will take into account the movement of the sample and correct for this. Rigid body movements can be corrected for by using this function. In the tab called "Multiscale", check the box marked "Use Multiscale". In addition, filters should be chosen in the boxes below, with increasing FFT size mask, as shown in Figure C.4.
  17. In case some of the images cause the analysis to fail, specific images can be skipped by manually entering the image indices in the tab "General", as shown in Figure C.1.
  18. To start an analysis, press "Save and Close", then right-click on the input file and select "Run analysis".
  19. The results can be viewed when the analysis is complete, by right-clicking the input file and selecting "Results view (image)".
  20. A map of the principal strains can be produced by right-clicking  $\epsilon_1$  and selecting "Set as Field Map", as shown in Figure C.5.



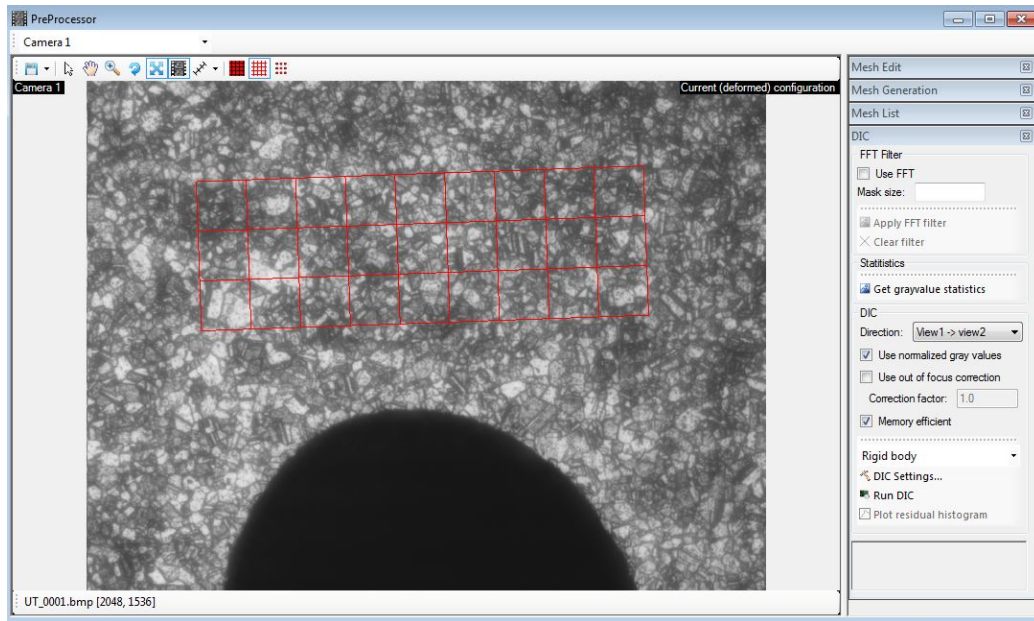


*Figure C.1: The PreProcessor window in eCorr v4.0.*

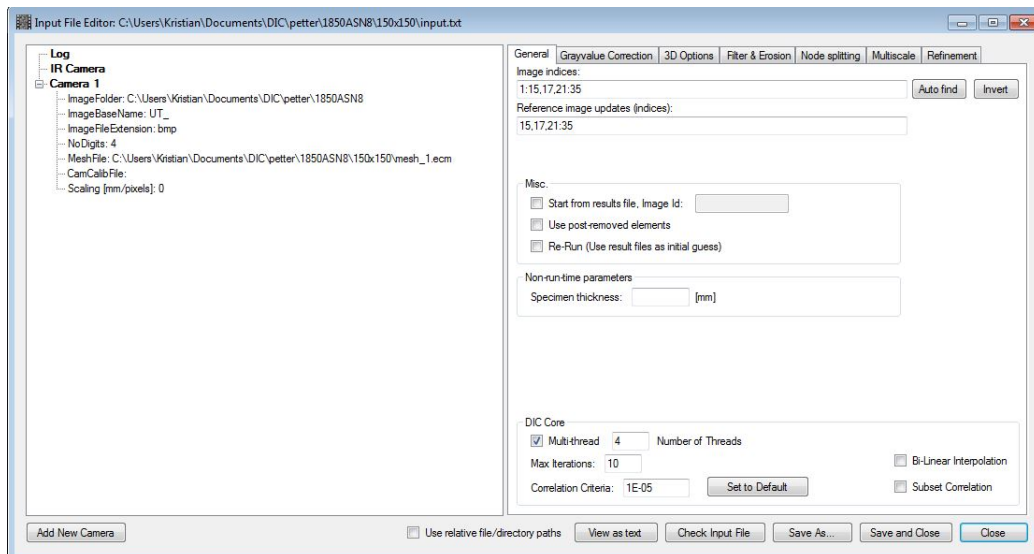


*Figure C.2: The input file editor.*

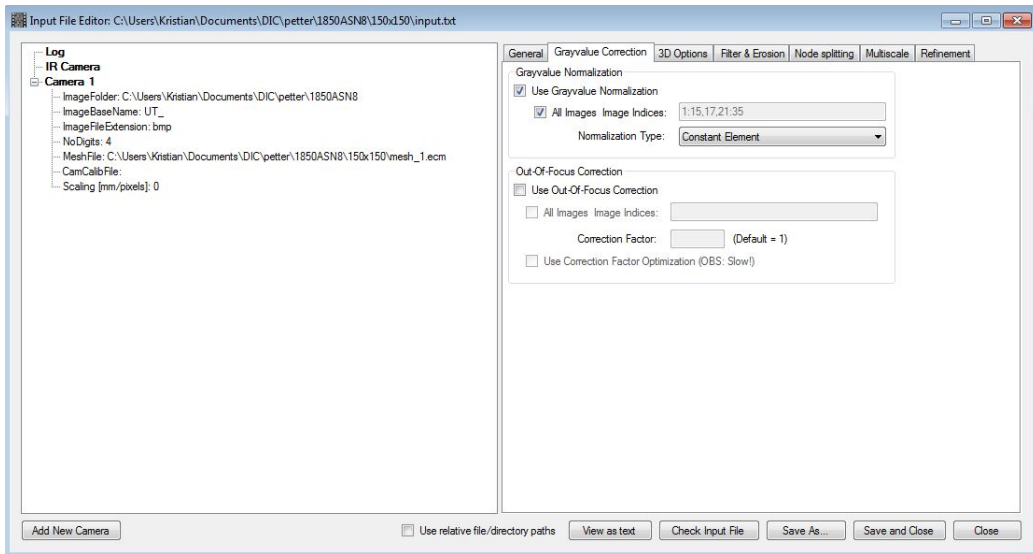


*Figure C.3: The Grayvalue correction tab.*

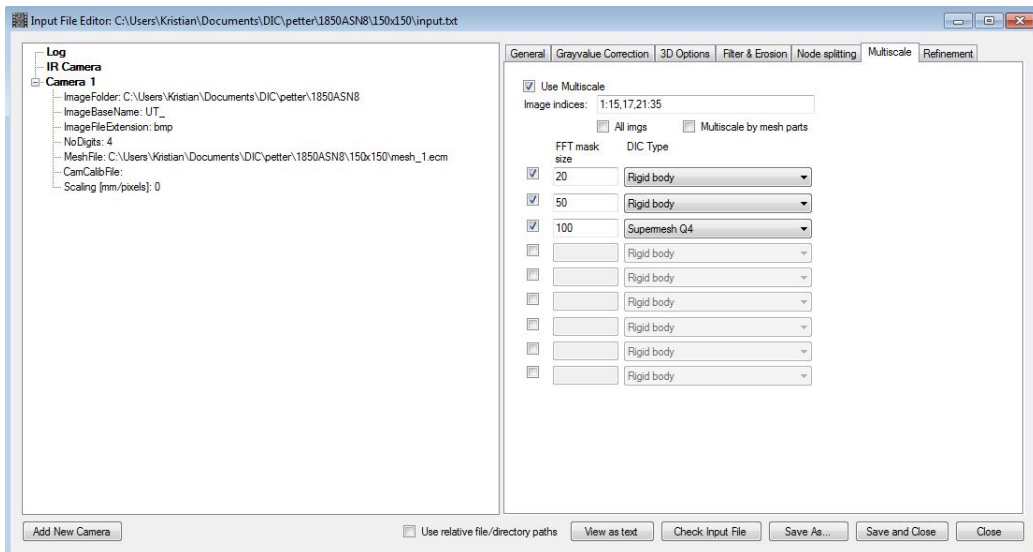


*Figure C.4: Setting used for the Multiscale tab.*

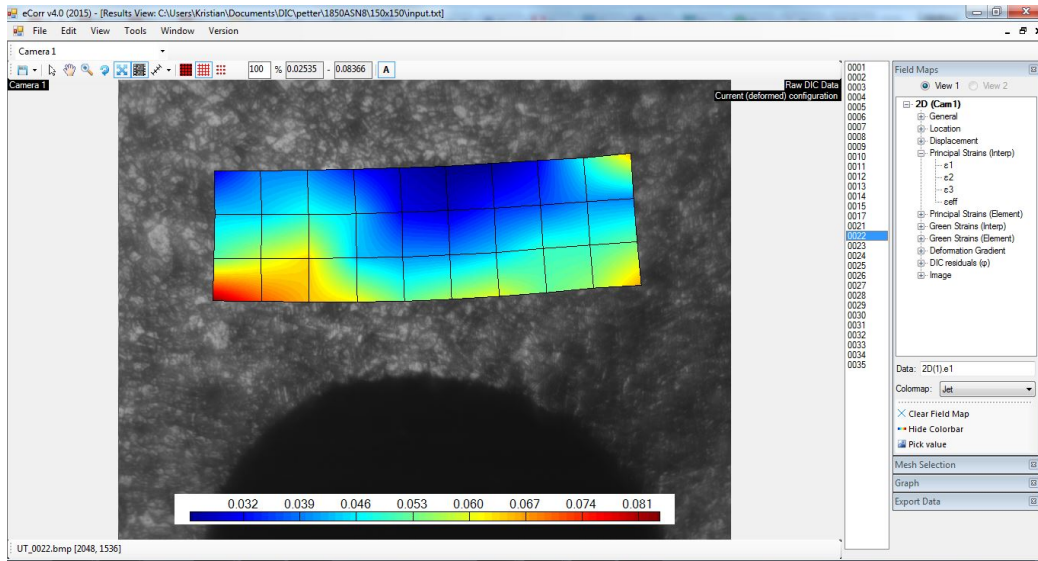


*Figure C.5: In the Results view section, a map of the principal strain can be made, among other things.*

# Appendix D

## Additional EDS results from coarse grained 1900

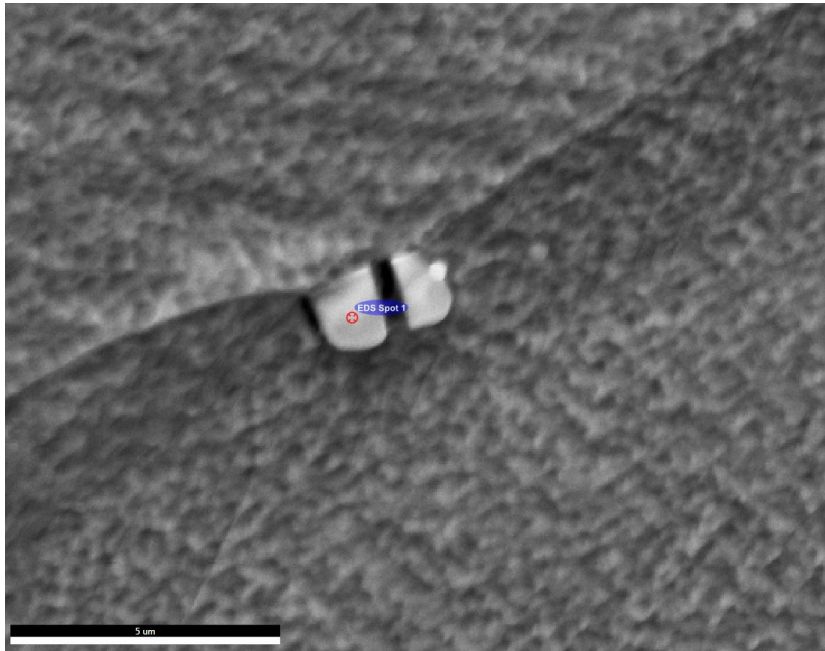


*Figure D.1:* A particle from 1900 SN-4 that was examined by way of EDS. The particle displayed high Nb and C levels.

*Table D.1:* Chemical content of the particle from 1900 SN-4. The particle exhibited Nb and C levels indicative of NbC-particles.

Element	Weight %	Atomic %	Error %
C	18.53	60.62	10.88
N	0	0.01	99.99
Al	0.25	0.36	12.59
Nb	66.96	28.32	1.72
Mo	0.77	0.32	11.73
Ti	7.99	6.56	3.84
Cr	1.17	0.88	15.07
Fe	1.35	0.95	16.78
Ni	2.97	1.99	10.71

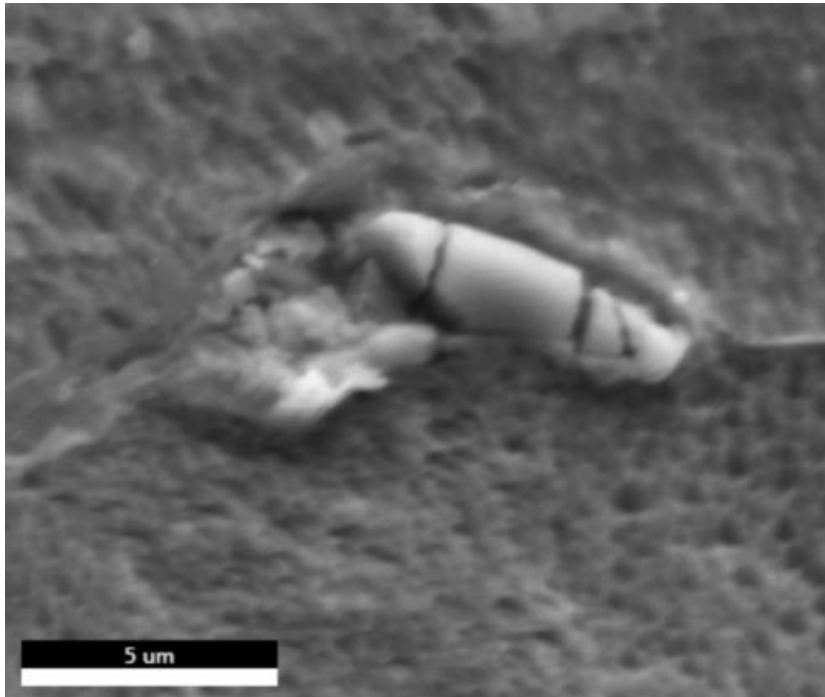


*Figure D.2:* A particle from 1900 SN-3 that was examined by way of EDS. The particle displayed high Ti and N levels.

*Table D.2:* Chemical content of the particle from 1900 SN-3. This particle exhibited chemical content indicative of TiN-particles.

Element	Weight %	Atomic %	Error %
C	3.85	9.76	8.64
N	20.25	44.02	7.86
Al	0.43	0.49	8.03
Nb	4.27	1.4	1.97
Mo	0.6	0.19	7.5
Ti	62.37	39.66	1.34
Cr	2.28	1.33	4.1
Fe	2.11	1.15	4.18
Ni	3.84	1.99	3.59

# Appendix E

## Signed Problem Text

THE NORWEGIAN UNIVERSITY  
OF SCIENCE AND TECHNOLOGY  
DEPARTMENT OF ENGINEERING DESIGN  
AND MATERIALS

**MASTER THESIS SPRING 2015  
FOR  
STUD. TECHN. KRISTIAN KNARBAKK**

**Hydrogen Induced Stress Cracking of Ni-alloys under Cathodic Protection**

Hydrogen induisert sprekking av Ni-legeringer under katodisk beskyttelse

During the last 10 years a lot of effort has been used to establish an understanding of the behavior and properties of stainless steels under cathodic polarization. Hydrogen induced stress cracking (HISC) is the main treat to the stainless steels under such conditions. Due to new demanding conditions, the oil and gas industry see an increased demand for use of Ni-alloys. Up to recently it has been an understanding that Ni-alloys are less exposed to HISC. NTNU and Aker Solutions have started a PhD project to establish a better understanding of the behavior of selected Ni-alloys under cathodic polarization.

During the last two years several student projects and master thesis have examined the effect of different parameters on the HISC susceptibility for Alloy 718 and Alloy 725 to support the PhD program. However, this is a complex topic and more R&D is needed.

Experiences from earlier work have shown that the HISC susceptibility of Alloy 718 is dependent of chemical composition and microstructure of the alloy. The effect of grain size is not yet clear, and this should be further studied in this MSc project. In addition, Alloy 625 (HIP) will also be included in the test program and compared to the performance of Alloy 718. The following activities are planned:

1. Modify/upgrade the test equipment
  - Implement strain measurement to the tensile machine.
  - Implement a new microscope to be able to detect and examine crack initiation. This crack should then be further examined in the SEM.
  - Design new chambers to avoid the problems with bubbles (Optional, will depend on the working distance of the new microscope).
  - Prepare samples with better defined notch geometry like a single EDM cut or even fatigued crack.
2. Experimental work
  - The notch effect should be taken into consideration. Simple FE-modelling can be used to investigate the effect of the crack geometry (in cooperation with Haiyang Yu).
  - Continue to examine the grain size effect. Do more parallels similar to the ones done in the project in order to make a strong conclusion about the grain size effect (Alloy 718).
  - Do initial tests with Alloy 625.

Based on the results from the project work, it shall be decided whether or not to pre-charge the samples before testing.

The work will be executed in close cooperation with the PhD candidate Gaute Stenerud. Aker Solutions will be industrial partner in the project.

**Formal requirements:**


Three weeks after start of the thesis work, an A3 sheet illustrating the work is to be handed in. A template for this presentation is available on the IPM's web site under the menu "Masteroppgave" (<http://www.ntnu.no/ipm/masteroppgave>). This sheet should be updated one week before the master's thesis is submitted.

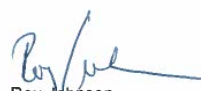
Risk assessment of experimental activities shall always be performed. Experimental work defined in the problem description shall be planned and risk assessed up-front and within 3 weeks after receiving the problem text. Any specific experimental activities which are not properly covered by the general risk assessment shall be particularly assessed before performing the experimental work. Risk assessments should be signed by the supervisor and copies shall be included in the appendix of the thesis.

The thesis should include the signed problem text, and be written as a research report with summary both in English and Norwegian, conclusion, literature references, table of contents, etc. During preparation of the text, the candidate should make efforts to create a well arranged and well written report. To ease the evaluation of the thesis, it is important to cross-reference text, tables and figures. For evaluation of the work a thorough discussion of results is appreciated.

The thesis shall be submitted electronically via DAIM, NTNU's system for Digital Archiving and Submission of Master's theses.

Supervisor: Roy Johnsen  
Co-supervisor: Afrooze Barnoush and Gaute Stenerud  
Industrial contacts: Jim Stian Olsen, AKSO

  
Torgeir Wærø  
Head of Division

  
Roy Johnsen  
Professor/Supervisor

 NTNU  
Norges teknisk-  
naturvitenskapelige universitet  
Institutt for produktutvikling  
og materialer

The scope of this work changed somewhat over the course of the semester. Following discussions with supervisors the focus changed to crack initiation, grain size effect and development of the experimental setup. Samples of Alloy 625 were never received.



# Appendix F

## Signed Risk Assessment

side 2 av 2 09.01.2015

C:\Users\Gjest\AppData\Local\Temp\Risikovurdering Risikovurdering kartlegging og risikovurdering

NTNU		Risikovurdering		Utskrift av		Nummer		Dato	
HMS IKS				HMS-ansv.		HMS-ansv.		04.02.2015	
				Godkjent av		Side		04.02.2015	
				Rektor					
Enhet:		IPM		Dato:		15.01.2015			
Linjeleder:		Torgeir Vælo							
Deltakere ved risikovurderingen (m/ funksjon):		Roy Johnsen, Afrooz Barnouhi, Kristian Knarbakk							
Kort beskrivelse av hovedaktivitet/hovedprosess:		Masteroppgave om "hydrogensprøket i nikkellageringer ved katodisk polarisering"							
Signaturer:		Ansvarlig veileder: <i>[Signature]</i>		Student: <i>Knarbakk</i>					
ID nr.	Aktivitet/prosess fra kartleggingsstadiet	Mulig uønsket hendelse	Vurdering av sannsynlighet (1-5)	Vurdering av konsekvens			Risiko-verdi	Kommentar/risikostatus	Forslag til tiltak
				Menneske (A-E)	Ytre miljø (A-E)	Om-domme (A-E)			
1	SEM/EBSD	Støtting/ødelagte av utstyr	2	B	A	D	B	B2	Følg opplæring og instruksjoner.
2	Kunnging med sag	Støde på utstyr	2	A	A	B	A	A2	Kontroller oppsett før kutting.
3	Elektropolering	Støde på utstyr, fell bruk av kjemikalier	3	A	B	C	A	A3	Følg instruksjoner. Væsk maskinen godt etter bruk og um kjemikalier i riktige beholdere.
4	Mekamisk pussing og polering	Støde på fingre og utstyr	4	A	A	B	A	A4	Følg instruksjoner. Pass godt på fingrene.
5	Strøkkoster	Ødelagte utstyr	2	A	A	C	A	A2	Følg instruksjoner.
6	Chargering	Selling med saltvann, evt andre kjemikalier	2	B	A	A	A	B2	Følg rutenevner.
7	Blanding av kjemikalier	Ekstrem varmeutvikling, utvikling av farlige gasser etc.	2	D	D	D	D	D2	Les nøye gjennom beredelse. Kjenn til kjemikaliet før bruk. Bruk ventilasjon og følg tid fra romsvarsvidg.

C:\Users\Gjest\AppData\Local\Temp\Risikovurdering Risikovurdering kartlegging og risikovurdering  
side 1 av 2 09.01.2015

NTNU		HMS	
Kartlegging av risikofylt aktivitet		HMS-prosedyre	
HMS-ent.	HMS-ent.	Godkjent av	Dato
22.01.2011	HMSRV2601	Bisk	01.12.2008
Elev		Elev	

Enhet: IPM Dato: 15.01.2015  
 Linjeleder: Torgetr Welo

Deltakere ved kartleggingen (ni funksjon):  
Roy Johnsen (hovedveileder), Afrooz Barnouch (medveileder), Kristian Knarbygg (stud.)

Kort beskrivelse av hovedaktivitet/hovedprosess:  
Masteroppgave om "hydrogensprøker i utikkallegeringer ved katodisk polarisering"

Signaturer: [Signature] Student: Kristian Knarbygg

ID nr.	Aktivitet/prosess	Ansvarlig	Eksterne dokumentasjon	Eksterne sikringsstiltak	Lov, forskrift o.l.	Kommentar
1	SEM/EBSD	Kristian Knarbygg	Risikovurdering av usyr, manual	Bruk av pålagt verneusyr	HMS-prosedyrer og arbeidsmiljøloven	
2	Kutting med sag	Kristian Knarbygg	Risikovurdering av usyr, manual	Bruk av pålagt verneusyr	HMS-prosedyrer og arbeidsmiljøloven	
3	Elektropolering	Kristian Knarbygg	Risikovurdering av usyr, manual	Bruk av pålagt verneusyr og ventilasjon	HMS-prosedyrer og arbeidsmiljøloven	
4	Mekanisk pussing og polering	Kristian Knarbygg	Risikovurdering av usyr, manual	Bruk av pålagt verneusyr	HMS-prosedyrer og arbeidsmiljøloven	
5	Strøktøler	Kristian Knarbygg	Risikovurdering av usyr, manual	Bruk av pålagt verneusyr	HMS-prosedyrer og arbeidsmiljøloven	
6	Charging	Kristian Knarbygg	Risikovurdering av usyr, manual	Bruk av pålagt verneusyr	HMS-prosedyrer og arbeidsmiljøloven	
7	Blending av kjemikalier	Kristian Knarbygg	Kartotek	Bruk av pålagt verneusyr og ventilasjon	HMS-prosedyrer og arbeidsmiljøloven	Les nøye gjennom kartotek for kjemikalier. Spørre romansverfing hvis i tvil.